Canadian Solar Road Panel Design:
A Structural and Environmental Analysis

by

Andrew Bruce Northmore

A thesis
presented to the University of Waterloo
in fulfillment of the
thesis requirement for the degree of
Master of Applied Science
in
Civil Engineering

Waterloo, Ontario, Canada, 2014

Author's Declaration

I hereby declare that I am the sole author of this thesis. This is a true copy of the thesis, including any required final revisions, as accepted by my examiners.

I understand that my thesis may be made electronically available to the public.

Abstract

Solar road panels are a technology that have the ability to revolutionize the way that roads are built and how electricity is generated. Strong incentives towards sustainable solutions in both of these fields have led to the design of innovative, multifaceted solutions, of which solar road panels are one of the most recent entrants. This research presents some initial analysis into the design of solar road panels from the perspective of Canadian pavement engineering. The hypothesis of this research was as follows:

> A specially designed modular panel can be constructed to withstand the structural and environmental loads on Canadian pavement structures while simultaneously generating electricity through embedded photovoltaic cells.

Through a process that covers the design, construction, and analysis of the structural elements of a solar road panel prototype, this research evaluated the impact that solar road panels can have for Canada's pavement infrastructure. Specific elements researched include the material selection for such a panel, the flexural response of the composite structure, how the panel will interact with traditional pavement and geotechnical materials while in use, and the change in performance of transparent layer materials as they are subjected to freeze-thaw cycling and scaling.

The research found that the initial prototype design included a two 10-mm tempered glass pane transparent layers with a 12.7-mm GPO-3 optical layer and 19.1-mm GPO-3 base layer. The concept being that the glass would provide the rigidity required to protect the fragile solar cells while the fiberglass laminate has demonstrated performance as a traffic-supporting material in adverse conditions.

Testing of this structure found that the performance was easily duplicated through finite element analysis, given that the material properties were assumed to be more rigid than the averages for tempered glass and GPO-3. Further finite element analysis demonstrated that the prototype solar road panel would not fail through traditional fatiguing methods, and in all cases on concrete, asphalt, granular, and subgrade bases the panels improved the performance characteristics of the structural base.

The environmental conditioning of acrylic, glass, and polycarbonate specimens demonstrated that glass is the ideal material choice for the transparent layer for Canadian solar road panels. It proved to have the greatest freeze-thaw and scaling resistance of the three materials, and while the friction characteristic of the flat glass samples would not be suitable for driving on, avenues of research were identified that could improve this characteristic.

In summary, the research conducted clearly proved the hypothesis; it is possible to build a structure that can house a photovoltaic system while supporting the structural and environmental loads that Canadian pavement are exposed to. The ideal panel would be constructed with a tempered glass transparent layer, GPO-3 optical and base layers, and the structure would be installed on a concrete structural base. The refinement of this design will be the scope for future research.

Acknowledgements

I first and foremost would like to acknowledge my supervisor, Dr. Susan Tighe, for all of her support in completing this research program. Without her this project would not have existed and her vision and guidance were critical in helping me get through the challenges of this expansive project. I will always be grateful for what I have learned from you and hope to pay the favor forward to many junior engineers in the future.

I would next like to thank the Natural Science and Engineering Research Council of Canada, Ontario Graduate Scholarship Program, University of Waterloo, and the Transportation Association of Canada for various levels of funding support throughout this project, without which none of my research would have been completed.

I would also like to thank all of the technical staff who helped me realize my research program. This includes Richard Morrison for his support in designing my structural testing program, Rob Sluban for helping me with all of my instrumentation needs, Douglas Hirst for designing my hydraulic load system and for other miscellaneous design needs, Phill Laycock and Andrew Urschel for providing design advice for fixture development, Rob Kraemer for consultation and construction on the testing frame design, Mark Griffett for his training and equipment provided for the three-point bending testing, and Dr. Michael Collins for providing training for and access to optical testing equipment.

Special thanks are extended to all of my colleagues who proved reliable time and time again at providing advice and for bouncing ideas off of. This includes, but is not limited to, Zaid Alyami, Dr. Mohab El-Hakim, Marcelo Gonzalez, Aleks Kivi, Boyd Panton, and Magdy Shaheen. Developing my research was a challenging process and your support helped make it possible.

Last, but certainly not least, I would like to thank my family, friends, and amazing girlfriend for helping keep me relatively sane through the last three years of my exhaustive research program. It’s been an amazingly stressful adventure and without your support I could not have accomplished it. There are far too many people to name here, but you all know who you are and I am forever in your debt for the help you have given me.

Table of Contents

List of Figures

List of Tables

Chapter 1

Introduction

Sustainability has become a leading goal of global infrastructure developments over the last several years due to increased understanding of the impacts that engineering decisions have on society and the environment. The leading definition for sustainability was created by the Brundtland Commission and states that sustainable development is “development that meets the needs of the present without compromising the ability of future generations to meet their own needs” (World Commission on Environment and Development, 1987). This is traditionally accomplished through optimizing the balance between design economic, environmental, and societal impacts while still delivering infrastructure that meets the original design requirements (Adams, 2006). While it is often possible to make traditional designs more sustainable by these metrics through evolutionary modifications, revolutionary redesign of infrastructure from first principles allows for rediscovery of its full potential.

This holds true within the realm of pavement infrastructure, where the majority of the materials currently used in roads and highways have not changed over the last few decades. Recent pushes have been made to make pavements more sustainable in a number of ways. One such way has been looking at using more recycled materials in pavements, be it glass, asphalt shingles, recycled asphalt pavements, recycled rubber tires, or other additives in asphalt mixes or recycled concrete and other additives in concrete mixes. Other focuses for increasing pavement sustainability have included reducing the processing temperatures required for asphalt and creating porous pavements which offset the need for stormwater management. While these technologies combined help make pavements incrementally more sustainable, the fact of the matter is they all look at pavement design through the same lens as designers have for the last few decades.

This becomes a problem within the transportation industry due to how large transportation’s impact on the environment is as a whole. It is well established that for our society to be more sustainable there must be substantial changes in our energy consumption and greenhouse gas emission patterns, and transportation is the cause of 19% of global energy consumption (US EIA, 2011) and 23% of global CO_2 emissions (IEA, 2011). While most of this is a direct result of transportation modes and not the infrastructure that satisfies these modes, the infrastructure is always designed with the mode energy consumption and emissions in mind. For roads there are direct correlations on the impact that roughness (Costello, Bargh, Henning, & Hendry, 2013) and grade have on vehicle fuel consumption, traffic intersections are naturally designed to minimize delays and as a result vehicle idling time, and the same applies to minimizing delays when performing road maintenance. All of these factors are the responsibility of regional transportation authorities, so solutions that minimize their energy or carbon footprint in a major way are highly sought after solutions.

One way that many jurisdictions have started making their transportation corridors more sustainable is by incorporating renewable energy projects into their territory. While using transportation corridors for utility purposes other than transportation is not a novel idea, the interest in incorporating renewable energy projects has only been building slowly over the last few decades. Most of the longer term projects exist in Europe, where they have constructed solar railway tunnels in Belgium (Enfiinty, 2011), solar highway tunnels in Italy, and solar highway tunnels and noise barriers in Germany (US DoT, 2012). Recently in the United States, many state Departments of Transportation have investigated the benefits of adding solar panels and wind turbines and using highway lands to grow crops for conversion to biofuels (US DoT, 2012). These projects demonstrate the interoperability of the right-of-way with renewable energy projects, though they for the most part ignore that roads have the capability to be a multifunctional element of our infrastructure.

1.1 Solar Road Panels

In Canada there are over 400,000-km of two-lane equivalent paved roads (Transport Canada, 2008) which accounts for 2,880-square km of paved surface area. As shown in Figure 1-1, the average daily solar energy available on flat mounted surfaces across Canada is 12-MJ/m^2 (3.3-kWh/m^2) (NRC, 2012). As a result the average day sees 9.5-TWh of solar energy incident on paved Canadian roads, which is 5.6 times higher than the current daily average electricity generation in Canada of 1.69-TWh (Statistics Canada, 2012). Even if you could only convert 5-10% of this energy into electricity due to efficiency losses in solar energy conversion systems, it is clear that the amount of solar energy available on Canadian paved infrastructure is far from insignificant and is a resource that modern pavement design should attempt to utilize.

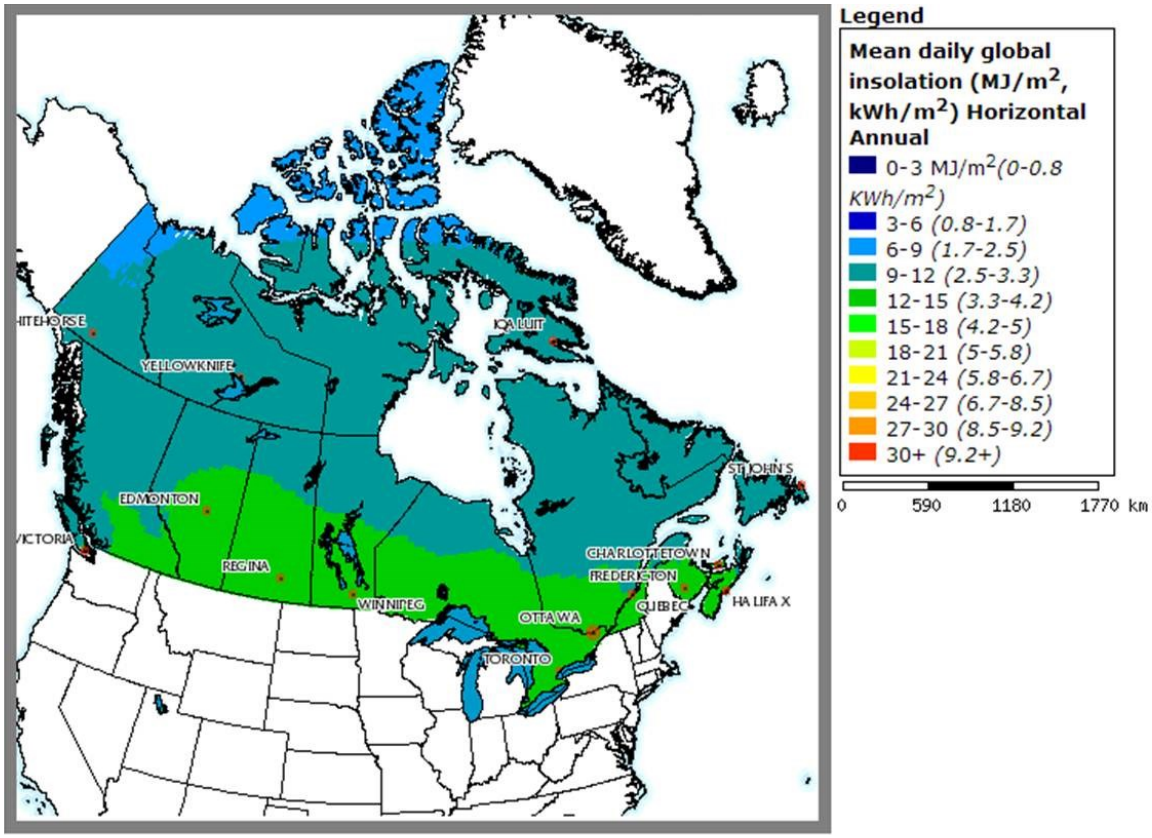

Figure 1-1: Mean daily solar insolation across Canada (NRC, 2012)

A few different methods have been researched to attempt to generate electricity from this resource. The first was done by turning traditional asphalt pavements into solar thermal collectors (Bijsterveld, 2001). While this was a logical choice due to the known heat retention of asphalt pavements, maintenance of such structures is very challenging as the piping that runs through the asphalt disrupts traditional maintenance approaches. More current research is being done on using thermoelectric generators to directly extract electricity from the thermal gradient in asphalt pavement structures (G. Wu & Yu, 2012), though this research is still in its infancy and has very low conversion efficiency. The most promising technology in this field also happens to be the most innovative and is the only one to completely disregard traditional paving practices: the development of solar road panels.

Solar road panels are a new technology being designed to serve as the top layer of pavement infrastructure. The key benefit from this approach is that it is a modular structure which incorporates photovoltaic cells which directly convert the incident solar energy into electricity. This electricity could have a number of uses, such as powering street lights, charging electric vehicles, or being sold to local distribution companies. While the greatest influence of these panels would come from replacing highway pavements, many lower speed and volume applications are currently being considered as ideal locations for installation of these panels (Northmore & Tighe, 2012a).

The panels are a three layer composite structure that consists of transparent, optical, and base layers as shown in Figure 1-2 (Northmore & Tighe, 2012a). The transparent layer handles direct interaction with vehicles and allows solar radiation to pass through to the optical layer. The optical layer transfers the load on the transparent layer to the base layer by directing it around the embedded solar cells within the structural cutouts. Lastly the base layer transfers load to the structured base beneath the panel (Northmore & Tighe, 2012b).

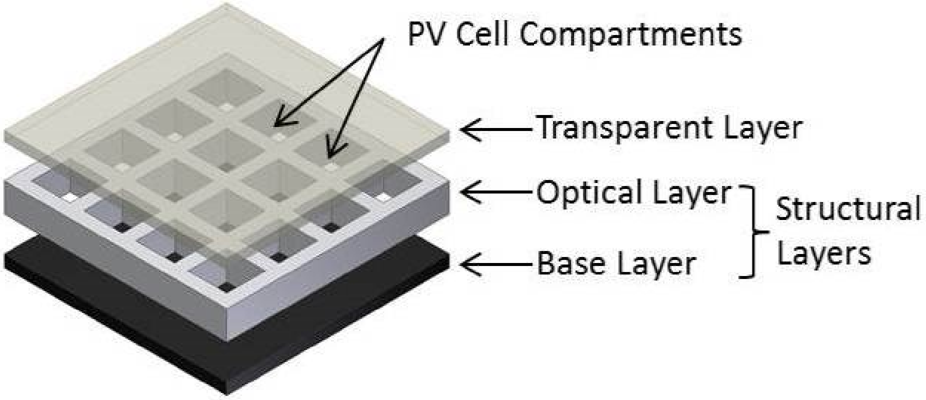

Figure 1-2: Exploded view of a conceptual solar road panel (Northmore & Tighe, 2012a)

Overall the research on solar road panels is also in its infancy. There are only two organizations working towards the development of these panels: Solar Roadways in the United States and TNO in the Netherlands. The prototypes being developed by these groups are being designed with less focus on optimizing the design of a composite pavement structure to act as a solar road module in a variety of structural scenarios and neither considers how to mitigate the issues of salting and freeze thaw effects experienced during a typical Canadian winter.

1.2 Research Scope and Hypothesis

The scope of this research was to define the design of a solar road panel that would be able to withstand the structural and environmental loads placed on it under use in a Canadian environment. Figure 1-3 shows a flow chart of the research activities completed as part of the scope of this project. The hypothesis for this research is as follows:

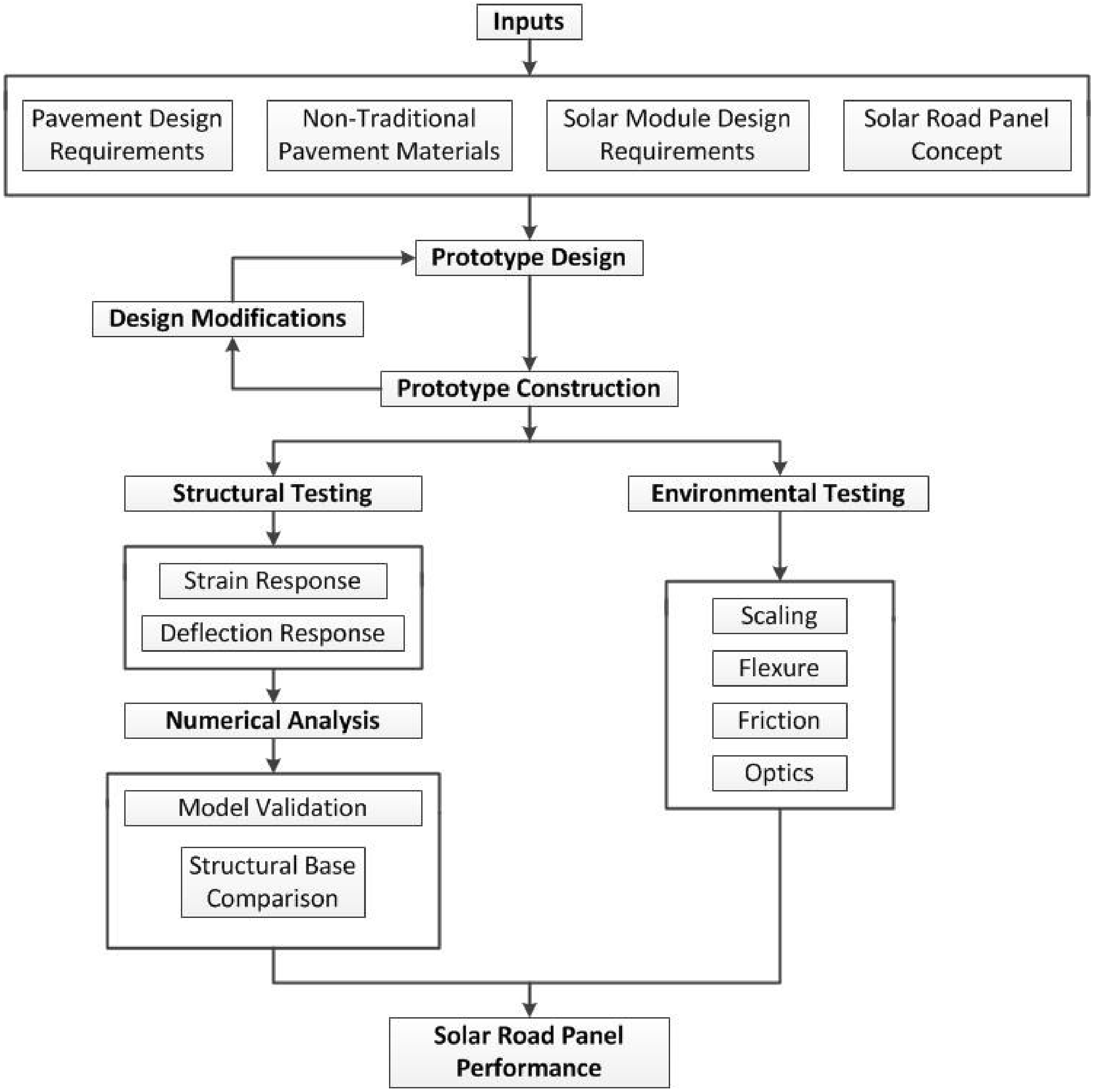

Figure 1-3: Research methodology

> A specially designed modular panel can be constructed to withstand the structural and environmental loads on Canadian pavement structures while simultaneously generating electricity through embedded photovoltaic cells.

This research involved the design, construction, and testing of solar road panel prototypes in a laboratory environment at the Centre for Pavement and Transportation Technology (CPATT) at the University of Waterloo. Additional testing work was performed through the Civil Engineering

Structures Laboratory, the Solar Thermal Research Laboratory, and the Mechanical Materials Laboratory at the University of Waterloo.

Laboratory testing of the solar road panel prototypes was done to determine the physical response of the panel to loading and to replicate the stresses of Canadian environmental conditions. This work was accomplished to properly assess the surface, structural, and optical characteristics of solar road panels and candidate transparent layer materials.

1.3 Research Objectives

The main objective of this research was to determine how a solar road panel could be constructed. The two main criteria considered were structural and environmental performance of the panels and associated materials. The specific objectives of this research included:

1. Determination of the design requirements and material selection required for the optimal solar road panel for use in Canadian conditions.
2. Design a prototype solar road panel to be used for laboratory testing and as a platform for future related research.

1.4 Research Contribution

It is expected that the research findings will provide a basis for solar road panel design for usage in a Canadian environment. This will be largely focused on the performance of the materials within the panel but also provide design inputs for the structural base material options and electrical system design.

Another contribution of this research involves guidance on the structural performance of non-traditional pavement materials as a form of subgrade or pavement reinforcement. Traditional work in this field has examined these materials as short-term reinforcement for poor subgrade soils exposed to heavy vehicle traffic while this research examines how these materials could perform over the long term on strong subgrades or on typical paved bases for city or municipal traffic loads. The work done herein is also more focused on finite element modeling of these systems while previous work was completed primarily through laboratory experiments.

The third major contribution of this work is in determining the performance of transparent materials as they are subjected to scaling and freeze-thaw cycling. This research is novel in that it assesses structural, textural, and optical properties of the materials as they are conditioned, a combination that is seldom investigated. Potential applications of this work include material selection for automotive applications, road lighting infrastructure, and building systems exposed to salt based corrosion.

1.5 Organization of Thesis

This thesis consists of six chapters. A brief description of each chapter is included below.

Chapter One: An introduction to solar road panels and the scope, hypothesis, and objectives for the entire thesis.

Chapter Two: An analysis of existing literature on design aspects for pavement and conventional solar modules and how the two topics converge towards designing solar road panels. This section also defines the gaps in existing knowledge regarding solar road panel design.

Chapter Three: The detailed design and construction processes for developing the prototype solar road panel used in testing throughout the rest of this thesis. Also included is a section on lessons learned through design and construction for the use of future researchers on this topic.

Chapter Four: Development of the testing mechanisms for solar road panel prototypes and materials. This section discusses the structural and environmental testing conditions that were developed to execute this research. Emphasis is placed on the development of the standards for both forms of testing and the design and construction of the fixture used for structural testing.

Chapter Five: Structural testing of the solar road panel prototype and numerical analysis of solar road panel designs on simulated structured bases. This section analyses the structural feasibility of solar road panels and draws conclusions about material selection, solar road panel design, and the required base for panel installation.

Chapter Six: Environmental testing of transparent materials. This section draws initial conclusions on the applicability of various polymer and glass materials as a transparent layer material for solar road panels installed in a Canadian climate with typical winter road maintenance practices. This was done through analysis of their mechanical, optical, and surface properties.

Chapter Seven: The conclusions drawn throughout the thesis are summarized in this chapter and compiled to define the overall structural feasibility of solar road panels. Recommendations for further research in the field of solar road panels are also presented.

Chapter 2

Design Elements

In order to develop an understanding of the requirements of a solar road panel and the justification for this research, a thorough review of pavement and solar module design elements is required. This will highlight the contrast between the designs of the two structures and identify the justification for thorough research on the design of a combined structure.

2.1 Pavement Design Elements

This section of the literature review will identify the materials and processes used in the design of traditional pavements, the non-conventional materials and techniques used in novel soil reinforcement and flooring applications that are relevant to this research, the structural testing techniques used to validate pavement and composite panel structures, and how numerical analysis is incorporated into pavement design practices.

2.1.1 Traditional Pavement Design

Traditional pavement design is categorized by the type of material used in the structure: flexible or rigid. Flexible pavements are those that use asphalt cement binder combined with aggregate materials. Rigid pavements are made from a combination of gravel and crushed stone particles bonded by a Portland cement and water mixture. While there are many variations of these types of pavements, the design considerations are similar (TAC, 2012).

The main factors taken into pavement design are the desired design life, traffic loading, environmental conditions, subgrade soil, drainage, performance of local similar pavements, and locational constraints (TAC, 2012). Typical pavement design lives for Ontario, marking the point where the pavement structure needs rehabilitation due to inadequate performance, are between 10 and 20 years for highways depending on the pavement materials used (MTO, 1990). The factors with the highest impact on the deterioration of a pavement structure are traffic loading and environmental conditions, as these define the stresses applied to the structure that need to be supported.

Traffic loading is measured in two ways to account for the varying vehicle types that are expected to travel on the pavement structure. The first measure for this is the annual average daily traffic with the given percentage of that traffic that is trucks. This method has demonstrated correlations to pavement performance through older design methods, however newer methodologies require the number of equivalent single axle loads (EASLs) that will travel over the given section (MTO, 1990). This method converts each individual vehicle into a number of EASLs, which each represent an 80-kN axle load with dual tires, through a load equivalency factor (LEF) that approximately follows a fourth power law based on vehicle weight. This equivalency is demonstrated in Figure 2-1 for single, tandem, and tridem axled vehicles as described by the American Association of State Highway and Transportation Officials (AASHTO).

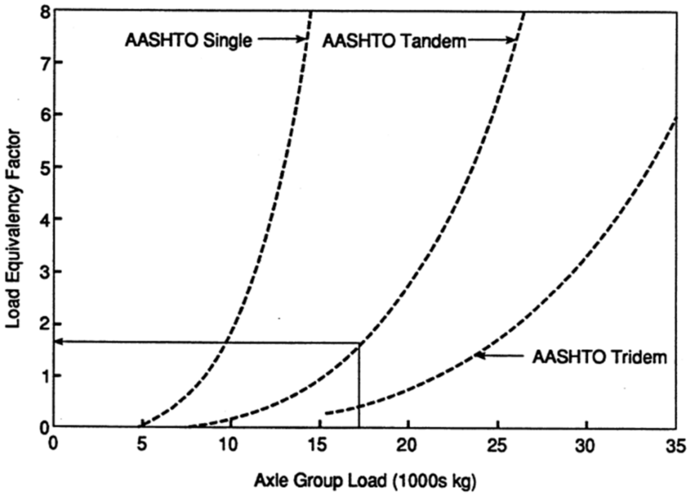

Figure 2-1: LEF relation to axle group load of AASHTO standard trucks (MTO, 1990)

The environmental conditions that have the greatest impact on pavement degradation are temperature and moisture. In Ontario the range of temperatures during the year causes a variety of issues, as low temperatures in the winter cause the ground to freeze and heave while high temperatures during the summer weaken asphalt structures allowing rutting and other failures. Moisture also causes issues because of its ability to infiltrate pavement structures and then freeze and thaw cyclically through the winter or wear away the surface pavement material. In designing roads this is taken into consideration by accounting for the expected frost penetration depth for the region. A map showing the frost penetration design standards for Southern Ontario is shown in Figure 2-2 (MTO, 1990).

Another important design factor for pavement engineers is the surface texture of their structure. In order for vehicles to safely traverse the structure, the surface must provide ample traction for tires to grip. With asphalt pavements there is no extra work needed to achieve this, though concrete structures require additional texturing once they have been laid. This is typically achieved through dragging a rough material across the surface while the material is curing or mechanically applying a texture after the concrete has hardened. The surface texture is impacted in the short term by weather conditions and the long term by vehicle traffic. Water and ice accumulation on pavement can make the surface too slippery to traverse if drainage is inadequate, while vehicle traffic will wears the surface down and requires maintenance to restore the texture (TAC, 2012).

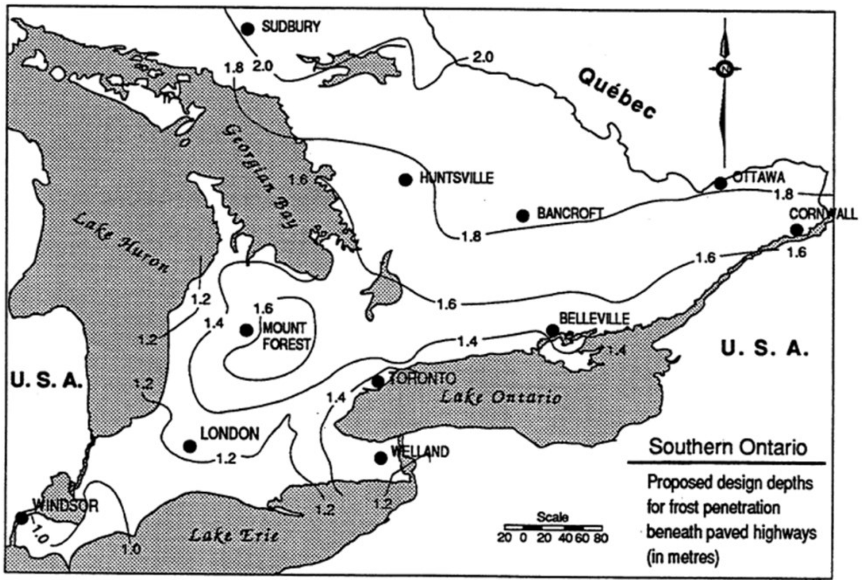

Figure 2-2: Design depths for frost penetration in Southern Ontario (MTO, 1990)

2.1.2 Non-Conventional Pavement and Flooring Materials

In addition to the conventional asphalt and concrete materials, a number of special applications require different materials to be used as reinforcement for soft subgrades or as structural surfaces. The most common of these are mats used to reinforce existing soils for military operations, specialized materials used in bridge decks, and transparent materials used in architectural flooring.

2.1.2.1 Landing and Road Mats

The US Department of Defense has funded extensive research into non-traditional road materials since the late 1930s. The focus of this work is designing mats that can be rapidly deployed as roads and landing surfaces in various environments to better support military operations. This research was deemed necessary in light of the operating conditions found during World War II, and has been an important part of American military operations globally ever since (Robinson, 2005).

Between the two, landing mats have a more stringent set of design requirements. This is largely due to the higher loadings that these mats are subjected to; the extreme weight of military transport aircraft and the high temperature jet exhaust from fighter aircraft. Another important design factor is that these panels must be light weight, so that they can be rapidly deployed. To accomplish this, the US Air Force Research Laboratory has set out guidelines that the next generation of landing mats should weigh approximately 14-kg/m^2, handle all aircraft loadings when installed on poor subgrades, provide adequate performance at a large range of operating temperatures, withstand all shear stresses from aircraft braking, and have an adequate anchoring system to firmly mount the panels (Foster & Anderson, 2003).

The most widely used early landing mats were the British Class 60 Trackway, AM-2 (Rollings, 1975), and XM19 landing mats (US DoD, 1987). All of these mats are constructed from aluminum alloys, which have the benefit of a very high strength to weight ratio, and are typically able to withstand 1,000 aircraft movements when placed on subgrades with a strength from 1.3 to 8.0 CBR (Ulery & Wolf, 1971). Given the rapid pace of military operations this represents a short service life, which then accentuates that the extruded aluminum mats are very expensive when compared to other strong materials. Modern advancements in material technologies have led multiple companies to develop their own landing mat systems, though all are still based on high strength extrudable alloys. An example of one such system is shown in Figure 2-3.

Figure 2-3: Faun Trackway aircraft landing mat system (FAUN, 2012)

Road mats are designed for a much lower strength operation than landing mats are, so many of the materials used in them are lower strength as well. Naturally aluminum and other metal alloys still provide strong performance in this application, but the lower loading from vehicles allows other less expensive materials to be considered. The typical application of these mats is the reinforcement of poor quality subgrades for the transport of military vehicles, and the mat structures are typically fiberglass reinforced polymer (FRP) hexagonal mats, plastic hexagonal mats, aluminum meshes, and plastic meshes (Webster & Tingle, 1998). An example of one such system being installed can be found in Figure 2-4.

Figure 2-4: Faun Trackway heavy ground mobility system installation (FAUN, 2012)

The testing performed on road mats is largely done on the lowest strength subgrades that the materials would be required to reinforce. Testing of road mats installed over sand and driven on by a 4,536-kg [5-ton] military truck showed that the plastic mesh mats are prone to extreme rutting, developing 84-mm [3.3-in] ruts within 20 vehicle movements. Under the same conditions the plastic hexagonal, FRP, and aluminum hexagonal mats developed ruts of 71-mm [2.8-in], 46-mm [1.8-in], and 28-mm [1.1-in] after 5,000 vehicle movements, demonstrating that these materials are much more suited to the application (Webster & Tingle, 1998).

An additional study found that the design of the road mat structure was very important to the performance of the panel. This was done again on a sand subgrade with a fully loaded six-wheel truck supplying the testing load. The majority of the designs using high-density polyethylene (HDPE) as the structural material experienced extensive rutting and structural damage over 2,000 vehicle movements, though one panel using this same HDPE material only experienced minor delamination in the same trials. This study also demonstrated that multiply FRP and aluminum structures provide adequate performance on poor subgrades, though at a higher cost and weight than the HDPE solutions (Rushing & Tingle, 2009).

2.1.2.2 Bridge Decks

One of the most common applications for non-traditional materials in pavement infrastructure is in the design of bridge decks. While highway bridges are traditionally constructed from concrete with extensive steel reinforcement and supports, many other applications see bridges designed from other materials due to either special load cases, modular construction requirements, or cost considerations.

One of the longest standing substitutes to concrete bridge deck construction is steel plate bridge decks. Being an excellent structural material, steel shows great performance in terms of loading capacity and stiffness when used in bridge deck applications. Examples of this type of bridge decking include the George Washington Bridge; the Lions Gate Bridge; and the Golden Gate Bridge, as shown in Figure 2-5 (ASCE, 2013).

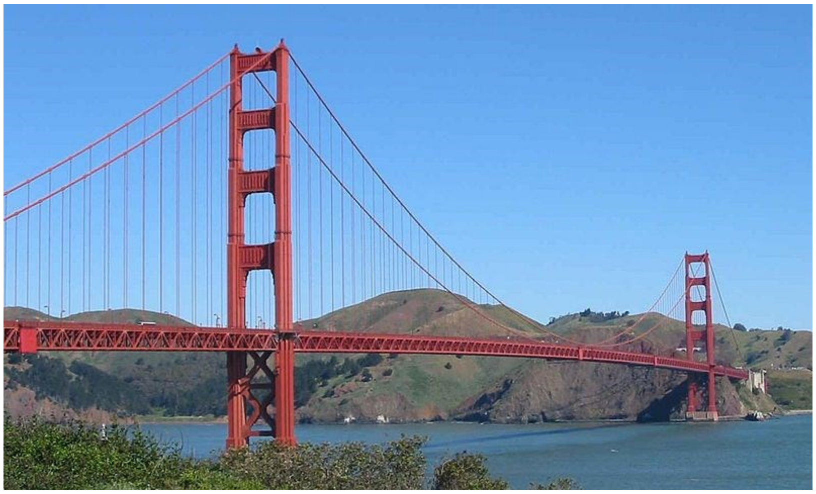

Figure 2-5: Golden Gate Bridge - Steel deck bridge

Various high strength aluminum alloys have also been used as bridge deck materials, though predominantly in pedestrian, portable, or expedient repair applications due to being a lower strength and higher cost material than more traditional alternatives. When expedient construction or bridge weight concerns are important, extruded aluminum has proven to be a suitable alternative from a strength and durability perspective. An example of an aluminum deck vehicle bridge can be found in Figure 2-6 (Walbridge & de la Chevrotiere, 2012).

Recent research demonstrates that extruded and pulltruded FRP panels are well positioned to withstand vehicle loading as an open supported bridge deck. Work completed at the University of Kentucky demonstrated that when loading FRP composite bridge deck panels as per AASHTO MS 22.5 (HS25) specified wheel loading, the typical safety factor against failure was between 3 and 8 for a variety of commercially available products. The main failure modes from this testing were debonding and flexure shear of the specimens (Alagusundaramoorthy, Harik, & Choo, 2006).

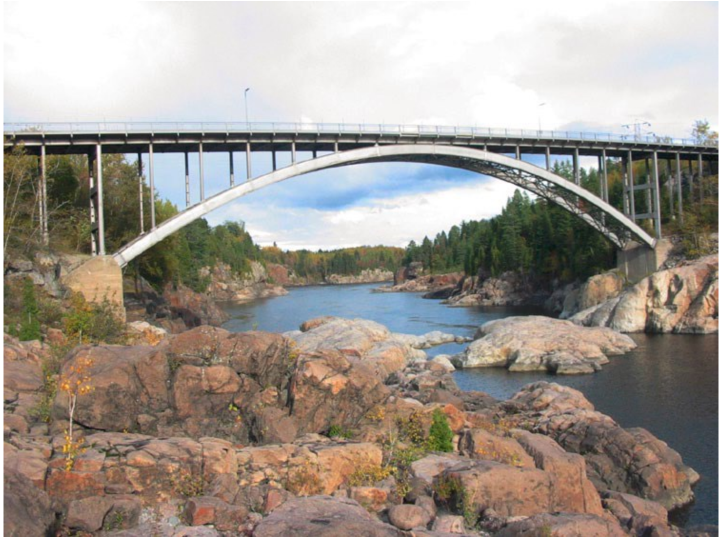

Figure 2-6: Aluminum deck bridge (Walbridge & de la Chevrotiere, 2012)

2.1.2.3 Architectural Flooring

Since this research also focuses on the need for transparent materials in transportation infrastructure, an important area of study is architectural glass flooring.

Typically, glass flooring is used in indoor environments as a prominent design feature. Many cases have seen installations in walkways, bridges, staircases, and cantilevered floor sections. The most notable of these are often in observation decks, such as the one in the CN Tower in Toronto (Torontoist, 2013), or on scenic walkways, like the one that loops over a section of the Grand Canyon in Arizona (Grand Canyon National Park, 2013). Both of these are shown in Figure 2-7.

One of the main concerns in the design of glass floors is ensuring for a large safety factor in the design. A fear of heights is common, which can make walking over a glass surface a very nerve wracking experience. To design these sections so that they are safe enough for people to walk on, the standard practice is to make the glass walking surface a three-pane glass structure (Alsop & Saunders, 1999). The three panes are laminated together using a typical resin and the glass is thick enough so that if any one of the three panes were to break the other two would be able to support the design load. This structure is demonstrated in Figure 2-8.

Figure 2-7: Glass Floors at the CN Tower (left) and Grand Canyon (right)

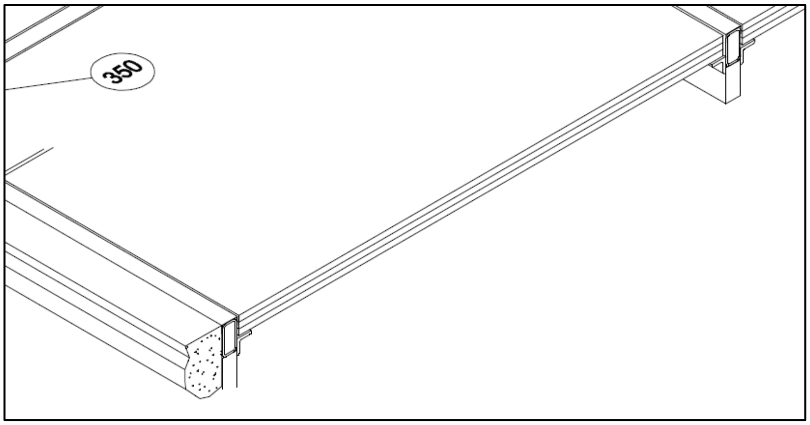

Figure 2-8: Typical glass floor panel structure (ISG, 2013)

The main reason why the majority of these installations are indoors is because the rubber-glass friction coefficient drops substantially when the surface is wet. Even at outdoor installations, people are typically not allowed to walk over the surface during inclement weather due to this reduced friction. This can be accommodated for by adding a texture to the surface, however this also reduces the transparency of the floor and reduces some of the architectural merit of the installation.

2.1.3 Structural Testing of Pavement

A wide variety of approaches are used to determine the structural capacity of pavements. Of most importance to this research is how controlled tests are performed on structural pavement sections in a laboratory or research environment.

The objective of structural testing is to determine how a structure will perform under various loading conditions that best emulate the real loading case for the structure. In terms of pavements, the most ideal test scenario allows vehicles to drive over a test section that has been instrumented to measure the strain caused within the structure. This is typically accomplished through two approaches, instrumenting new pavement sections of existing road infrastructure and constructing dedicated pavement test tracks. Both types of facilities allow researchers to better understand how specific pavement materials perform in the environment of the site; the key advantage to instrumented roads being that the site is often a better replica of that region's conditions than a test track while a test track has the advantage of a more controlled load scenario than open roads have. Due to the cost of the infrastructure required for both, these are often only implemented when determining how a new-to-the-region pavement structure will perform. An example of and instrumented road section can be found in Figure 2-9.

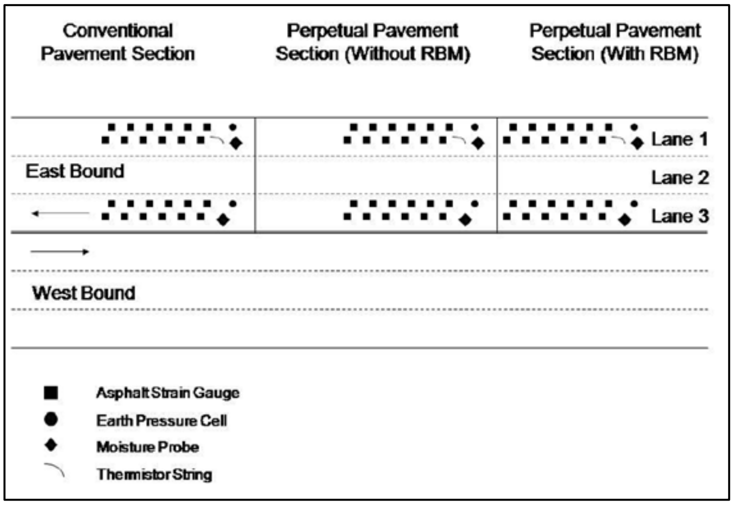

Figure 2-9: Highway 401 test section instrumentation schematic (El-Hakim, 2009)

Full pavement structure testing has also been completed in lab environments using confined pavement structures at a much smaller scale than test tracks, as shown in Figure 2-10. The concept being that when a load is applied to a pavement structure, only a portion of the total base and subgrade materials are deformed. If a confined specimen is able to contain enough material so that the deformation only occurs within a section of the contained material then real world results can be emulated in a lab. This is most commonly done in the analysis of geosynthetic reinforcing layers in flexible pavements. Typical configurations involve the design of a large steel or concrete box that contains between 0.25 and 4.5 cubic metres of pavement structural materials depending on the designed testing regime (Tingle & Jersey, 2005). Loads are typically applied through hydraulic actuators at low frequency in order to simulate vehicle traffic (Tingle & Jersey, 2005). Larger scale versions of this testing have been done in concrete pits, which would also allow for vehicles to drive over the test installation (Pokharel et al., 2011). The main disadvantages of this testing approach are the cost of developing such a setup and the limited size of the test specimens.

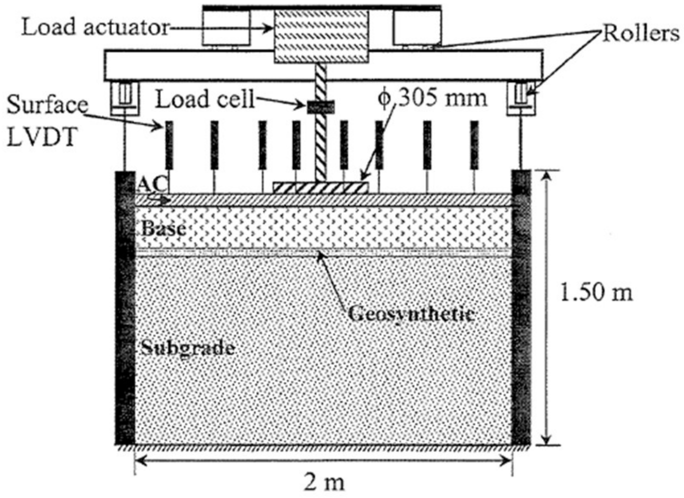

Figure 2-10: Schematic diagram of confined pavement test apparatus (Perkins, 1999)

In lieu of being able to do testing of full pavement structures, the normal method for structurally testing pavement materials is to test samples of individual materials to measure comparative properties. These tests often allow for samples to be tested under a wide variety of simulated conditions in a controlled laboratory environment. Quite often the performance characteristics determined from these tests can be used as an input for mechanistic pavement design systems; while the lab results do not directly imply performance in the field, correlations have been developed that make these results valuable. These tests can include dynamic modulus, fatigue beam, and moisture susceptibility tests for asphalt samples; compressive strength, flexural strength, and durability testing for concrete samples; and soundness, absorption, abrasion, and gradation testing for aggregate samples.

2.1.4 Numerical Analysis in Pavement Design

While the majority of pavement design is accomplished through empirical and mechanistic relations, specialized applications occasionally make use of finite element analysis (FEA) to determine the strain development that is expected within the pavement and subgrade materials for a given site. There are a number of reasons for why FEA is not widely used including the variability of pavement and soil material properties, the expense of viscoelastic material modeling, the variability introduced through constructing the site, and the ability to adequately model all pavement design factors within FEA software. As a result of this, FEA tends to be used in niche applications of pavement design. Often this can be helpful if dealing with difficult or unknown conditions or when trying to develop a better mechanistic understanding of the failure mechanisms of a pavement structure.

Some of these cases though do provide validated, simplified models for the use in approximating pavement structural performance. The first major assumption is that the materials behave only in the elastic regime, which is a valid assumption for determining a static response from pavement loading but does not account for dynamic effects. These models also often assume homogenous material properties within a given layer, which assumes a lot of ideal construction practices and material specifications. A sampling of these models has been summarized below in Table 2-1.

Additionally, work has been completed previously at CPATT on the FE modeling of steel reinforcing plates for weak subgrades. This work, using the ABAQUS software package, assessed various thicknesses of steel plate reinforcement for a sliding scale of effective subgrade modulus and soil bearing capacity. The output of this work demonstrated the type of steel reinforcement required for various base conditions and, most importantly for this research, demonstrated the applicability of the ABAQUS software package to pavement structure FE analysis (Mak, 2012).

2.2 Solar Module Design Elements

This section of the literature review will identify the basics of photovoltaic (PV) energy conversion and the requirements that this places on solar module design. The state-of-the-art in solar module design will also be assessed as well as the infrastructure requirements for PV solar arrays.

2.2.1 Photovoltaic Energy Conversion

The basic element of a PV solar module is the solar cell used to capture the incident photons and generate an electric current. There are a variety of technologies that accomplish this task, from thin film devices through crystalline solar cells, however since single crystalline silicon PV cells currently offer the best conversion efficiency for mass marketed cells (Luque & Hegedus, 2003) these will be the focus of the design of the solar road panel's electrical system.

Table 2-1: Simplified FE models of pavement structures

Author	Title and Source	Structural Design	Material Properties
Caliendo and Parisi	Stress-Prediction Model for Airport Pavements with Jointed Concrete Slabs (Caliendo & Parisi, 2010)	300-mm PCC	E = 38,200-MPa v = 0.15
		2,500-mm subgrade	E = 50-MPa to 200-MPa v = 0.35
Cho et. al.	Considerations on Finite-Element Method Application in Pavement Structural Analysis (Cho, McCullough, & Weissmann, 1996)	105-mm HMA	E = 2,413-MPa v = 0.35
		205-mm PCC	E = 27,579-MPa v = 0.35
		Infinite base	E = 103-MPa v = 0.35
Greene et. al.	Impact of Wide-Base Single Tires on Pavement Damage (Greene, Toros, Kim, Byron, & Choubane, 2010)	130-mm HMA	E = 4,800-MPa v = 0.35
		270-mm limerock	E = 550-MPa v = 0.40
		915-mm subgrade	E = 131-MPa v = 0.45
Xia	A Finite Element Model for Tire/Pavement Interaction: Application to Predicting Pavement Damage (Xia, 2010)	125-mm HMA	E = 3,000-MPa v = 0.40
		300-mm limerock	E = 167-MPa v = 0.30
		2,575-mm subgrade	E = 34-MPa v = 0.45

Single crystalline silicon solar cells are thin wafers of a single crystalline silicon ingot that have been cut to a prescribed size and doped on the top and bottom of the cell to promote electron transmission across the wafer. The top of the cell is heavily doped with a negative charge while the bottom of the cell is lightly doped with a positive charge. When photons enter the cell they travel until their energy displaces an electron, which then diffuses to the negatively charged top of the cell while the resulting hole drifts to the base. This release generates the electrical potential across the cell while repeated incident photons generate the electron flow between the layers. When the cells are linked together in a circuit, the electron flow passes from cell to cell and by combining enough cells this generates usable power (Luque & Hegedus, 2003; Neamen, 2003).

Typical solar cells used in utility grade solar modules have a high individual current capacity but small voltage potential. To accommodate this, solar cells within a module are linked together in series to allow the voltage to build while keeping the current constant. Depending on the size of the module there can be multiple strings of series solar cells linked in parallel to achieve the desired power output characteristics. In typical module fabrication there are 72 cells combined in two parallel strings of 36 (Luque & Hegedus, 2003).

The energy conversion potential within the solar cell is highly dependent on the materials used to make the cell. Each material type has a specific bandgap potential that can be achieved, and this is the potential that must be exceeded by an incident photon to release an electron (Neamen, 2003). Without achieving this minimum requirement no energy generation can occur and all of the photon's energy is lost as heat. Similarly, any excess energy from the photon that is not used to release an electron will be lost as heat within the solar cell. For a silicon solar cell, this bandgap energy requirement is 1.1 eV; a level of energy that exists in the upper infrared region of radiation allowing the solar cells to generate current from that point, through the optical spectrum, and onwards though with additional thermal losses (Luque & Hegedus, 2003).

2.2.2 Solar Module Design Requirements

There are a number of design requirements for solar modules due to the variety of stresses that can be placed on them during operation. The main stresses on traditional solar modules are thermal cycling, mechanical loading from environmental factors and mounting systems, ultraviolet (UV) radiation, and humidity and other atmospheric factors (Perret-Aebi, Li, Chapuis, & Heinstein, 2011).

Thermal cycling is a large issue in the design of solar modules for a number of reasons. First it is important to ensure that the module will withstand the thermal expanding and contracting that the materials will endure over the course of a year (Askeland & Phule, 2006). This is especially important as the crystalline solar cells used within the modules are very brittle and cannot endure a large lateral tensile stress (Luque & Hegedus, 2003). Another issue with thermal performance is that photovoltaic solar cells lose efficiency as their temperature increases on the order of 0.5% per degree centigrade (Skoplaki & Palyvos, 2009). This is because temperature impacts how the semiconducting cell works; it increases the developed short circuit current due to a decrease in the bandgap but also lowers the open circuit voltage due to variation in the intrinsic carrier concentration (Neamen, 2003). It is therefore important to make careful material selections when designing a solar module to account for thermal expansion and the quick removal of the excess thermalization losses from the PV conversion.

Mechanical loading plays an important role in the design of solar modules. The majority of typical solar modules are installed on a stationary or solar-tracking structural harness to allow for optimum exposure of the panels to solar beam radiation. The nature of these harnesses leaves the solar modules exposed on the top and bottom sides to wind and snow loading, depending on the climate they are installed in. Normal condition loading, including from environmental factors, is not an issue for most solar modules however impact or otherwise-transient loading can create issues that cause premature failure in the solar modules (Chung, Chang, & Liu, 2008). These need to be accounted for in the design by ensuring that the panel is sufficiently rigid to accept loads from hail, bird collisions, and like loadings appropriately.

UV radiation poses a challenge to the material selection for solar modules. While most materials are sufficiently protected for short term exterior use, solar modules are designed for an exterior use lifetime in excess of twenty years. Combine this with that the solar module must be oriented towards incoming solar radiation to be effective and this results in a lot of exposure to UV radiation sources. The materials used in solar modules must be appropriately selected so that they do not degrade during these operational conditions (Holley Jr, Agro, Galica, & Yorgensen, 1996).

Humidity and atmospheric conditions pose another large design challenge for solar module designers. Due to the electronics encased within the module there must be ample weatherproofing to make sure that moisture does not get into it and degrade the system. The same sort of degradation can come from particulate matter in the air etching the glass surface, or wearing away at the housing. Depending on the mounting strategy used, moisture infiltration can also come from direct contact below the panel. This is especially the case for ground or roof mounted units. Therefore proper materials should be chosen so that there will not be excessive moisture seeping through the panel, weatherproofing completed for the same effect, and that there will be effective resistance against other atmospheric particulate matter (Jorgensen et al., 2006).

2.2.3 Solar Module Design

Crystalline silicon solar modules are typically made by compiling five layers of material together and melting the middle plastic layers to laminate the composite panel together. The layers that make up this composite structure, as shown in Figure 2-11, are glass, two layers of ethylene vinyl acetate (EVA) encapsulant layers, PV cells and their interconnections, and a Tedlar backsheet. This arrangement causes each component of the panel to play a very important role in the overall performance of the solar module (El Amrani, Mahrane, Moussa, & Boukennous, 2007).

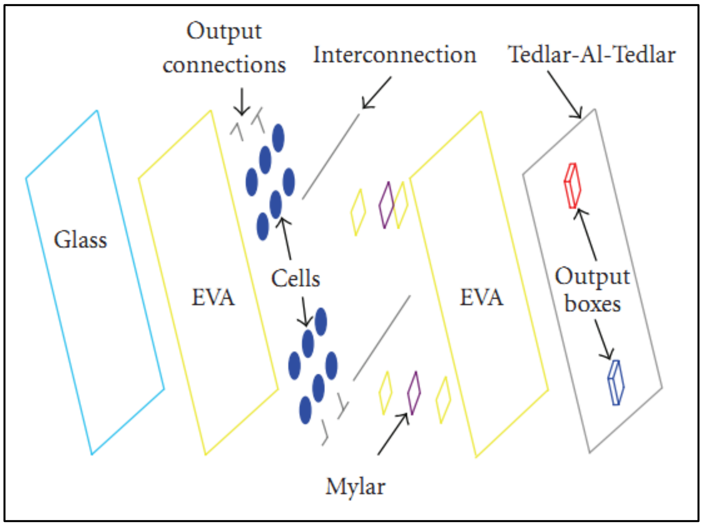

Figure 2-11: Crystalline silicon module structure (El Amrani et al., 2007)

2.2.3.1 Glass Layer

Starting with the top layer, the glass is extremely important as it must allow for free passage of solar radiation as well as providing the majority of structural support to the panel (Luque & Hegedus, 2003). Typically PV modules are made with soda-lime-silica glass with low iron content as it has excellent transmittance, coatability, weather resisting, and UV resisting properties (Deubener, Helsch, Moiseev, & Bornhöft, 2009).

One common feature of high-performance solar glass is that a texture is applied to the surface in order to improve overall performance. This texture is specially designed to trap light within the glass and minimize incident light reflection from the glass surface. These properties are both important as they help improve the overall efficiency of the solar module; any light that is not being used in the conversion process is not useful to the solar module. The texture is specifically designed with the geometry of the panel in mind as once light has entered the glass the main points of reflection are from the interface with the EVA resin and beyond that the interface between the EVA resin and the solar cells. Through knowing these it is possible to texture the glass in such a way that internal reflection of light is maximized, with a particular interest on the wavelengths of light that are closest to the bandgap of the solar cells being used (Deubener et al., 2009).

The glass texturing can be done with a number of performance objectives in mind. While a lot of research focuses primarily on the light entrapment, surface texturing can also increase the overall efficiency of a panel throughout the day and concentrate radiation to the useful portions of the solar cell. Through applying structured textures, it is possible to improve the performance of solar glass to light that approaches the panel at a large incident angle. In one case it was found that a 35% to 55% efficiency improvement was found through applying a triangular or sinusoidal surface texture to the glass when light was at an incident angle of 80° to the normal of the surface. This greatly impacts one of the challenges in solar module design, which is that the best performance is achieved with an incident angle near zero and that performance tapers on either side of this mark. While this would be of little use for solar modules that track the sun's apparent movement, the majority of solar module installations are stationary and this technology would have a great positive impact on their performance (Sánchez-Illescas et al., 2008).

While the majority of surface area on a solar module is exposed to the PV solar cell, there are a few areas that are not; gaps between the cells and the bus-bars and fingers on the solar cell. Any light that is incident on these areas is not used to excite electrons, so focusing light away from these areas and onto the main semiconducting cell has efficiency benefits. It has been demonstrated that by specifically texturing the glass above these areas that the shadow losses in a solar module can be reduced by 50%, though due to the constraints of ray tracing this is a benefit that can only be achieved through modules that have full or partial solar tracking (Bergamin & Sammaraee, 2010).

While the texture of the glass has an impact on the reflectiveness of the module, another important factor is that an anti-reflective coating is often applied to the surface of the glass exposed to the atmosphere. These coatings are typically layers of SiO_2 or Si_3N_4 which are thinly deposited onto the glass surface and produce a refractive index gradient at the coating-glass transition that maximizes transmission. Through most manufacturers this form of textured, coated glass is referred to as solar glass, as these specific properties are mostly coveted for only solar panel applications (Deubener et al., 2009).

As noted earlier, the glass is an important element from a structural perspective. With the EVA and Tedlar being comparably flexible materials to glass and a minimal aluminum frame with respect to the size of the panel, the glass is required to impart its rigidity to the rest of the panel. With the environmental loads that solar modules are expected to endure this is not much of an issue, as glass is a very strong and rigid material to low pressure loading, impact loads can be very detrimental to the performance of solar modules. Most consumer solar modules are considered with relatively thin glass, though aftermarket or hobbyist panels are made with thicker layers to provide greater strength though at a higher cost (Luque & Hegedus, 2003).

2.2.3.2 Encapsulating Layers

The majority of solar modules use an EVA compound as the laminating material. This layer performs a number of tasks for the solar module including protecting the electronics in the module from moisture, blocking UV radiation from the cells and backsheet, buffering the solar cells from loads placed on the glass or backsheet, and adhering the structure together (El Amrani et al., 2007). In mass produced modules, this layer is installed as two plastic layers, one on either side of the solar cells, so that when the module is put through lamination the EVA melts and forms around the cells and adheres the panel together (Luque & Hegedus, 2003). In hobbyist projects this can also be completed using a poured resin, as laminating a solar module without the proper equipment can be challenging.

The laminating material must also meet a number of specifications, including minimum standards of electrical, optical, mechanical, and chemical performance (Lange, Luo, Polo, & Zahnd, 2011). Equally important to this are the reliability and cost performance of the laminate through the entire assembly process of the solar module (Agro & Tucker, 2004). The specific material choice is made by the manufacturer and can vary depending on the specific properties that they are looking for; this can include benchmarks on curing time, moisture transport properties, and overall assembly procedure. Other materials often used as laminates are silicone, polyvinyl butyral, thermoplastic polyurethane, and ionomer (Agro & Tucker, 2004; Rose, Jester, & Bunea, 2008).

2.2.3.3 Solar Cell Interconnections

The cell interconnections are the next major component of solar modules. These components provide the link between each of the cells in order to create the strings of solar cells that generate electricity as required through the panel. As a result, it is very important that these elements be protected and selected so that failure risk is minimized. The interconnection is essentially a conductor that is soldered onto the top busbar of one solar cell and the bottom bus bar of the adjacent cell to complete a circuit between them. Most materials used for the interconnection strips and the solder are lead based, though switching to a lead-free solder is a major research focus as this would make solar module recycling an easier and more environmentally friendly process. The major design challenge with interconnections is ensuring that there are not significant power losses across the strings of solar cells within the module, as this has been shown to have a large impact when studied in practical applications (Hsieh, Lin, & Yu, 2011).

2.2.3.4 Backsheet Layer

The last component in a solar module is the Tedlar backsheet layer. This layer is responsible for further protecting the solar cells, particularly from any conditions applied to the back side of the panel, as well as ensuring the stability of the whole module. Tedlar is one of the leading materials used as a backsheet, though other options such as ethylene propylene diene monomers have been considered for use as new combinations of materials can help streamline the assembly process by eliminating need for the second EVA layer (Kempe & Thapa, 2008). Typical properties desired in a backsheet are high UV resistance and minimal moisture transport as this layer is directly exposed to the environment and must maintain protection for the EVA and electronics layers (El Amrani et al., 2007).

2.3 Solar Road Panel Systems

With a strong background in the areas of non-traditional pavement design and solar module design established, the next step is to understand the current state-of-the-practice on solar road panel design and identify the existing knowledge gaps that need filling in order to meet the objectives of this thesis.

2.3.1 State-of-the-Practice

As identified in Section 1.1 there are two organizations working on the development of solar road panels: Solar Roadways and TNO.

2.3.1.1 Solar Roadways

Solar Roadways is a company located in Idaho, U.S. and is developing a solar road panel that could potentially be used in highway applications. Work on developing their prototype panel began in 2009 and was sponsored by the U.S. Federal Highway Administration (FHWA). After they had developed their prototype they received a further grant from the FHWA to develop more prototypes and install them in their company's parking lot. This installation of three panels has been scheduled for the Spring of 2013 (Solar Roadways, 2013).

The panel Solar Roadways has developed is a 3.66-m [12-ft] square panel and consists of a transparent surface layer made from textured glass, an electronics layer that houses circuit boards supplying the electrical links between the solar cells and other systems, and packaging which weatherproofs the panel. In addition to simply having solar cells strung together in this system, the

Solar Roadways prototype includes LED lighting built into the cell compartments to provide messaging and lane markings from the road surface. It also includes resistance heaters to deal with any potential snow or ice issues that may develop on the surface during winter operation. An image of the first prototype from Solar Roadways can be found in Figure 2-12 (Solar Roadways, 2013).

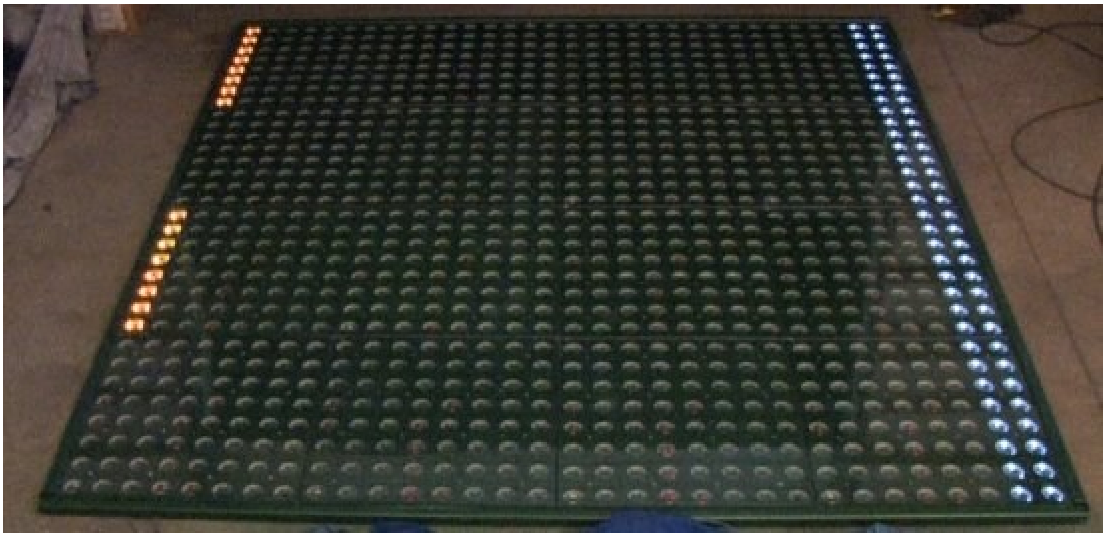

Figure 2-12: Solar Roadways prototype solar road panel (Solar Roadways, 2013)

2.3.1.2 TNO

TNO, the Netherlands Organization for Applied Scientific Research, is based in Delft and is a knowledge organization used by local companies and government agencies to develop innovative technologies to solve technical challenges in the Netherlands and abroad. Solar road panel development is only a small part of this organization's energy efficiency systems research. They've partnered with Ooms Avenhon Groep, a civil infrastructure engineering group, and Imtech, an electrical and mechanical engineering consulting group, to develop solar road panels within the context of the Dutch environment (TNO, 2013).

The first design of TNO's SolaRoad concept is being developed for use in cycling paths; infrastructure that the Netherlands has an abundance of. The panels they are building are 1.5-m by 2.5-m and consist of a glass surface layer, crystalline silicon solar cells, and a concrete block housing. The trail installation in North-Holland was expected to be installed in the summer of 2012, but to date this installation has not been completed. An image of a SolaRoad prototype is found in Figure 2-13 (TNO, 2013).

Figure 2-13: TNO SolaRoad prototype panel (Ooms, 2013)

2.3.2 Knowledge Gaps

While there are a large number of knowledge gaps in the realm of solar road panel design, despite the prototypes built by Solar Roadways and TNO, the two main ones focused on in this analysis are the overall structural analysis of a solar road panel system and the effects of winter environmental conditions and maintenance practices on such composite panels.

One of the main reasons why traditional pavement design is so variable is that no two regions provide the exact same set of conditions for building roads. When you start to assess traffic, weather, existing soil, and available resource conditions for a region you soon find that you cannot adopt a universal design practice everywhere, and this is an important lesson for solar road panel designers.

In essence a solar road panel would be a modular piece of hardware, like in Solar Roadway's and TNO's designs, but a lot of consideration has to be made on what you would be installing these panels on top of and what materials you should make the panels out of to best optimize the performance for a given soil condition. In any case, a solar road panel would need to be placed on a structured base and there is room for optimization between various material configurations for solar road panels and the types of bases you could provide (compacted soil, granular subgrade, concrete or asphalt bed, etc.). No literature thoroughly addresses this issue.

In addition, very little consideration has been made for how these panels will operate during winter conditions. This is reasonable design for TNO, seeing as the Netherlands only sees 25 snowy days on average per year (KNMI, 2013) compared to 64 in Waterloo, Ontario (Environment Canada, 2013) and much higher through other portions of Canada, but is a lacking element in the design from Solar Roadways.

As identified earlier, the design from Solar Roadways does include a resistance heater in the panel to melt any snow or ice that may accumulate however this is not a total solution to winter climate and maintenance issues. It solves the issue of damaging the panels through snow plowing operations, but salting is still a major part of winter maintenance operations. Even if it was found that the surface of the solar road panels does not need to be salted, large volumes of salt would be brought onto the solar road panel surface by cars that have been exposed to salt on other roads. Salting operations are a large attributor to the damage of civil infrastructure, so it is expected that this needs to be studied for solar road panel performance as well.

Chapter 3

Solar Road Panel Design and Construction

With a thorough understanding of the design of pavement structures and traditional solar panels having been established, this section details the design and construction processes used for developing the solar road panel prototypes used in later testing and analysis sections of this thesis.

3.1 Design

The design process for the solar road panel prototype was completed across three main phases; design requirement development, material analysis, and component system design. The material analysis focused on determining the materials which are best suited for use in a solar road panel while the system design takes the materials and the design concept and produces a functioning, manufacturable prototype.

3.1.1 Design Requirements

In developing the design requirements for a solar road panel there were two categories that the overall system was broken down into with distinct requirements: structural and electrical.

3.1.1.1 Structural Requirements

The foremost structural design requirement is that solar road panels must be able to withstand the cyclic loading from vehicles without failing through static or cyclic loading (Northmore & Tighe, 2012b). In the field these panels would be installed on a structured base, be it compacted granular materials or a paved asphalt or concrete structure, which provides greater support to the panel and must be taken into account during material selection.

The second major structural requirement is that the surface of the panel must provide adequate friction for vehicles to safely travel across it. This is a major challenge as the surface must also be transparent enough to allow solar radiation to reach the solar cells embedded within the structural layers and any sort of texturing could impair light transmission if not designed properly (Northmore & Tighe, 2012b).

Since modern high-efficiency solar cells are made from brittle silicon wafers, a solar road panel design must allow load to be bypassed around the cells. This can be accommodated by cantilevering the transparent layer over the solar cell compartments, however the transparent layer would then need to be strong enough to not deflect onto and load the solar cells (Northmore & Tighe, 2012b).

The panel also needs to be designed in such a way that it is weatherproof. This is important for both structural and electrical reasons as water and contaminant penetration would degrade the structural integrity of the composite panel and damage the embedded electronics (Northmore & Tighe, 2012b).

3.1.1.2 Electrical Requirements

Many of the electrical design requirements focus on the exposure of the photovoltaic cells to solar radiation and the physical robustness of the electrical circuit formed between the individual cells.

Shading is a major issue for photovoltaic panels because cell area that is not exposed to radiation is not able to operate as a part of the electrical circuit and this quickly degrades the performance of the panels. Since the design requires the solar cells to be recessed from the transparent layer, care needs to be taken to ensure the ledges of the structural layers do not cause internal shading on the solar cells. Additionally, debris collecting on the surface would need to be removed through street sweeping, rubber removal, or other processes if it begins to impact the overall radiation reaching the solar cells (Northmore & Tighe, 2012b).

In addition to the solar cells being very fragile components, the connecting links between the cells are also very fragile. The cell interconnections are typically a tin-lead ribbon that is soldered to the top of one solar module and the bottom of the next one in the series. In a solar road panel these connections would need to be more robust due to the higher loadings on the panel and the larger distances between solar cells due to the ribs in the structural layer design (Northmore & Tighe, 2012b).

3.1.2 Material Analysis

Due to the contrasting material requirements for the structural and transparent layers of the solar road panel design concept, as was shown in Figure 1-2, the material analysis for these layers was completed separately.

3.1.2.1 Structural Layers

As identified in the literature review, many non-traditional pavement materials have demonstrated adequate performance as a reinforcing layer for soils with poor subgrades. This indicates that there should be many options available for use in the design of solar road panels as it is expected they would always be installed on at least a properly compacted subgrade layer.

As was shown in Figure 1-2, the structural layers of the solar road panel are the optical and base layers within the conceptual design model. The main requirements for the material selection for these layers are that the material should be able to provide adequate structural performance for the panel, as defined within the design requirements, and that the material be suitable to easy in-house prototype construction. This second requirement is of key importance due to the use of this prototype as a current and future research platform.

With these requirements in mind, the candidate materials identified for the structural layers were A36 steel, 6061-T6 aluminum, and fiberglass reinforced polymers (FRPs). The mechanical properties of these materials are identified in Table 3-1 with the same properties of traditional pavement materials used in Ontario for comparison.

Table 3-1: Structural layer material mechanical properties

Category	Material	Compressive Yield Strength (MPa)	Young's Modulus (GPa)	Density (g/cm^3)
Structural	Steel – A36 (ACI, 2013)	152	200	7.85
Structural	Aluminum – 6061-T6 (ACI, 2013)	276	68.9	2.70
Structural	GPO-3 Laminate Fiberglass (Rochling, 2013)	55	12	1.90
Structural	HDPE – Glass Fiber Filled (ACI, 2013)	36.9	7.38	1.25
Structural	ABS – Glass Fiber Filled (ACI, 2013)	120	5.55	1.56
Pavement	Concrete Pavement (ARA, 2011)	32	29.6	2.32
Pavement	Asphalt Pavement (AASHTO, 1993)	N/A	2.76	2.46

In terms of material performance one of the major objectives is to minimize deflections within the panel due to external loading in order to protect the solar cells. To this end A36 and 6061-T6 are the best options due to their high compressive yield strength and Young's modulus; meaning they can withstand large loads and require large loads before substantial deformation occurs to the material.

The yield strengths for the FRP materials are more comparable to the ultimate strength of typical concrete pavements, however the Young's modulus only being two to three times that of a typical asphalt pavement indicates that these materials are more prone to high strains under low loads given a comparable cross section to the A36 and 6061-T6 options.

Typically the major benefit of the comparatively high strengths of metals over polymers is that you are able to use less material to obtain the same level of performance, thus having an overall lower cost and lower weight component. While this was demonstrated in several of the landing mat designs covered in the literature review, minimizing the material used like this may not be possible in the prototype design in order to accommodate the electronics, glass, and housing with readily available components.

Another challenge with the structural layers is choosing a material that is cost effective for building a prototype out. This creates a large difference between the available material options as the ideal way to construct the details for the optical layer out of a metal is through a casting operation while the ideal method for the fiberglass is through customized multi-ply construction. Both of these processes are very complicated and expensive to accomplish, though for the purposes of developing a one-off prototype it is simpler to go with a multi-ply fiberglass approach. The simpler alternative to these is purchasing sheets of the respective material and then cutting them down to the required sizes, which is not structurally optimal due to the epoxied ribbing but allows for simple construction of the layers out of any desired material.

One major area where these materials differ is on environmental resistance. Steel and aluminum would both require coatings to protect them from rusting and from being conductors of the current flowing through the panel from the photovoltaic system. The two glass-filled polymers both have typically poor environmental resistance as the polymer matrix degrades in corrosive environments. The GPO-3 material is designed to be an electrical insulator and also be inert in challenging conditions.

3.1.2.2 Transparent Layer

There are naturally less material options for the transparent layer of the solar road prototype due to the layer needing to be optically transparent. This limited selection down to acrylic, polycarbonate, and tempered glass as these are typical materials used in transparent structural applications, with the respective mechanical properties as shown in Table 3-2.

Table 3-2: Transparent layer material mechanical properties

Category	Material	Compressive Yield Strength (MPa)	Young's Modulus (GPa)	Density (g/cm^3)
Transparent	Acrylic – Optical Grade (ACI, 2013)	95.0	2.87	0.655
Transparent	Polycarbonate – Optical Grade (ACI, 2013)	70.0	2.35	1.13
Transparent	Tempered Glass (Alsop & Saunders, 1999)	>5000[1]	72.0	2.50
Pavement	Concrete Pavement (ARA, 2011)	32	29.6	2.32
Pavement	Asphalt Pavement (AASHTO, 1993)	N/A	2.76	2.46

Note 1: Tempered glass fails due to the tensile reaction from compressive loading before compressive yielding is achieved

These materials all demonstrate higher compressive strengths than typical concrete pavements, which indicates that they should all be able to operate as a transparent layer within a solar road panel through diligent design. The large structural difference comes through the Young's Modulus of the materials, as tempered glass is far more rigid under loading than concrete while acrylic and polycarbonate will be nearly as flexible as an asphalt pavement is currently. This could cause issues in designing the transparent layer for the polymer materials as they are cantilevered over the solar cells and large deflections should be avoided as they may cause damage to the solar cells.

Another large difference between these materials is the way in which they are most likely to fail under loading. As was identified in the literature review, polymer materials under vehicle loading typically demonstrate plastic deformation through rutting and shoving of the top layers of the cast material. Also, the optical grade versions of these polymers, which are required in order to maximize the solar energy that is able to reach the photovoltaic cells, are typically specified for temperatures above 0°C, meaning that they should not perform as well as expected under typical Canadian winter conditions.

The tempered glass, on the other hand, does not fail through plastic deformation like the polymer options though this means there is less indication of performance loss before failure. In order to safely design a tempered glass panel it must conform to typical glass flooring standards, so the structure must use multiple redundant panes of tempered glass which are laminated together, for reasons outlined in the literature review. The tempering process also means that should a pane catastrophically fail it would break into very small shards instead of large sheets of glass while the lamination also helps bind these broken shards to the other layers of glass in the panel instead of spreading into the rest of the environment.

The last set of important differences between these materials is in cost and texturing. The tempered glass is substantially more expensive a design option than the cast polymers, especially since this would have to be outsourced for the construction of the CPATT prototypes. Also, all of these materials can have surface textures applied to them through a number of processes during casting or in post-processing through etching.

3.1.3 Electrical System Design

After identifying the materials available for use in the design of the solar road panel prototypes it was important to identify how the electrical system would be installed within the panel. This consists of three segments; photovoltaic cell selection, cell interconnection, and external hardware.

3.1.3.1 Photovoltaic Cell Selection

As the focus of this thesis is on the structural design of the panel, it was decided that the electrical system would use conventional high-efficiency components and allow for future testing of additional solar technologies in solar road panel applications. To this extent, the selection for the solar cells was narrowed to monocrystalline silicon cells.

Monocrystalline silicon photovoltaic cells are available in a variety of sizes to meet various needs in custom OEM products. The typical size used in utility power generation applications is 150-mm square solar cells, as these can be produced efficiently with relatively high energy conversion rates. Since 150-mm is a large area to cantilever the transparent material over, the decision was made to use the next size down of high efficiency solar cells; 125-mm square solar cells. These still leave a lot of the surface area of the panel available to generate electricity while leaving plenty of space for load transfer around the solar cells. Additionally, due to packaging requirements for the scaled prototype, the 125-mm cells proved a better fit that the 150-mm cells as demonstrated further in this section. Figure 3-1 shows the dimensions of the solar cell selected for this project, where all of the specified dimensions are in millimetres.

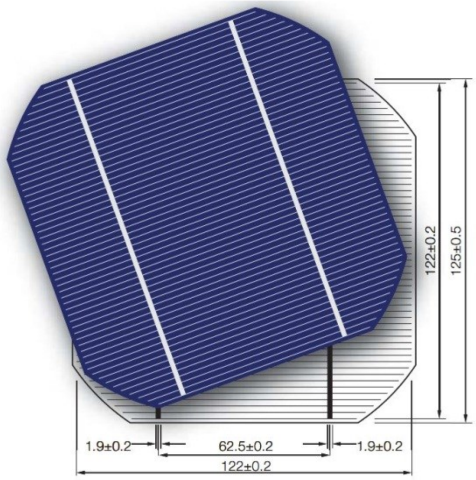

Figure 3-1: 125 mm square monocrystalline silicon solar cell (RMSolar, 2012)

This solar cell selection allowed the DMSolar DMS-125M-280 photovoltaic cell (RMSolar, 2012) to be used in the design of the prototype panel. This cell has a maximum power point voltage and current of 0.521-V and 5.342-A respectively. Due to the smaller size of the cells it is possible to fit 25 of them into each square metre of solar road panel, resulting in a total output voltage of 13.025-V and a peak power output of 69.58-W.

3.1.3.2 Cell Interconnection

As identified in Chapter 2, the typical interconnection method between photovoltaic cells in a solar module is to solder a tin-lead ribbon to the bus-bars on the top of one cell and the bottom of the adjacent cell. This works well in conventional solar module manufacturing due to the low loads placed on the connections and due to the cells being adjacent to each other with only minimal cell separation; as already identified, neither of these conditions are going to be available in the design of a solar road panel.

To accommodate this, the cell interconnection was designed to be a hybrid between traditional tin-lead ribbon and electrical wire. The soldered ribbon is still required to ensure a solid connection between the cell’s bus-bar and the electrical conductor, but the ribbon will only be extended as a small tab off of the solar cell and an electrical wire will be soldered between the soldered tabs of adjacent cells (Northmore & Tighe, 2012b). 22-gauge wire was selected for this application due to the expected electrical load throughout the module. This wiring will be done as per the schematic shown in Figure 3-2.

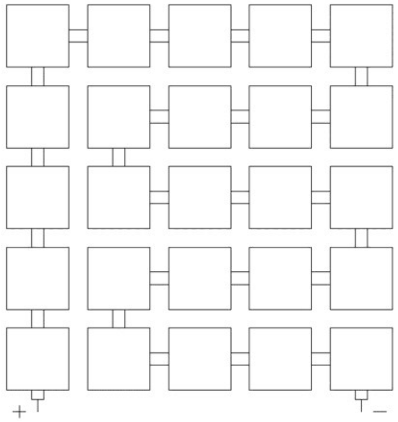

Figure 3-2: Schematic solar road panel interconnection scheme (Northmore & Tighe, 2012b)

3.1.3.3 External Hardware

In addition to the electrical circuit built within the panel, a reverse current protection diode is required to ensure that no current is allowed to pass in the wrong direction through the panel as this would result in destroying the sensitive electronics. To simplify packaging it was determined that this would be done externally to the panel with wire connections to a barrier strip that integrates the reverse current protection diode. The diode selected for this provides reverse current protection of up to 5-A on voltages up to 40-V; sufficient for the design parameters of the prototype solar road panel given that the panel can be handled such that only a minimal reverse current would be subjected to it.

3.1.4 Transparent Layer Design

Due to the demonstrated rutting performance of transparent polymers it was determined that the prototype panel should have a tempered glass transparent layer. The use of a polymer material would require a maintenance program to be established which replaces the transparent layer of the panels periodically and the low Young’s modulus means that there would be large deflections of the transparent layer through the optical layer.

With the material selected, the most important design property to determine from a structural standpoint is the thickness of the transparent layer. Due to safety considerations it is important to have multiple panes of glass laminated together to support the loading, and in this case a two-pane configuration was selected such that should one pane break the other would be able to support the vehicle load by itself. Under this condition it is known that the design stress for tempered glass members is 42-MPa (Alsop & Saunders, 1999).

With these conditions it was possible to determine the bending stress that would be found in a cantilevered section of the glass. It was assumed that the cantilevered sections would be 140-mm square, large enough for a 125-mm solar cell and interconnection space, and that the highest load condition would see an even distributed load from a passing vehicle tire, assumed to be 480-kPa of pressure. This information was applied to correlations developed for stress relations (Roark & Young, 1975), using low bending theory, and the results for varying pane thicknesses are shown in Table 3-3.

Table 3-3: Maximum transparent layer bending stress as a function of glass pane thickness

Thickness (mm)	**6**	**8**	**10**	**12**	**14**	**16**	**18**	**20**
Maximum Bending Stress (MPa)	75.11	42.25	27.04	18.78	13.80	10.56	8.345	6.760
Maximum Deflection (mm)	0.5415	0.2284	0.1170	0.06769	0.04262	0.02856	0.02006	0.01462

As demonstrated, all of these configurations give very minimal deflections even when using thin layers of tempered glass, which validates the use of the low bending theory assumptions. For individual panes of glass the minimum usable configuration is the 10-mm design, so two 10-mm panes were determined to be used in the solar road panel prototype.

In order to make the glass structure usable in a solar road panel, a texture must be applied to the surface and accommodation must be made for the panel to be packaged together by a frame. Since the primary focus of this research is on the structural characteristics of a solar road panel and not the functional ones, a simple etching pattern was chosen from the catalogue of the supplier of the glass structure. This texture will add some tractive capacity to the panel while also not degrading the optical quality too severely.

In order to frame the panel, it was determined that the best approach to ensuring the glass is secured into the panel was to design a ledge into the overall glass panel structure. This was done by using two 10-mm glass panes cut to different square sizes and centred upon each other during lamination. An image of the designed glass layer can be found in Figure 3-3.

3.1.5 Structural Layer Design

Since each of the steel, aluminum, and fiberglass materials that were analyzed will provide sufficient performance for the structural layers of the solar road panel prototype, emphasis was placed on manufacturability when making the final material selection. The metals would have to either be cast, laser cut, or water jet cut in order to produce the required elements in the design while the fiberglass can be cut to size using standard equipment. For this main reason the prototype structural layers were made from GPO-3 rated fiberglass.

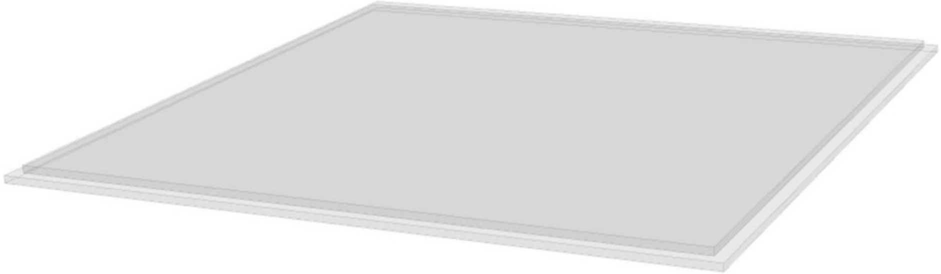

Figure 3-3: Solar road panel prototype transparent layer

3.1.5.1 Structural Layer Thickness

The next step in the design of the structural layer was to determine the overall thickness of the panel. This was largely based on the availability of components, as the transparent layer, structural layer, and frame all have to fit together to make one complete prototype panel. With the glass thickness determined at 20-mm, the next step was finding a frame size that would be appropriate for the overall structure.

When designing a road-testable prototype, the frame of the panel is going to have a significant impact on the overall structural performance due to load transfer characteristics. For the purposes of this study, where the prototype panel is being constructed at a smaller scale than a full-sized road panel would be, the frame should have minimal impact on the performance of the transparent and structural layer materials. The frame material should also be readily available and easily workable; to this end it was determined that the frame should be made out of 6063T5 aluminum channel members.

With the material selected, the options for the overall panel thickness were narrowed down. Typical 6063T5 channel is available in 25.4-mm [1-in], 38.1-mm [1.5-in], 50.8-mm [2-in], and 76.2-mm [3-in] channel widths, which is the governing dimension for the panel thickness. With the glass requiring 20-mm of thickness, it was determined that 50.8-mm is the minimum usable channel size to allow for multiple layers of fiberglass to compose the optical and base layers. In terms of structural performance a greater thickness of fiberglass would provide more resistance to bending, however due to practical limitations on fiberglass availability the 50.8-mm channel thickness was chosen over the 76.2-mm channel.

3.1.5.2 Optical Layer Design

The transparent layer and frame design effectively leave 31.75-mm [1.25-in] of space for fiberglass structural layers. Since the base layer should be as thick a layer of fiberglass as possible, the optical layer was designed first as it has more detailed design requirements.

Overall the optical layer of the solar road panel prototype needs to be thin in order to minimize solar cell shading, as outlined in the design requirements. This layer also needs to allow for cutouts to be made for cell interconnections, making it easier to design a two-layer structure for the optical layer; one with the cutouts for interconnections and one without to support the transparent layer.

GPO-3 laminate fiberglass is readily available in thicknesses at increments of 3.175-mm [0.125-in]. In order to keep the material thickness consistent between the optical and base layers, reducing the amount of material required, it was decided that only 6.35-mm [0.25-in] and 12.70-mm [0.50-in] thick fiberglass sheets would be used.

This meant that the optical layer would be designed as two layers of 6.35-mm cast fiberglass sheet. The pattern used for this layer is shown in Figure 3-4 and accommodates the 125-mm solar cells with 6.35-mm of space around the edge to allow for the interconnections to be routed.

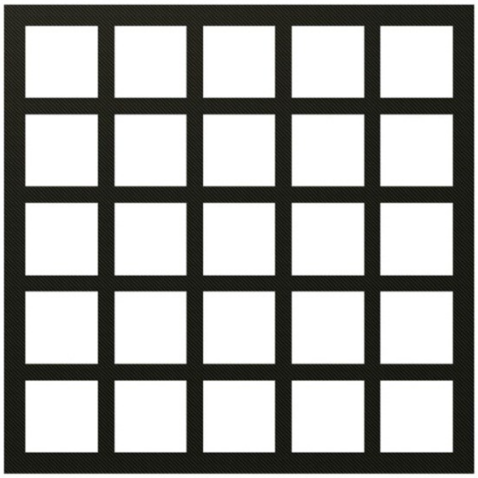

Figure 3-4: Cell compartment accommodation in the optical layer

In order to make the cutouts in the optical layer for the solar cells, the grid pattern was broken down into smaller rectangular bars that could easily be manufactured with a chop-saw that was available for use. At full scale production this would be completed through laser or water jet cutting.

3.1.5.3 Base Layer Design

With the optical layer having a total thickness of 12.70-mm, there are 19.05-mm [0.75-in] remaining for the base layer. Due to the material thickness decision outlined above, this is easily consumed by two plates of fiberglass; one 12.70-mm plate and another 6.35-mm plate. In order to accommodate the frame design, a lip was required around the base layer just like was included in the design of the transparent layer. This was accommodated by dimensioning the 6.35-mm plate to a smaller size than the 12.70-mm plate and centring them upon each other, similarly to the transparent layer. An image of this setup can be found in Figure 3-5.

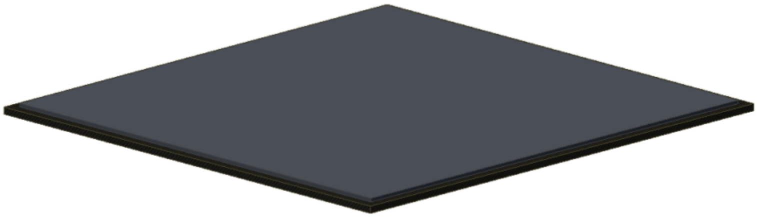

Figure 3-5: Base plate configuration

3.1.6 Frame Design

As was outlined in 3.1.5.1, the frame is being constructed from 50.8-mm [2-in] 6065T6 aluminum C-channel. In order to provide a physical bugger between the frame and the structural and transparent materials within the panel, weather-stripping and foam inserts were added as shown in Figure 3-6.

Figure 3-6: Assembled frame member

3.1.7 Prototype Model

The overall panel was then assembled as shown in Figure 3-7 and detailed drawings for each component can be found in Appendix A.

Figure 3-7: Solar road panel prototype model

3.2 Construction

The construction of the prototypes was completed at CPATT at the University of Waterloo between the lab facilities on campus and at the Region of Waterloo Emergency Services Training site. Since the focus of the prototype is for determining the structural panel performance the construction of the electrical subsystem elements has been omitted.

3.2.1 Bill of Materials

The itemized bill of materials for the assembly of the prototypes can be found in Appendix B. The majority of the structural materials were purchased in bulk and fabricated in-house as outlined in the rest of this section, however the transparent layer was outsourced to All-Brite Glass and Tint due to the complexity of glass fabrication. This glass layer is as shown in Figure 3-8.

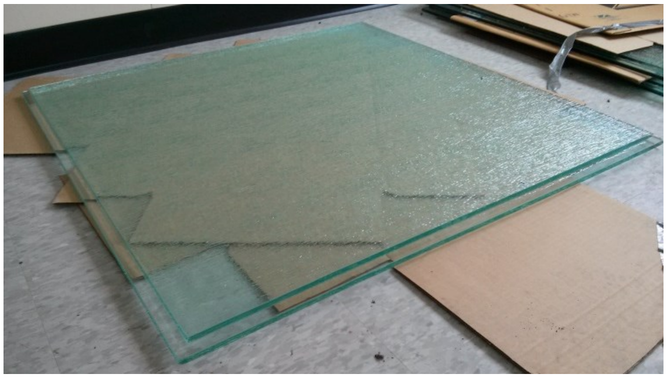

Figure 3-8: Glass transparent layer

3.2.2 Fiberglass Fabrication

As outlined in the Bill of Materials, the fiberglass was all purchased in 6.35-mm and 12.70-mm plates and then cut to size in-house for assembly into the solar road panel prototype.

3.2.2.1 Base Layer Fabrication

The base layers of the solar road panel prototype require large, solid, square plates of fiberglass cut to sizes just under 1-m. This was accomplished across three stages where the first, as shown in Figure 3-9, was to mark out the required area and use a circular-saw with laminate rated blades to trim the bulk of the excess material from the edges of the panel.

Figure 3-9: Base layer fiberglass cutting

With the bulk of the material trimmed away, the second stage of fabrication was to sand the edges of the panel down to the proper, square dimensions using a palm sander and coarse sanding pads. The faces of the two pieces to be epoxied together were also sanded to improve bonding.

The final stage was to epoxy the two base plate materials together to form one large block of fiberglass material with the designated lip for the housing. This was accomplished as shown in Figure 3-10.

3.2.2.2 Optical Layer Fabrication

As outlined in the Optical Layer Design section, the fiberglass members for this portion were cut into strips small enough so that fabrication could be completed using a chop-saw. Optimally this would be done with a table saw, laser cutter, or water jet cutter but none of these were readily available with adequate ventilation.

Figure 3-10: Base layer fiberglass epoxying

The first stage of this fabrication was done by using a circular saw to cut the large fiberglass sheets into portions that could be further cut-up by the chop-saw. All of the sheets required were divided into sections for the three different piece sizes that make up the optical layers and taped off to designate cutting lines. This overall process is demonstrated in Figure 3-11.

Figure 3-11: Optical layer fiberglass sheet trimming

With the fiberglass sheets trimmed, the next step was to use the chop saw to cut the lengthwise dimensions of the fiberglass pieces. This was accomplished by setting up the chop saw to the designated specimen width and then sequentially trimming the required width one piece at a time, as shown in Figure 3-12.

Figure 3-12: Optical rib cutting with a chop saw

With the correct width of each specimen achieved, the third step was to square one end of each member so that the pieces could be trimmed to the correct length. This was not required for members that were adjacent to the edge of the finished cast panel, as it was assumed that the acquired fiberglass sheets were square enough for our purposes.

With three of the edges squared, the next step was to mark each of the pieces for the correct length so that the last end could be trimmed off and the parts would be the correct dimensions. This was done in the lab with all of the pieces marked as shown in Figure 3-13.

The fifth step was to then trim off these ends to finish the fiberglass pieces. This process was accomplished in a similar fashion to what was shown in Figure 3-12.

With all of the pieces cut to the appropriate size, the sixth step was to measure and sort the pieces by the critical dimension. In the case of the short ribs this was the length while this dimension was the width of the long rib and edge members. These dimensions were identified as critical because they were what would collectively add up to the overall panel dimension in the direction with the most cuts, meaning that there were more opportunities for compounding dimensional errors to add-up.

Figure 3-13: Fiberglass ribs marked for trimming

Then, the pieces were all arranged and taped in the pattern required for the optical layer. After the taping, the pieces were untapped individually so that all of the connection pointes could be sanded manually and epoxied using a standard 2-phase epoxy. The pre-epoxied layout of these pieces is shown in Figure 3-14 while the epoxied joints are demonstrated in Figure 3-15.

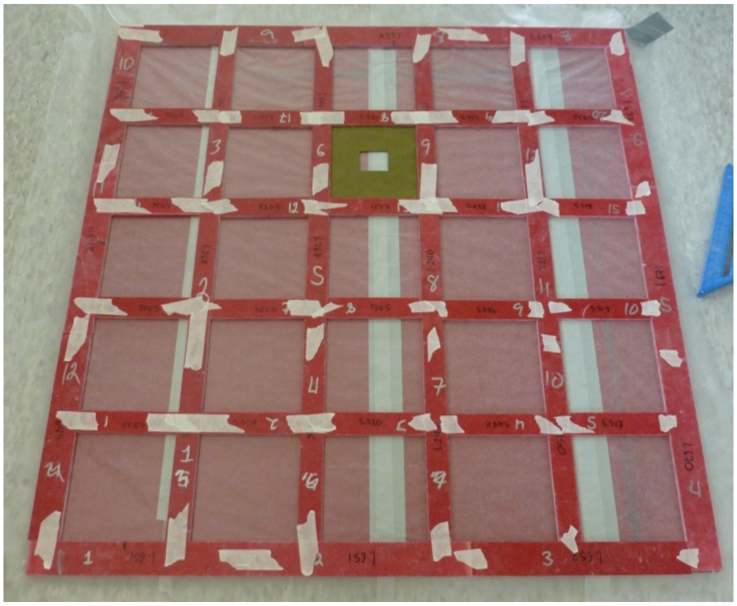

Figure 3-14: Optical layer pre-epoxying

Figure 3-15: Optical layer epoxied joints

The last step of fabricating the optical layer is to sand down the epoxy on the top and bottom of the panel as well as around the edges of the fiberglass to make the layer conform with the required dimensions. The end result of the sanding is as demonstrated in Figure 3-16.

Figure 3-16: Optical layer post-sanding

3.2.3 Housing Fabrication

The housing of the panel is constructed out of aluminum C-channel and various weather-stripping and edge sealing components. The first step in fabricating the housing is to take the aluminum frame members are trim and angle the ends to a 45° profile.

The next step involved cutting and applying a plastic edge trim to the edges of the aluminum frame members. This was completed to protect the structural materials of the solar road panel prototypes from contact with the frame members.

The last step involved cutting and applying weather-resistant foam to selective internal portions of the aluminum frame. This was done to create a flexible buffer between the structural materials and the frame so that hard contact would be minimized. The foam inserts also helped make-up gaps between the frame members and the structural materials. The end result of the edge seal and foam application to a frame member is demonstrated in Figure 3-17.

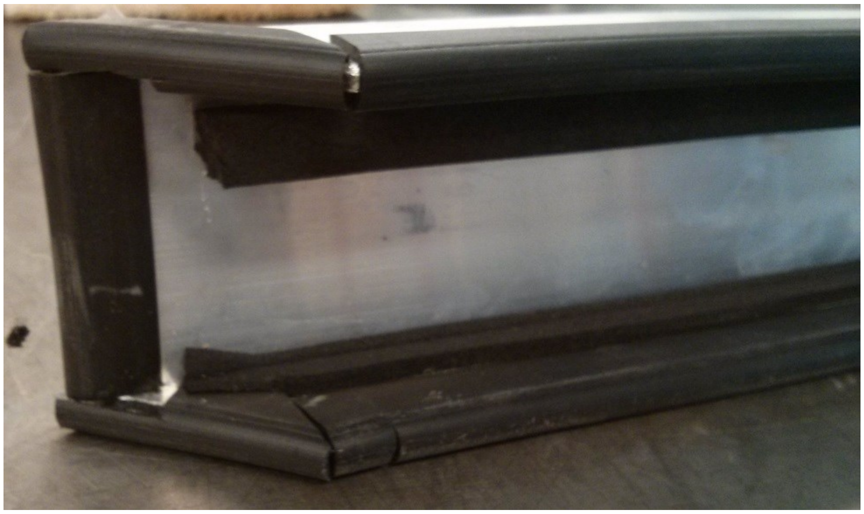

Figure 3-17: Housing frame with edge trim and foam inserts

3.2.4 Panel Assembly

The final panel assembly was accomplished by stacking all of the structural layers in order. This resulted in a composite structure which, from the bottom up, consisted of the epoxied base layer, two optical layers, and the acquired tempered glass structure. The frame members were then positioned around the edges of the panel and held in place with tie-straps while the corners were taped to hold together. The resulting final assembly is as shown in Figure 3-18.

3.2.5 Lessons Learned

One of the most important lessons learned was that the ideal structural way to fabricate the fiberglass layers is not possible in-house without extensive knowledge of fiberglass fabrication. To create a multi-ply fiberglass layup of the required parts required external expertise. All of the identified research showed that multi-ply areas of fiberglass were the optimal option for the study, but after several attempts it was determined that precast fiberglass laminate would have to be used due to the challenges of working with multi-ply fiberglass.

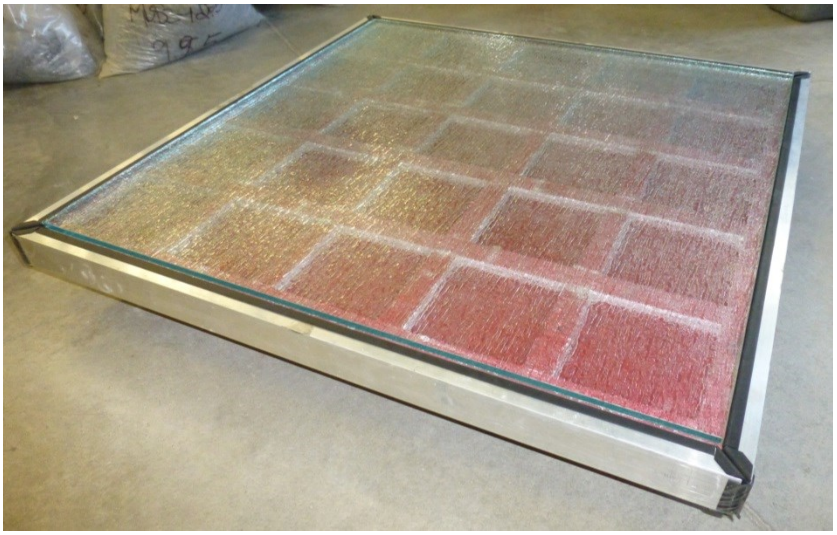

Figure 3-18: Completed structural solar road panel prototype

It was also noted, approximately a year after the glass was acquired from the supplier, that their recommended glass structure for this application had changed from being two panes of tempered glass laminated together into using a traditional bulletproof glass type structure. This tends to use thinner panes of glass and a larger resin layer to protect from impact loading, though it is also unknown how the thicker resin layer would impact on the rutting and deformation performance of the transparent layer.

It was also learned, while cutting the base layers of fiberglass, that the optimal method for using a skill saw to cut through such large blocks of material is to alternate cutting two close parallel lines. Trimming at the edges of the fiberglass plates was not challenging, as the material was able to bend away to make room for the saw blades to cut through. However, whenever an interior cut had to be made, the circular-saw would bind too easily if a relief line was not being cut right next to it. This helped speed up the process of cutting and reduced the number of saw blades that needed to be purchased.

Chapter 4

Testing and Analysis Methodology

With the prototype panel now designed and constructed, the testing and analysis methodology can now be outlined. This work is largely divided into three categories: structural testing, FE analysis, and environmental testing.

4.1 Structural Testing

The purpose of the structural testing was to perform a controlled test on the prototype solar road panel to determine how the panel deflects when various loads are applied. The output of this test is to validate the design of the prototype that was outlined in Chapter 3 and to act as an input for the FE analysis outlined in Section 4.2 below.

This is largely broken into four segments: determining the testing objectives, test frame design, load apparatus design, and instrumentation.

4.1.1 Testing Objectives

Since the overall output of this testing is to serve as an input to the FE analysis of this research, the specific objective of the structural testing is to determine the flexural response of the designed prototype panel to specific low loadings in a manner that can be easily duplicated within the FE software.

The testing should specifically allow for variable loading and variable load application, to ensure that performance of the composite panel is truly consistent. Testing will be performed for static response and within the elastic range for all materials in question, as the static, low load response will be sufficient to determine the comparative response of a panel with in-situ loading.

4.1.2 Testing Frame

A number of designs were considered before establishing that the most feasible option for the testing frame was to build a structure, as shown in Figure 4-1, where a freely supported prototype could be installed upside-down and loaded from underneath.

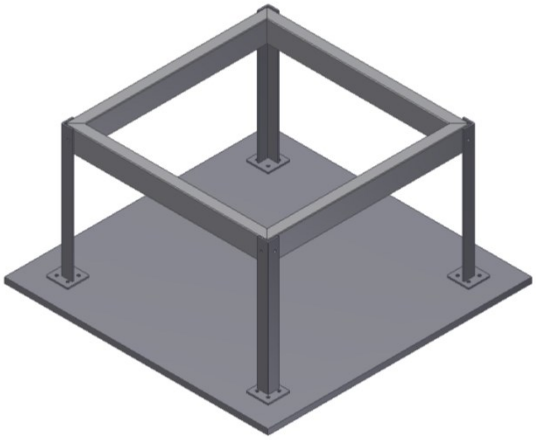

Figure 4-1: Structural testing rig schematic

4.1.2.1 Test Frame Configuration

A number of configurations were considered for this testing frame, including confined pavement testing, adapting an existing test frame, and a top loading frame, but these were all rejected for the bottom loading frame for a number of technical or feasibility considerations.

The confined pavement testing, while providing the best representation of how the prototype would function in in-situ conditions, would provide very specific results depending on the granular materials used. This would also be more challenging to duplicate in FE analysis, as the viscoelastic properties of the soil base materials would have to be modeled while determining the overall panel properties. The cost of this structure would also be the highest, as a steel box would need to be procured for the testing and a frame would need to be developed to apply the loading.

Adapting an existing test frame was quickly discarded as an option due the expected loading requirements on a freely-supported panel. Initial analysis of structural loading on the glass panel, as shown in Figure 4-2, determined that the prototype would need to be tested at up to 4,448-kN [1,000-lbf], which would only produce a deflection of 0.84-mm [0.033-in], to ensure it does not fail under brittle conditions during testing. The actuators and load cells on the existing test frames are not sensitive enough to operate safely at this resolution, especially as there are only a few prototypes being made for all forms of testing and analysis.

The top loading frame was rejected for the bottom loading frame because of the manner of loading. A top loading frame would require a structure to be built to support the load apparatus, which also makes repositioning the load between tests more cumbersome. A bottom loaded frame structure uses the base of the testing rig and strong-floor of the structures lab as structural support, making it a simpler and more efficient design. There are no downsides to testing the panel upside down, as gravitational forces can be accounted for within the FE model easily.

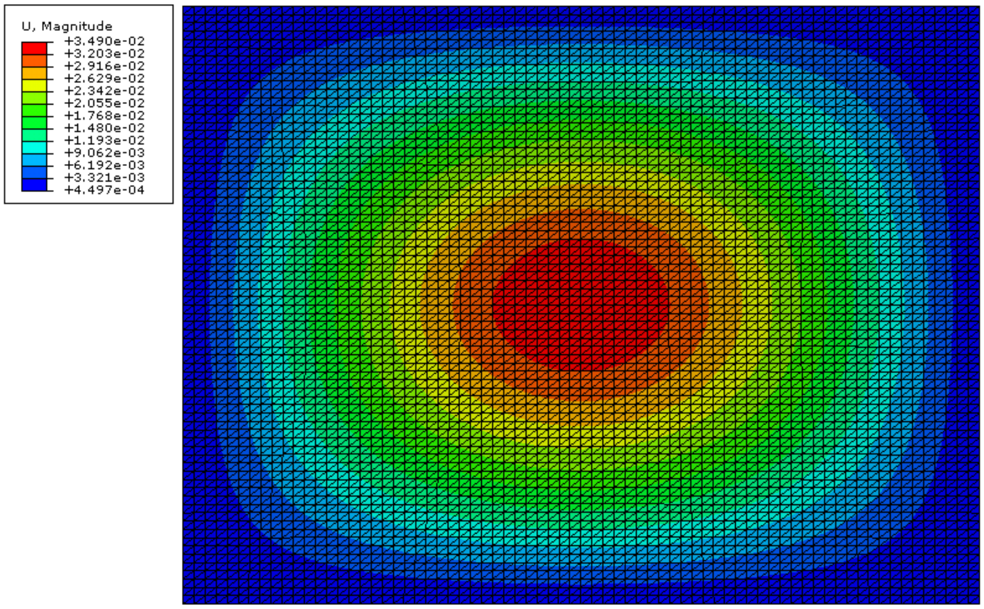

Figure 4-2: Deflection response of simulated panel to a centred 4,448-N [1,000-lbf] load

4.1.2.2 Test Frame Design

As demonstrated in Figure 4-1, the design of the frame was kept as minimal as possible to decrease the cost of the frame and make it easier to store after testing.

It was initially determined that an existing reinforced steel plate could be used as the base plate for this testing rig. The plate, 1.5-m by 1.83-m by 0.03-m, is reinforced with 101.6-mm C-channels underneath. This provides a very stable surface for building the testing rig onto. An image of this base plate can be found in Figure 4-3.

The next major element of the testing rig is the loading ring that the panel will be loaded against during testing. This element must be extremely rigid, as even minimal deflections will affect the results from testing, as the expected overall panel deflections are on the order of 0.58-mm. After investigating some different material options a 101.6-mm [4-in] by 51.2-mm [2-in] hollow section with 6.35-mm [0.25-in] wall thickness was selected as the material for this element due to its high resistance to flexure, as demonstrated in Figure 4-4.

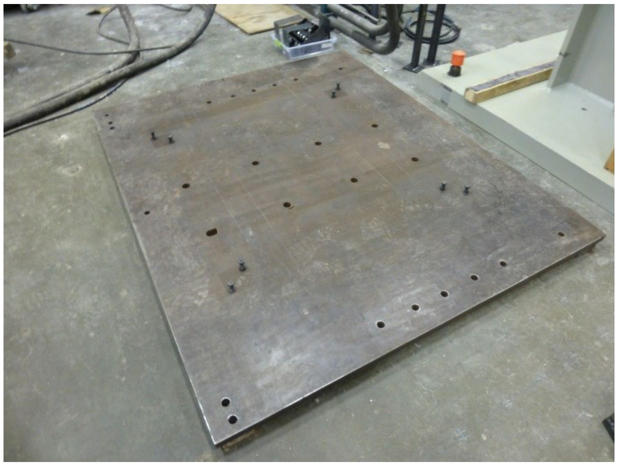

Figure 4-3: Structural testing rig base plate

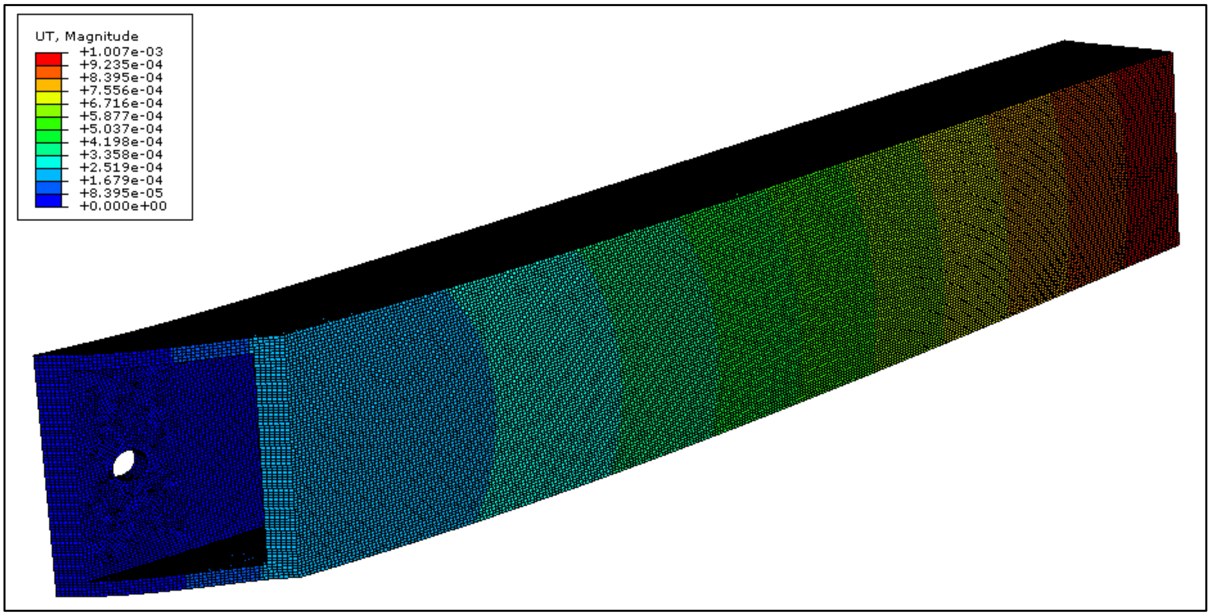

Figure 4-4: Deflection response of 101.6-mm x 51.2-mm HSS under 6,672-N [1,500-lbf] distributed load

With the material selected, it was cut and welded into a ring large enough for the panel to support itself against. This simulates a simply supported condition that can be simulated in FE software for validation of the panel model. The final product of this loading ring is shown in Figure 4-5.

Legs were also designed to connect the loading ring to the base plate while giving enough room for the load apparatus and instrumentation to be installed. Also, since this frame is expected to see limited use after this testing, the legs were designed to be removable so that the frame can easily be stored post-testing. The legs designed for this apparatus are shown in Figure 4-6.

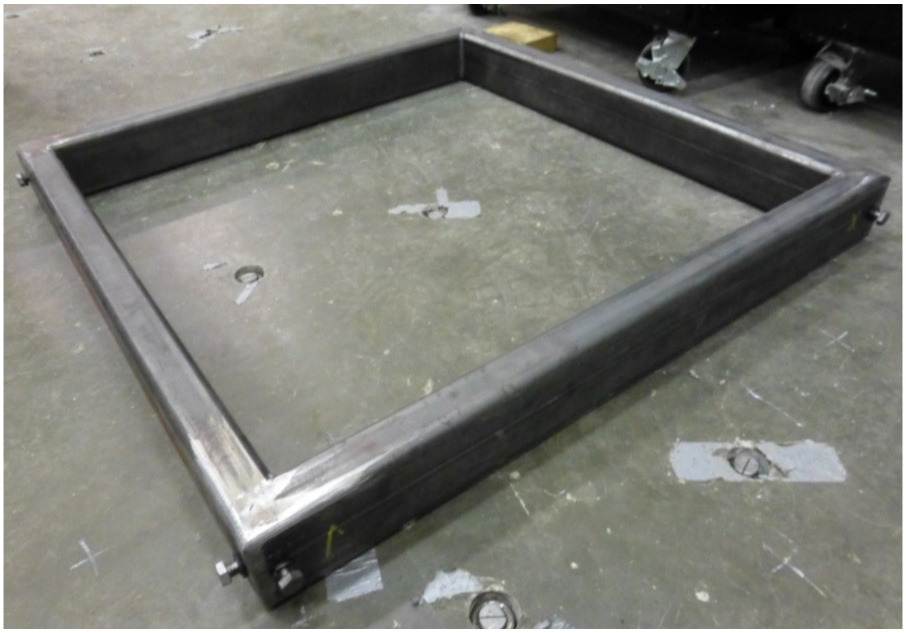

Figure 4-5: Structural testing rig loading ring

Figure 4-6: Structural testing rig legs

The final, constructed apparatus can be found in Figure 4-7 while the detailed design drawings for the structural rig can be found in Appendix C.

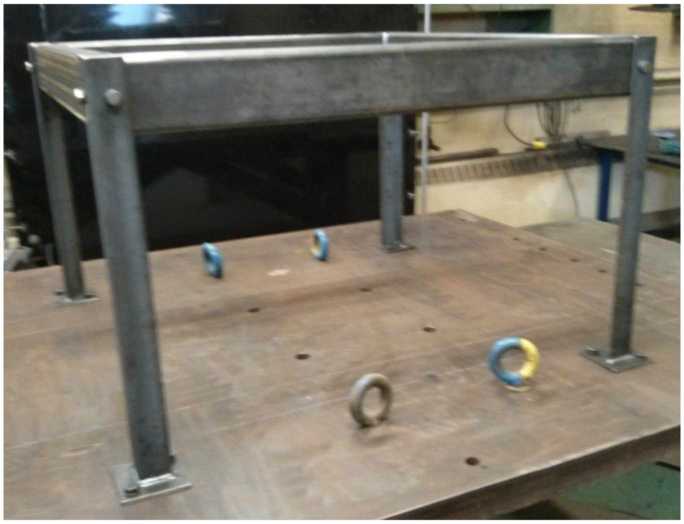

Figure 4-7: Structural testing rig

4.1.3 Load Apparatus Design

The load for testing was supplied through an air-over-oil driven actuator as shown in Figure 4-8. This system is able to use the lab's existing air supply lines to pressurize the oil to a variable pressure of up to 10.3-MPa [1500-psi]; the specification being used as a possible maximum for testing. A base was built for the actuator which allows the location of the actuator to be easily adjusted in between tests.

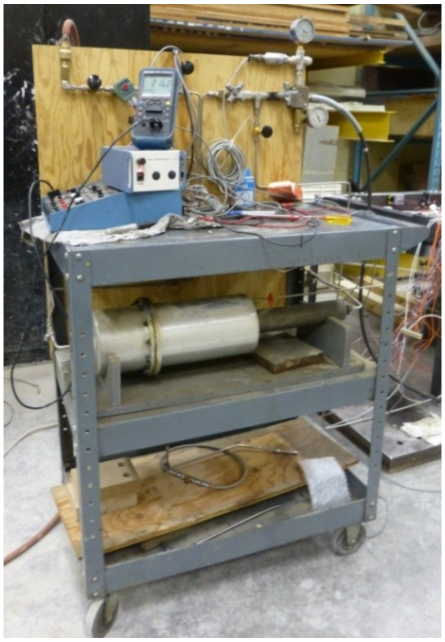

Figure 4-8: Structural testing air-over-oil system

Potential locations to load the panel during testing were all located in the middle of the optical layer cutouts. This best represents the expected high stress concentrations that would develop over these sections during vehicle loading. Each of these locations were marked on the transparent layer of the panel as shown in Figure 4-9.

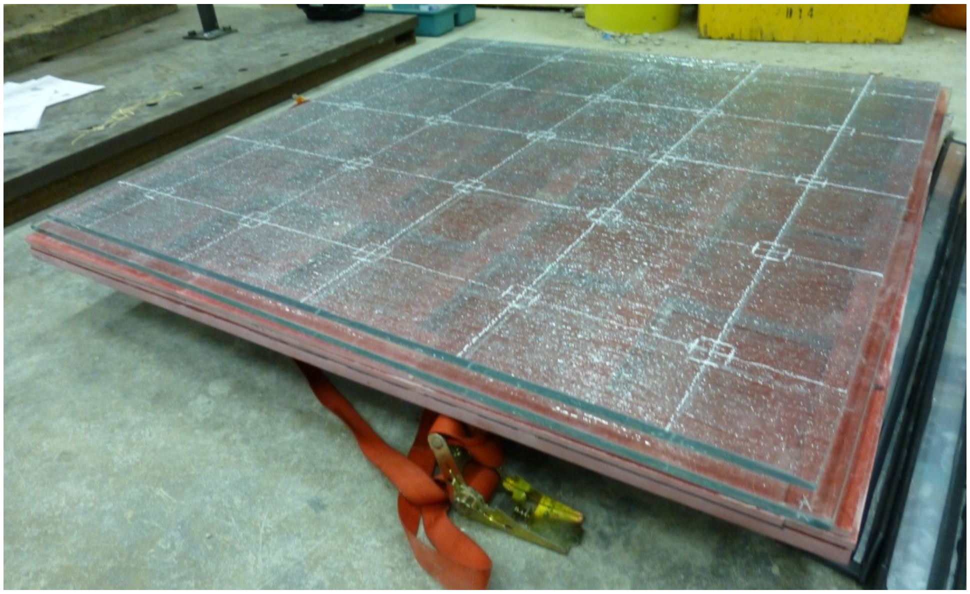

Figure 4-9: Structural testing load application points

The load being applied to the panel by a 25.4-mm [1-in] square steel surface covered in a medium-stiffness rubber. The square applicator was chosen to simplify the modeling required to validate the panel design; square areas are easier to model than circular ones. The rubber was added to ensure a smooth contact area with the textured glass panel; accidental point loading would damage the glass and cause premature failure of the prototype.

4.1.4 Instrumentation

In order to measure the output of the testing a variety of instrumentation is being used. This includes a load cell to validate the load supplied to the panel, strain rosettes adhered to the glass and fiberglass members, and LVDTs to measure the displacement of the bottom fiberglass layer.

The load cell being used to validate the loading in the panel is a StrainSert FL5U-2SPKT, as shown in Figure 4-10. This was calibrated using a 13.4-kN [3000-lbf] load ring on a range from 0 to 8.90-kN [2000-lbf].

Figure 4-10: Structural testing load cell

The instrumentation measuring the response of the panel to the loading is being instrumented over an eighth of the panel as demonstrated in Figure 4-11. This was done to minimize the instrumentation requirements while allowing for symmetry effects to be assumed from the strain and displacement responses from loading in a variety of locations around the panel. As a result, loading on reference point C-2 could be simulated through the entire panel by loading points C-2, D-3, C,-4, and B-3, for example.

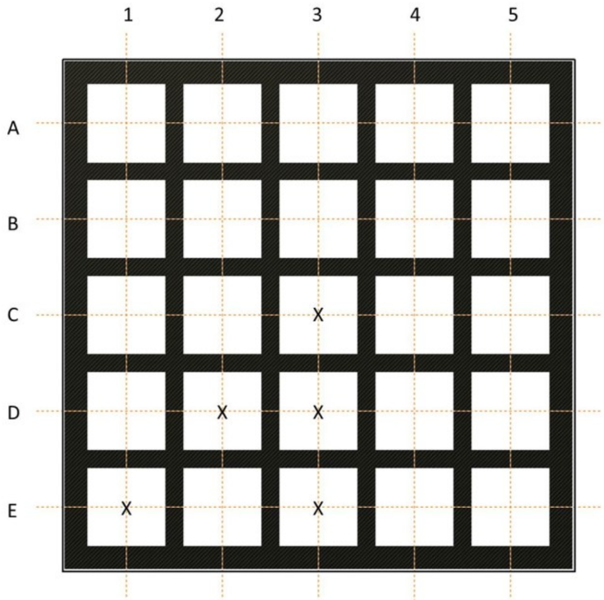

Figure 4-11: Instrumentation locations with respect to the optical layer

The strain rosettes being used for the testing are all Vishay Model C2A-06-250LR-350 rosettes. These rosettes are designed to be attached to both glass and fiberglass specimens and provide highly accurate planar strain measurements. In order to be read by the NI data acquisition system available from CPATT, the 350-ohm strain rosettes had to be shunted down to 120-ohm using a 182.6-ohm resistor being mounted in parallel across it at the datalogger terminals.

The transducers being used to measure the displacement of the fiberglass base plate are HP 24DCDT-050 units. These LVDTs allow for up to a 1.27-mm [0.050-in] displacement, which is well above the maximum expected displacement of 0.84-mm as determined from the initial FE analysis as shown back in Figure 4-2.

The transducers were mounted to the load ring of the structural testing frame using magnetic based retort stands. An image of the rosette and transducer positioning on the fiberglass base plate during testing is shown in Figure 4-12.

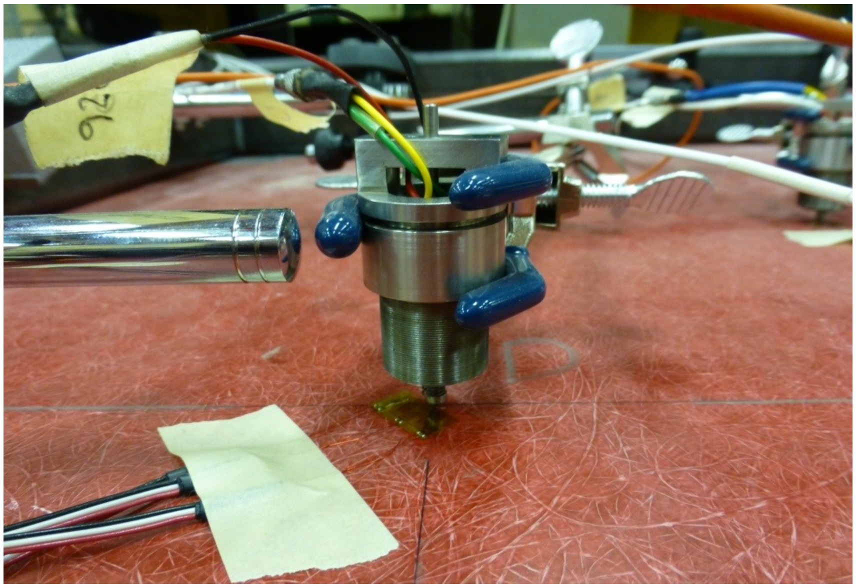

Figure 4-12: Rosette and LVDT arrangement

To collect all of the data simultaneously, a NI SCXI-1000 data acquisition system with multiple modules was used. This system was connected to a computer in the structures lab and was accessed using NI LabVIEW. The entire setup for the structural testing is shown in Figure 4-13.

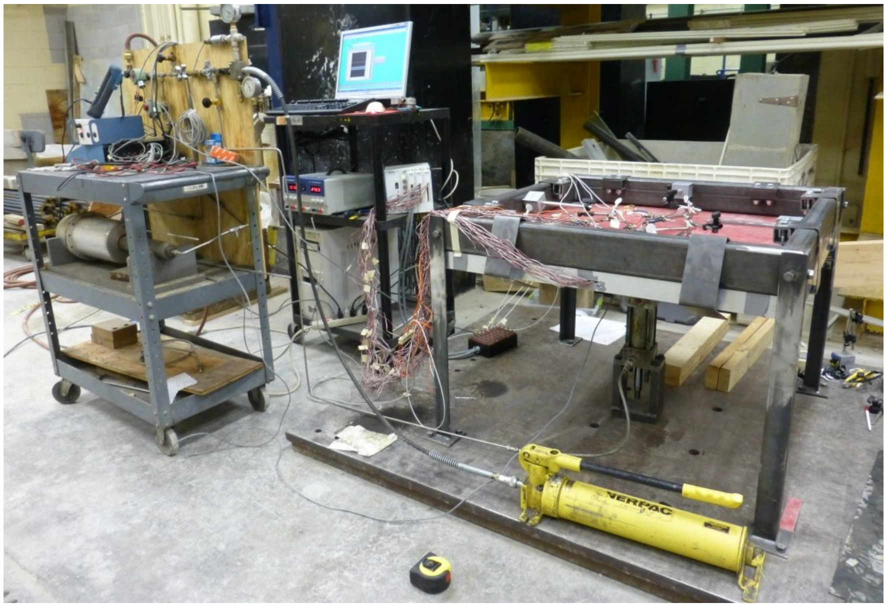

Figure 4-13: Structural testing setup

4.2 Finite Element Analysis

The purpose of this analysis is to determine the static and fatigue responses of the solar road panel prototype in potential applications in Ontario. This consists of modeling the output of the structural testing in FE software, testing this model installed on top of standard Ontario pavement and subgrade structures, and using the maximum stress output from these simulations to determine the static limits and fatigue life of the solar road panel prototype. All of the FE analysis is completed using Abaqus CAE 6.13 (Abaqus, 2013).

4.2.1 Prototype Model Development

The model development consists of two parts; the simplifications that went into making the FE model and the modeling and validation procedure used.

4.2.1.1 Model Simplifications

The aluminum frame was excluded from the model and the transparent and structural layers were extended to be 36-inch squares. This is a reasonable simplification as the aluminum frame is far less rigid than the glass being used in the transparent layer, so it will have minimal impact on the performance of the model. The validation of the model based on the structural testing will focus on modeling the internal load points to mitigate edge loading anomalies.

The fiberglass rib portion of the structural layers is modeled as a homogenous block of material with the grid of squares cut-out. This is more realistic to how a future state prototype would be fabricated, as this layer would be a customized multiply fiberglass layup, but may not accurately represent the prototype constructed with epoxied joints.

The prototype transparent layer has a textured surface but this was modeled as flat for the FE analysis. This is a reasonable approximation, as the soft rubber pad on the load applicator will evenly apply the load across the contact area.

The boundary conditions of the structural testing were approximated using a flat plate steel ring, with the same dimensions as the load ring shown in Figure 4-5, with an encastre boundary condition applied to the top face. This implies that the ring will not deflect at all during testing, which is a reasonable approximation for the highly rigid load ring.

4.2.1.2 Modeling Procedure

Due to the prototype being much wider and longer than it is thick, all of the layers of the panel need to be modeled as shell elements. This is standard procedure for elements with a thickness to length ratio of less than 1/15 (Abaqus, 2013) and allowed the transparent layer, when modeled by itself, to obtain results identical to recognized load-stress relations for simply supported flat plates with centred loading (Roark & Young, 1975).

To govern the contact between the layers of the panel model, surface-to-surface contact models were generated in the standard solver using a simple normal contact property. The slave component of the model is adjusted to remove overclosure prior to running the solver as this adjusts the three shell elements to be directly adjacent and remove displacement distance added from the shell thickness.

Due to challenges in modeling the interaction between the rigid transparent layer and the more flexible structural layers some additional solver tools were required. The normal behavior of the contact was driven by hard contact but with a standard linear penalty model applied to allow for some error at individual nodes. Similarly, a contact control was added that allows for automatic stabilization of the results using the default parameters provided by Abaqus. These techniques were both prescribed by the Abaqus user manual (Abaqus, 2013) to solve convergence issues with the modeling technique.

The two main parameters of the model validation are the meshing and the material properties. The mesh has the greatest effect on the accuracy of the FE model, with finer meshes producing more accurate results at the cost of increased computational time and memory allocation. The objective of mesh optimization is to achieve a mesh that simulates the results of the structural testing with at least 95% accuracy. This is typical of FE analysis, as increasing accuracy requires exponentially more computational time. Most studies found used an objective accuracy between 90% and 95% (Mak, 2012)(Z. Wu, Chen, & Yang, 2011).

Due to the geometry of the members structured meshes are easily generated for the transparent and base layers, which tend to provide more accurate results. The mesh strategy used for the optical layer was a free mesh, due to the continuous nature of the member with irregular cutouts. The parameters being varied for the mesh validation are outlined below in Table 4-1, with the default variables for the parametric study highlighted in bold.

Table 4-1: Prototype mesh validation parameters

Layer	Mesh Strategies	Mesh Sizing [mm]	Mesh Thickness
Transparent	**Structured**	25.4, 19.05, **12.7**, 6.35, 2.54	3, 5, **7**, 9
Optical	**Free**	25.4, 19.05, **12.7**, 6.35, 2.54	3, 5, **7**, 9
Base	**Structured**	25.4, 19.05, **12.7**, 6.35, 2.54	3, 5, **7**, 9

The material properties assumed for the materials in the prototype are as outlined in Table 4-2. The values for tempered glass are typical material property ranges as per the literature (ACI, 2013; Alsop & Saunders, 1999); the inherent imperfections in glass manufacturing leaves large margins for mechanical properties. The fiberglass laminate used in the prototype meets the NEMA GPO-3 standard, which has the supplied elastic modulus value from the manufacturer (Rochling, 2013). Poisson’s ratio is not a commonly required property of thermoset polymers, so a range of potential values was once again determined from the literature (ACI, 2013; Rochling, 2013). In order to satisfy these ranges three material property conditions were created to represent the average, most flexible, and most rigid combinations. These conditions will be modeled and compared to the results of the structural testing.

Table 4-2: Prototype material property ranges and analysis categories

Material	Property	Range	Panel Model Properties		
			Flexible	*Average*	*Rigid*
Tempered Glass	Elastic Modulus [GPa]	70 to 75	70	72.5	75
	Poisson's Ratio	0.2 to 0.3	0.20	0.25	0.30
GPO-3	Elastic Modulus [GPa]	12	11	12	13
	Poisson's Ratio	0.28 to 0.33	0.28	0.30	0.32

4.2.2 Ontario Pavement Load Cases

To determine the performance of solar road panels in typical Ontario conditions both the load conditions and structural bases needed to be determined with Ontario in mind.

4.2.2.1 Loading Conditions and Locations

There were two tire load considerations for this study; a maximum static load and a fatigue load. These loads are identified in Table 4-3 and represent the typical pavement design loads for Ontario.

Table 4-3: Tire loading conditions

Condition	Load [kN]	Contact Dimensions
Static	87.5	0.60-m x 0.25-m
Fatigue	40	0.529-m x 0.364-m

The static load condition is based on the heaviest wheel load applicable by Canadian regulations, CAN/CSA-S6 CL-625-ONT (CSA, 2006), which is in this case the heaviest single wheel fourth axle load. The fatigue load was determined based on the single wheel load equivalent of the dual wheel ESAL load. This was developed in accordance with the geometric relations used to convert dual tire loads into single tire loads for the analysis of concrete pavement sections (Huang, 2004), and since the relations are all geometric it was assumed to be applicable to loads on non-concrete pavement structures. A tire pressure of 600-kPa was assumed in determining this area.

The loads are applied to the model through a pressure application over the contact area. Abaqus allows a total force to be distributed across the selected area, so this technique was used to apply a ramped, static, general load to the panel model. This is demonstrated in Figure 4-14 on a sample structural base. The load area is designated on the panel model by partitioning the transparent layer so that there is a volume with a designated upper surface area that matches the tire contact area. Gravitational loads were also included in the analysis.

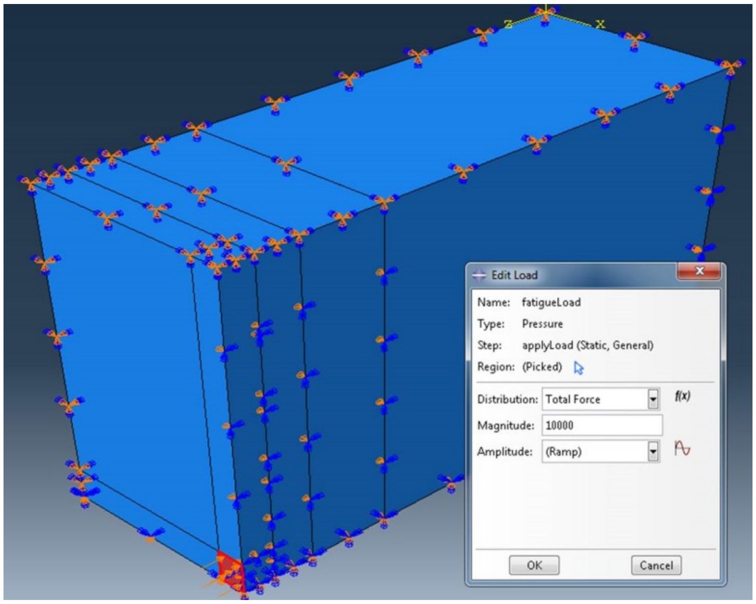

Name: fatigueLoad
Type: Pressure
Step: applyLoad (Static, General)
Region: (Picked)
Distribution: Total Force
Magnitude: 10000
Amplitude: (Ramp)

Figure 4-14: FE model load application for fatigue load case

In order to properly assess the performance of the solar road panel it needed to be loaded in four distinct locations as shown in Figure 4-15: centre, transverse edge, longitudinal edge, and corner. These conditions cover the extremes of typical panel stresses from tire loading, with the total load being applied to either one, two, or four panels.

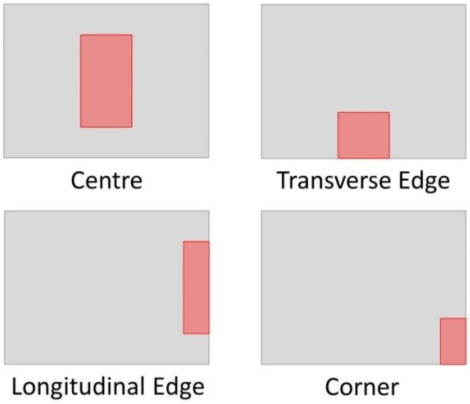

Figure 4-15: FE tire load application locations, direction of travel up the page

4.2.2.2 Structural Bases

The structural bases that were selected for analyzing the panel performance on are the typical pavement structure guidelines for minor arterial roads with 1000 annual average daily truck traffic. This level of traffic was chosen because it provides a reasonable example of where the panels would be installed for initial trials, in lower volume and loading applications. The purpose of the FE study is also to determine comparative performance of solar road panels on a variety of structural bases, and medium volume road bases will provide a starting point for this comparison.

The structures for concrete (PCC) and asphalt (HMA) roads are taken directly from the StreetPave report (ARA, 2011), which outlines the standards used for pavement infrastructure in Ontario. Models for granular and subgrade structural bases are based on the HMA road design with the additional layers removed as required. For this the HMA base was chosen over the PCC base because of the increased equivalent thickness of the asphalt base, which implies greater strength. The high strength subgrade was chosen as the structural subgrade for the models. The layer thicknesses for the four structural bases are outlined below in Table 4-4.

Table 4-4: FE structural base layer thicknesses (ARA, 2011)

Material	**Base Structure [mm]**			
	PCC	**HMA**	**Granular**	**Subgrade**
PCC	200	-	-	-
HMA	-	120	-	-
Granular A	200	150	150	-
Granular B	-	300	300	-
Subgrade	Infinite	Infinite	Infinite	Infinite

The material properties for each of these material layers are defined below in Table 4-5. These values are largely derived from Ontario's default parameters for the AASHTOWare pavement design tool (MTO, 2012), the Ontario provincial standards for granular materials (OPSS, 2003), the StreetPave report (ARA, 2011), the Canadian Pavement Asset Design and Management Guide (TAC, 2012), and the AASHTO Guide for Design of Pavement Structures (AASHTO, 1993). These documents represent the standard design practice for Ontario pavement structures, so no variability of these values is considered in the study.

Table 4-5: FE structural base material properties

Material	Elastic/Resilient Modulus [MPa]	Poisson's Ratio	Specific Density [kg/m^3]
PCC	29,600	0.20	2,320
HMA	2,758	0.35	2,460
Granular A	250	0.35	2,400
Granular B	200	0.35	2,000
Subgrade	50	0.3	1,750

4.2.2.3 Modeling Techniques and Validation

Due to the size of each layer within the study it was possible to accurately model them as 3-dimensonal solid extrusions with homogenous material properties. Contact properties between the layers, and between the panel model and the pavement structure, were defined the same way as within the panel model; normal contact with a linear over-closure penalty and with automatic stabilization contact control. This was done because of, once again, the large differences in material properties between the layers of the models. In some cases the step size was decreased to improve the probability of a converging solution, as per the literature recommendation (Mak, 2012).

Due to the potential size of the model, symmetry effects were used as frequently as possible. Each of the load configurations allows for symmetry about the x- and y-axes within the structural base, though loading on the edge or corner of sees symmetry not applied to some or all of the edges of the panel model. The boundary conditions applied to the bottom and far sides of the modeled structure are encastre conditions, as a model of sufficient size allows the base to deform adequately within the scope of the model and not interact with the boundaries. A summary of the conditions applied for each load case can be found in Table 4-6.

In order to validate these FE models, an extensive parametric study was completed to determine the effects of mesh sizing, base model length and width, and subgrade depth. The range across which the parameters are being varied is identified in Table 4-7, with the default variables identified for each condition.

Table 4-6: FE boundary conditions per load application model

Load Application	Panel Fraction Modeled	Tire Load Applied in Model	Panel Boundary Conditions	Pavement Boundary Conditions
Centre	1/4	1/4	Near X: Symmetry Near Y: Symmetry Far X & Y: None	Near X: Symmetry Far X: Symmetry Near Y: Encastre Far Y: Encastre Base: Encastre
Transverse Edge	1/2		Near X: Symmetry Near Y: None Far X & Y: None	
Longitudinal Edge	½		Near X: None Near Y: Symmetry Far X & Y: None	
Corner	1		Near X: None Near Y: None Far X & Y: None	

Table 4-7: FE load case model validation parameters

Parameter	Default Value	Analysis Range
Subgrade Depth [m]	1.5	0.5, 1.0, 1.5, 2.0, 2.5
Base Length [m]	3.0	1.5, 2.0, 3.0, 4.0, 5.0
Base Width [m]	1.5	
HMA Average Mesh Size [m]	0.025	0.10, 0.075, 0.05, 0.025, 0.01
PCC Average Mesh Size [m]	0.025	
Granular A Average Mesh Size [m]	0.025	
Granular B Average Mesh Size [m]	0.025	
Subgrade Average Mesh Size [m]	0.050	0.10, 0.075, 0.05, 0.025

The mesh strategy in the structural bases is different from the panel model in that biased seeding techniques are being used to optimize the analysis. Since the load application is concentrated over a small portion of the overall model, a higher density of nodes is required at the load area to accurately model stresses, strains, and displacements than in the far corners of the encastred boundaries. This is accomplished by determining the number of nodes along a given edge using the average mesh size and seeding the individual edges of the model with that number of elements but with a single bias towards the loaded corner and a bias ratio of five, the Abaqus default. This seeding process is used for all structural base edges in the x-y plane and the z-direction edges for the subgrade, but double bias seeding is applied for all other z-direction edges to ensure that both upper and lower face contacts are modeled accurately. This is demonstrated for the default subgrade layer in Figure 4-16 below.

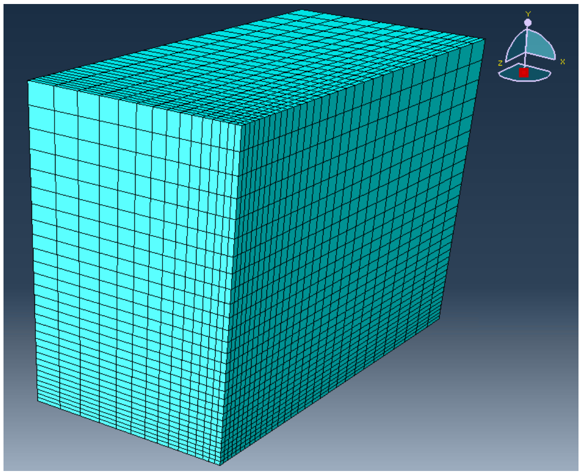

Figure 4-16: FE subgrade model with complete single bias meshing

The parameters being optimized through the validation process are the maximum stress, strain, and translation within the panel model. For the sake of validation, the panel model is simplified to a 1-m by 1-m by 25.4-mm layer of tempered glass. The goal of the validation process is to achieve a level of 95% accuracy within the model for each of these properties based on the parameters varied from Table 4-7. The validation was completed in a cascading fashion, starting with the subgrade depth and proceeding down the list identified in the table. This was done so that a value could be locked in for each property to converge to the most accurate solution.

4.2.3 Static and Fatigue Property Analysis

The values measured to assess the static and fatigue performance of the panels were the maximum stress of the transparent, base, and structural base components; the maximum strains in the base and structural base; and the maximum deflection of the structural base. These values were compared between the different load cases and structured bases to determine which structural base conditions the panels are most suited to be installed on.

4.2.3.1 Fatigue Analysis

The fatigue analysis was completed differently for the glass, fiberglass, and structural base layers as they fail through cyclic loading by different mechanisms, however the objective is to determine the number of ESALs that the panel can withstand on each structural base before failure of any component.

Glass specimens fail through fracture methods due to the brittle nature of the material. The method by which this occurs is well documented in literature (Alsop & Saunders, 1999) making this analysis method straight forward. The assumption is that there are micro-cracks in the surface of the material 0.7-μm in length (Budynas & Nisbett, 2008). As the panel is cyclically loaded the crack slowly propagates through the material. This propagation occurs at a constant rate while load is being applied to glass, so sensitivity will also be analyzed for the speed of traffic over the panel. Other factors including the notch parameters have been identified in literature (Budynas & Nisbett, 2008) and will vary as the crack length increases, making this an iterative solution. In order for fatigue failure to occur at all, the developed tensile strains must exceed the 69-MPa compressive edge stress developed through the tempering process.

Fiberglass laminate fails through traditional fatigue theory methods, as S-N curves have been developed that accurately predict the performance of various laminates to cyclic loading. In this case the curve has been developed as shown below, in Figure 4-17, for short glass fiber reinforced matrices; which is a best available estimate of the fatigue performance of the GPO-3 used in the prototype panel. Determining the number of available load cycles is based on the fatigue load induced stress to ultimate stress ratio of the material and then applying the given formula.

Concrete pavements fail through a number of mechanisms as outlined in the equations shown in Figure 4-18; where N_f is the maximum number of stress cycles, σ is the cyclical stress applied to the concrete, and S_c is the compressive strength of the concrete. Similarly to the equations for GPO-3, an endurance limit exists at a maximum stress of 0.45 times the compressive strength of the concrete at which point unlimited fatigue cycles may be applied. The compressive strength assumed for these calculations will be 32-MPa, a traditional design value for Ontario pavements (ARA, 2011). These conditions are also sensitive to the joint placement as typically higher stresses are realized at the edges and corners of concrete slabs.

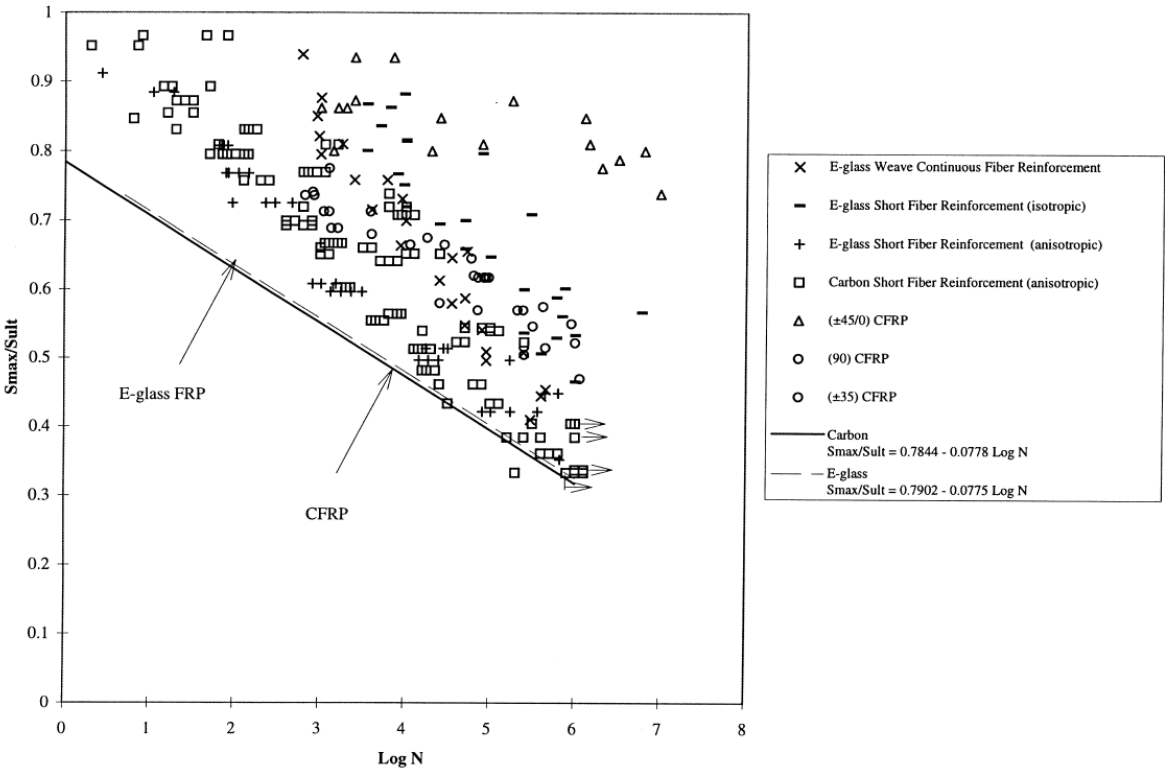

Figure 4-17: S-N curve for cyclic loading performance of short fiber reinforced matrices (Demers, 1998)

$$\text{For } \frac{\sigma}{S_c} \geq 0.55: \quad \log N_f = 11.737 - 12.077\left(\frac{\sigma}{S_c}\right)$$

$$\text{For } 0.45 < \frac{\sigma}{S_c} < 0.55: \quad N_f = \left(\frac{4.2577}{\sigma/S_c - 0.4325}\right)^{3.268}$$

$$\text{For } \frac{\sigma}{S_c} \leq 0.45: \quad N_f = \text{unlimited}$$

Figure 4-18: Concrete pavement fatigue life equations (Huang, 2004)

Asphalt pavements fail through two primary mechanisms; fatigue cracking and rutting. For fatigue cracking, the relation between design life and horizontal strain developed at the bottom of the asphalt layer is shown below in Figure 4-19; where N_f is the allowable number of load cycles, ε_t is the horizontal strain at the bottom of the asphalt layer, and E_1 is the elastic modulus of the asphalt material. The elastic modulus value used in this empirical equation must be input in imperial units, so a value of 400,000-psi was used.

$$N_f = 0.0796(\varepsilon_t)^{-3.291}(E_1)^{-0.854}$$

Figure 4-19: Asphalt pavement fatigue life equation (Huang, 2004)

Rutting, a failure that occurs in both asphalt and granular structures, is a function of the vertical compressive strain that is developed at the bottom of the lowest granular layer. The relation for this is shown in Figure 4-20; where N_f is the allowable number of load cycles, ε_t is the vertical compressive strain at the bottom of the granular layers, and E_1 is the elastic modulus of the asphalt material.

$$N_f = 0.0685(\varepsilon_t)^{-5.671}(E_1)^{-2.363}$$

Figure 4-20: Asphalt and granular rutting life equation (Huang, 2004)

4.3 Environmental Testing

The purpose of this portion of the testing is to determine the impact that freeze-thaw cycling and scaling have on the structural, optical, and textural performance of materials that would be used in the transparent layer of a solar road panel. The goal being to identify the initial changes to the properties of these materials to identify if further investigations are required.

4.3.1 Material Selection

In order to keep the environmental testing consistent with the solar road panel design process; glass, acrylic, and polycarbonate were selected as the materials for environmental testing. The materials were all ordered to a specific thickness and then cut to the size required for the individual tests. All of the samples were prepared with flat, non-textured surfaces so that the effects being analyzed are purely from a material perspective and do not include texture variation effects.

4.3.2 Sample Conditioning and Testing Standards

The scaling treatment and testing performed on the transparent materials are as identified in Table 4-8. Variations to the standards were made, as outlined in the following section, to adapt the tests to the materials being tested and the facilities available at CPATT and UW.

4.3.3 Scaling Resistance

The scaling resistance technique outlined in ASTM C672 (ASTM, 2012b) was designed for use on concrete cylinders, making it an ideal candidate for pavement surface conditioning. The standard calls for the application of a salt brine to the surface of the samples with freeze-thaw cycling being applied.

Samples are to be tested for visible effects of scaling on a subjective scale after 0, 5, 10, 15, 25, and 50 cycles. After each fifth cycle the samples are to be rinsed and the salt brine reapplied. The output of the scaling resistance is the subjective measurement of how much the surface has scaled, where a '0' implies no scaling and '5' implies that the surface is heavily scaled.

Table 4-8: Standard procedures for environmental testing

Purpose	Standard	Description	Sample Size
Conditioning	ASTM C672	Scaling resistance evaluation of concrete surfaces exposed to deicing chemicals	N/A
Testing	ASTM D790	Three-point bending of unreinforced and reinforced polymers	114-mm x 25.4-mm x 6-mm or 6.35-mm
Testing	ASTM E303	Frictional evaluation using the British Pendulum Tester	89-mm x 152-mm x 6-mm or 6.35-mm
Testing	ASTM E1175	Determining solar or photopic properties of materials using an integrating sphere	50.8-mm x 50.8-mm x 6-mm or 6.35-mm

4.3.3.1 Standard Modifications

There were two challenges with adapting this standard to the polymer and glass sample being used in the environmental testing; salt brine composition and the method by which the salt brine is applied.

For the purposes of this testing it is important to determine if salt brine application has an impact on these materials that should be further investigated and optimized. For this purpose, the four-percent by weight solution of anhydrous calcium chloride was seen as an inadequate scaling solution. In order to determine whether or not the scaling has an impact on the samples, it was determined that a 25-percent by weight solution of sodium chloride should be used. This is a common salt that is used as a chemical deicer, making it an ideal candidate, and at this concentration is near the maximum that can be obtained at room temperature.

This does add another difference between this and traditional scaling resistance tests. A 25-percent by weight solution of sodium chloride would not actually freeze at the temperatures we could cycled the samples to, though the samples still reach a temperature of -16°C as verified by an infrared thermometer. This should have little impact on the study as the typical purpose for freezing the brine solution is to propagate the ice into cracks in the material. Due to the smoothness of our samples there should be no significant cracks for ice to propagate into, thus making the higher solution strength a greater asset in determining corrosion potential and effects.

The method of application for the salt brine also proved challenging due to the nature of the specimens being tested. The standard calls for a constant solution depth on the surface of the specimens to be maintained, however the number of specimens and their irregular sizes being tested made this challenging. To accommodate this, it was determined that the specimens could be submerged or suspended in containers of the brine solution. This still maintains an adequate level of brine being applied to a specific surface of the specimen, and each specimen could be identified for weather it was submerged or suspended. The submerged samples were typically glass while the polymers were suspended due to the differences in density of the materials.

4.3.3.2 Conditioning Procedure

A rolling cart with a custom built rack was used to hold the samples during the scaling resistance process, as shown in Figure 4-21. The samples being scaled were kept in the raised bins while the regular samples were kept flat on the floor of the cart. The floor of the cart was covered in wax paper to protect the specimens from contact with the cart.

Figure 4-21: CPATT freeze-thaw cart arrangement

This cart was then rolled in and out of the CPATT Lab's walk-in freezer at intervals allowing at least two hours of time for the samples to freeze and two hours of time for the samples to thaw, as these were the intervals determined during checks in the first cycling to ensure that the samples met their required temperatures as verified by an infrared thermometer.

As this cart was also used for freeze-thaw cycling of pervious concrete samples, the tracking sheet used to count the testing cycles performed on those samples was modified for use with these optical test specimens.

4.3.4 Three-Point Flexural Testing

The three-point bending technique outlined in ASTM D790 (ASTM, 2010) was designed for the flexural analysis of polymer specimens. Due to the nature of this environmental testing, the same conditions were used for the glass samples to maintain a level of uniformity between the tests.

4.3.4.1 Testing Apparatus

Due to the small size and low estimated failure load of the components, this testing could not be performed on equipment within the Civil Engineering Structures Lab. For this material testing it was determined that the best option was to use equipment within the Materials 2 Laboratory, operated by Mechanical and Mechatronics Engineering. The load setup used is shown below in Figure 4-22.

Figure 4-22: Materials 2 Laboratory 500-kg Instron

In order to minimize the cost of the apparatus required for this test, it was decided that an existing base would be used for the testing which had the capacity for additional brackets to be fitted to it to meet the ASTM D790 specifications. The base, which is used for similar flexural testing, is owned by Dr. Marianna Pollak within Civil and Environmental Engineering and is shown below in Figure 4-23.

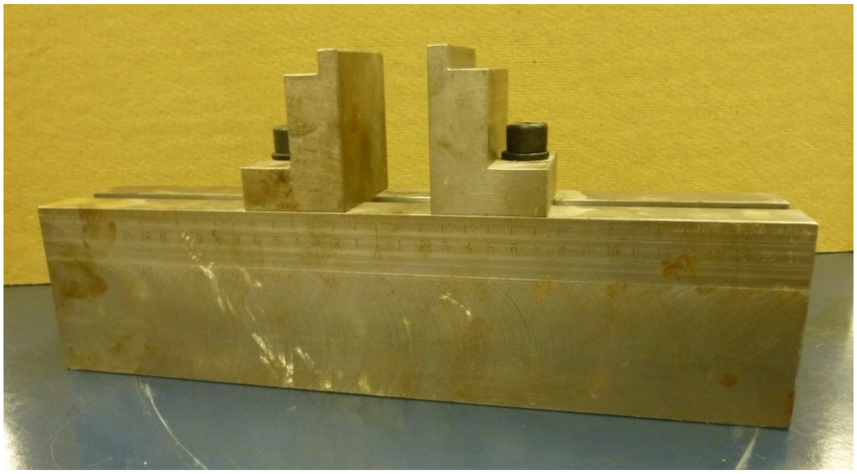

Figure 4-23: 3-point structural loading base

Three pieces of hardware were then designed to make this base work with the Instron machine from Mechanical Engineering and the ASTM standard we are following; a collar to mount the base to the Instron, the support nose brackets, and the load nose assembly. Figure 4-24 shows the finished components as manufactured by RJB Machining, and touched up as required, while detailed drawings for them can be found in Appendix D.

Figure 4-24: 3-point bending test support noses, base collar, and load nose (left to right)

4.3.4.2 Testing Specimens

The samples were originally cut with the intention of doing testing across a 101.6-mm [4-in] span due to the standard size of materials being available in 6.35-mm [0.25-in] depth. As a result the specimen materials were ordered and the parts were cut to the size outlined in Table 4-8. Some of the materials were only available in a metric sizing, so a 6-mm depth was used for these materials, as this was the closest available metric size. The average dimensions and standard deviation of measurements are outlined below in Table 4-9.

Table 4-9: 3-point bending specimen dimensions

	Length		**Width**		**Height**	
Material	Average [mm]	Standard Deviation	Average [mm]	Standard Deviation	Average [mm]	Standard Deviation
Acrylic	113.8	0.5055	24.83	0.5613	5.687	0.1651
Glass	114.3	1.400	26.25	1.041	5.550	0.03302
Polycarbonate	113.7	0.3353	24.93	0.5004	6.233	0.03810

In order to accommodate for the thinner materials, it was determined that a smaller span than 101.6-mm [4-in] should be used in testing. The span based on the actual material thicknesses was determined to be 95.25-mm [3.75-in] as this would allow for all of the specimens to be tested within the bounds of sample measurement for the ASTM D790 standard.

4.3.4.3 Testing Procedure

The testing rig is shown in Figure 4-25, with the support nose spacing set at 92-mm [3.625-in], a value within the valid range of testing as per ASTM D790. Testing was run at a displacement rate of 2.71-mm/min [0.1067-in/min] in accordance with the ASTM standard and the dimensions of these specimens.

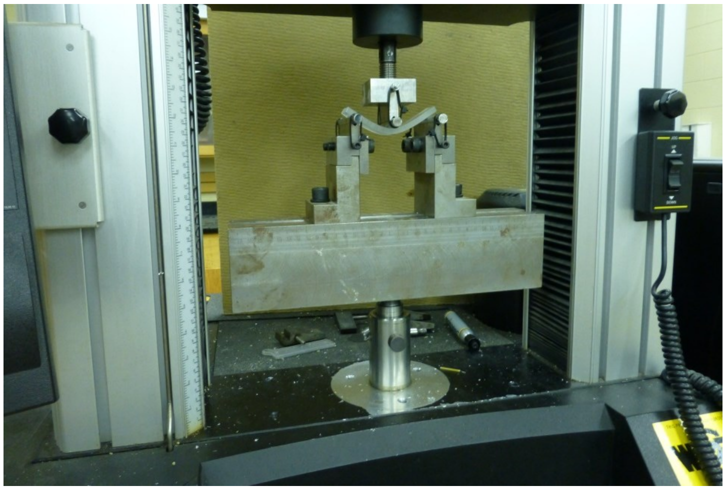

Figure 4-25: 3-point bending test apparatus

4.3.5 Friction Testing

The friction testing, as per ASTM E303 (ASTM, 2012b), was performed in the CPATT Lab using the existing calibrated British Pendulum. The standard was followed without modification, and based on practice it was determined that six sprays of water from a spray bottle were required to fully saturate the surface of the specimens with water, as shown in Figure 4-26.

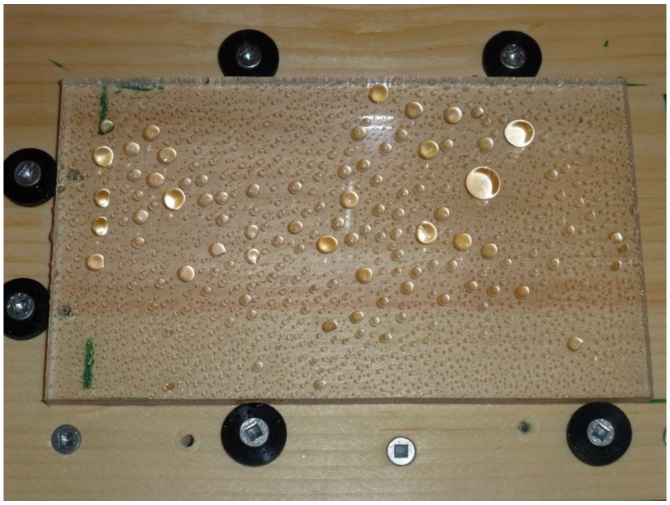

Figure 4-26: Water-saturated friction test specimen

To accommodate the test specimens, a platform with adjustable bumpers, as shown installed in Figure 4-27, was designed to be installed around the existing formwork for the pendulum. This platform also allowed for compatibility between ongoing friction testing in the lab, so that the pendulum did not have to be constantly readjusted between testing concrete cylinders for other research and the optical materials for this analysis.

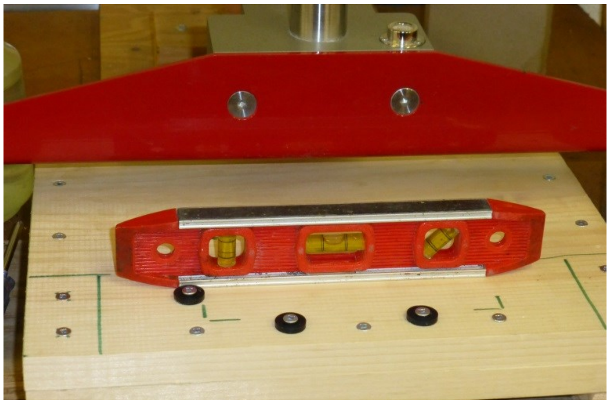

Figure 4-27: Friction testing platform

To ensure repeatability of the tests, one new British rubber slider was acquired and used for all of this testing. This was of high importance as rubber sliders kept with the device are often used for concrete or asphalt testing in between, which would supply much more damage and impact the results of this testing. Calibration of the device in terms of energy loss and slider contact area were completed before each set of freeze thaw cycle testing and checked periodically through the testing runs.

The data obtained from this testing is in terms of British Pendulum Numbers, as the values obtained were too low for comparison in terms of Skid Number; a value more commonly used in pavement evaluation.

4.3.6 Optical Testing

The optical testing, as outlined by ASTM E408-13 (ASTM, 2013), E903-12 (ASTM, 2012a), and E1175-87 (ASTM, 2009), is performed to determine the transmissivity, reflectivity, and absorptivity of materials. The apparatus used for this testing is the Varian Cary 5000 UV/VIS/NIR spectrophotometer, as shown in Figure 4-28, operated by the Solar Thermal Research Lab at the University of Waterloo.

Figure 4-28: Varian Cary 5000 UV/VIS/NIR Spectrophotometer

Tests were conducted at 5-nm intervals from 250-nm up to 1200-nm. The 1200-nm ceiling for the tests was chosen to ensure that the entire spectrum of absorption for solar PV cells was covered (Luque & Hegedus, 2003) and to reduce time from running the test to 2500-nm as was available; the longwave radiation testing, testing over 800-nm, is highly time intensive due to the sensor used for data collection.

For the testing, 50.8-mm [2-in] square samples were used to ensure that material was covering the entire opening for light transmission. The samples were cleaned with a glass cleaner prior to testing to remove any residue that collected during the scaling process. For transmission testing the samples were installed in front of the integrating sphere of the Cary 5000, as shown in Figure 4-29, so that electromagnetic radiation could be passed through the sample and into the integrating sphere. For the reflection testing, the samples were installed behind the integrating sphere as shown in Figure 4-29.

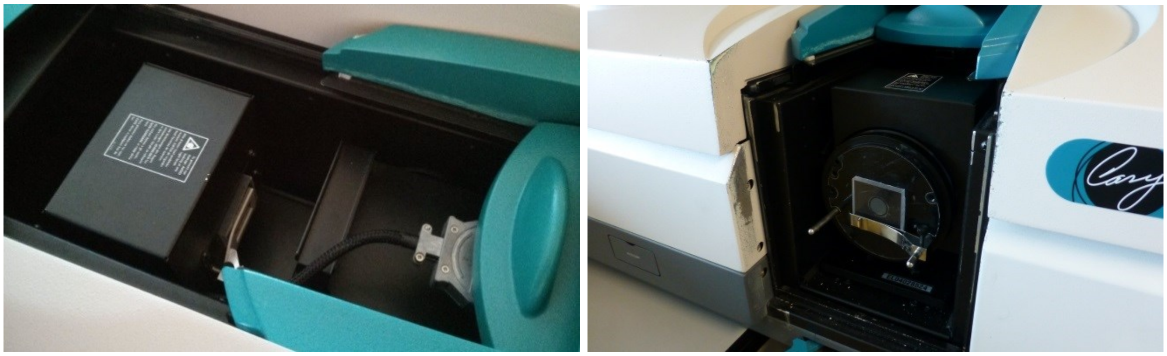

Figure 4-29: Sample positioning for transmissivity and reflectivity testing (left to right)

Chapter 5

Structural Prototype Testing and Analysis

This chapter outlines the results from the structural testing and finite element analysis that was described in the methodology.

5.1 Structural Testing Results

Four data sets were collected which represented three loading locations (centre, side, and diagonal) and two applied loads (2.22-kN and 4.44-kN). These three load positions and the grid references used to identify locations on the panel during testing are shown in Figure 5-1 and correspond to loads at locations C-3, C-2, and D-2.

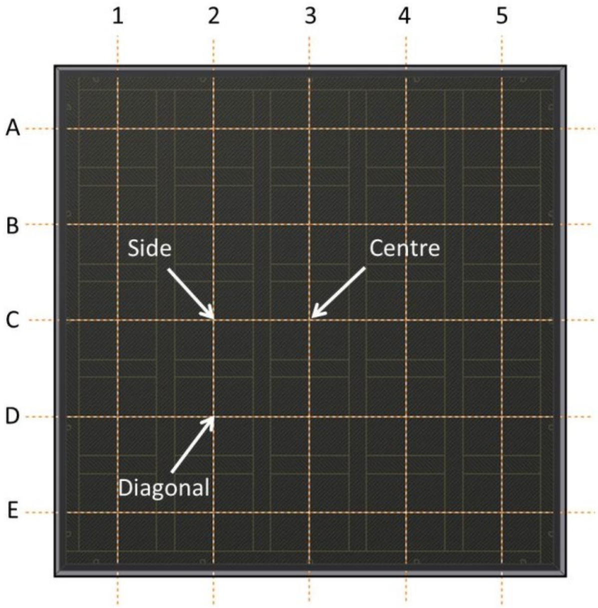

Figure 5-1: Structural testing load positions on transparent layer

Since the panel orientation for testing was upside down, as shown in Figure 4-13, the orientation of all of the strain and deflection response data is with respect to the locations shown in Figure 5-2. This figure still shows the load cases, however since the base layer of the panel is facing upwards in this configuration these labels only represent where the maximum strains and deflections should be noted during the testing.

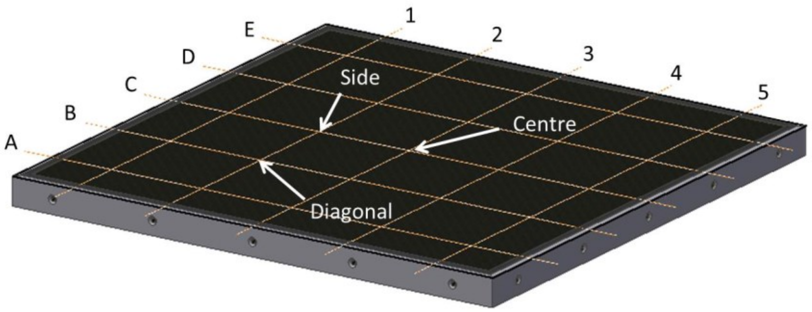

Figure 5-2: Structural testing result orientation

Due to the orientation of the rosettes and LVDTs, as outlined in Figure 4-11, there are no values collected for A-2, A-4, B-1, B-5, D-1, D-5, E-2, or E-4. This is represented in the figures below as having no strain or deflection at these points.

5.1.1 Strain Response

The strain response of the panels was largely as expected. As demonstrated in Figure 5-3 for the 4.44-kN centre load, the glass panel produced the highest strain where the load was applied with the values tapering off towards the edge of the panel.

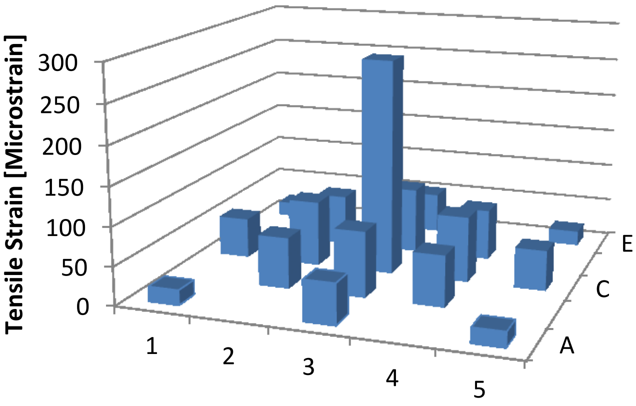

Figure 5-3: 4.44-kN centre load glass strain response

This same phenomenon applied to all four data sets on the glass panel, including the eccentric load placements for the side and diagonal load cases. This is demonstrated below in Figure 5-4 for the 2.22-kN diagonal load test.

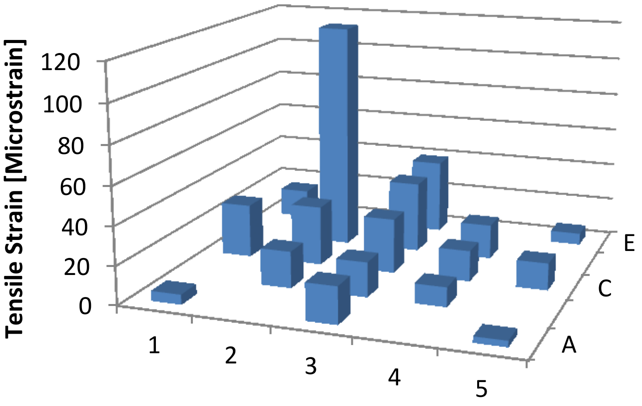

Figure 5-4: 2.22-kN diagonal load glass strain response

Also notable from Figure 5-4 is that the measured strain response is fairly symmetrical about the diagonal axis from A-5 to E-1. Given that four tests with 2.22-kN loads at B-2, B-4, D-2, and D-4 were amalgamated to make this profile, the symmetry represents a high level of accuracy within the testing regimen and constructed prototype.

In some cases for the strain response of the base layer strains were observed at the edges of the panel that were higher than at the expected peak location. This is shown in Figure 5-5 for the 2.22-kN centre load case. Note that the highest strain would be expected at location C-3, however higher values are found at every point around the edges. This is believed to be a result of boundary effects on the panel, as repeated testing delivered the same results.

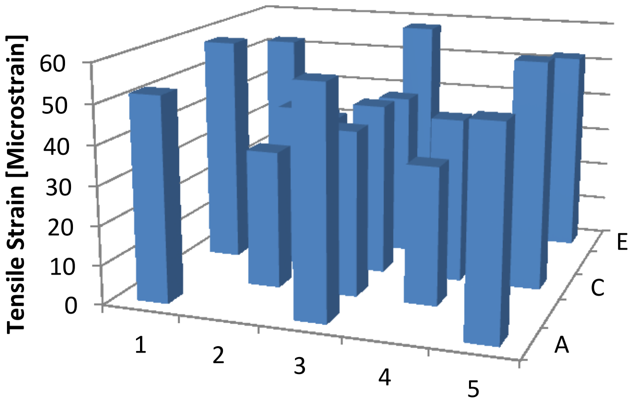

Figure 5-5: 2.22-kN centre load base strain response

5.1.2 Deflection Response

Due to the orientation of the panel and the sensitivity of the transducers being used, deflection measurements were only taken for determining the differences in deflection between two load cases. As a result, this testing was only accomplished for the centre load condition for the deflection difference between 2.22-kN and 4.44-kN.

The results from this testing followed the trends that were expected, as shown in Figure 5-6, where the largest deflection between the 2.22-kN and 4.44-kN loads occurred at the centre of the panel and tapered towards the edges.

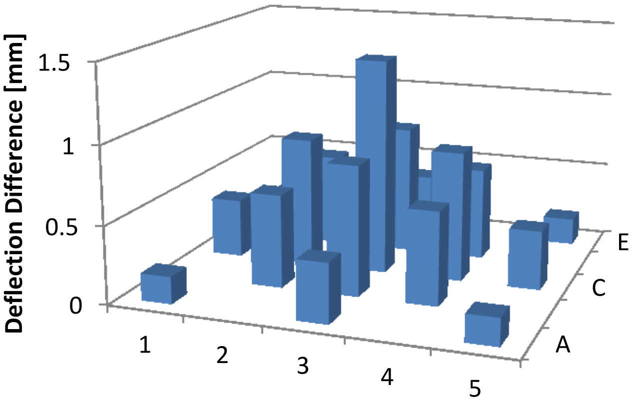

Figure 5-6: Deflection difference from testing between 2.22-kN and 4.44-kN centre loads

However, it is important to note that the deflections measured here are much larger than were expected based on the initial FEA shown in Figure 4-2. In this figure an expected maximum deflection of 0.84-mm is demonstrated for a 4.44-kN centre load, while the test data shows a deflection of 1.4-mm between the 2.22-kN and 4.44-kN load conditions.

Extensive reworking of the laboratory test apparatus occurred in an effort to ensure that the testing was appropriate for measuring the deflection responses. As noted earlier, the objective of the testing is to drive simulations that can predict the in-field strain and deflection responses of this panel to vehicle loading. The displacement transducers were recalibrated to ensure their accuracy using thin plates of known thicknesses. The frame members were also removed, as shown in __, as it was believed that the foam inserts and edge seal may be affecting the response being measured.

When the tests were rerun under the new conditions it was found that the deflections measured were of a similar magnitude. Since there is a discrepancy between these measurements and the original predicted values, the model development will focus on the measured strain values and the deflection will be analysed with respect to these models.

5.2 Prototype FE Model Development

5.2.1 Mesh Development

The summary of the mesh development can be found below in Table 5-1. The smaller meshes for the transparent and base layers are as expected since the focus of the mesh development was to accurately model the stress, strain, and deflection response of the these layers. The number of integration layers remained small for all of the layers because elastic behavior was assumed for the entire model, removing the sensitivity of this parameter.

Table 5-1: Prototype panel mesh development results

	Model Parameter	
Layer	**Integration Layers**	**Mesh Size [mm]**
Transparent Layer	3	6.35
Optical Layer	3	25.4
Base Layer	3	6.35

5.2.2 Structural Test Simulation

Each of the structural tests performed were simulated using the mesh conditions outlined above. Figure 5-7 and Figure 5-8, the glass and base layer strain contours from the 2.2-kN diagonal load simulation with average material properties, demonstrate the typical results from these simulations. In the transparent layer the strain peaks where the load is applied with the strain tapering towards the edges of the panel. The strain contours in the base layer peak at the same location, but the actual maximum values are closer to the optical layer ribs that transfer the load between the layers.

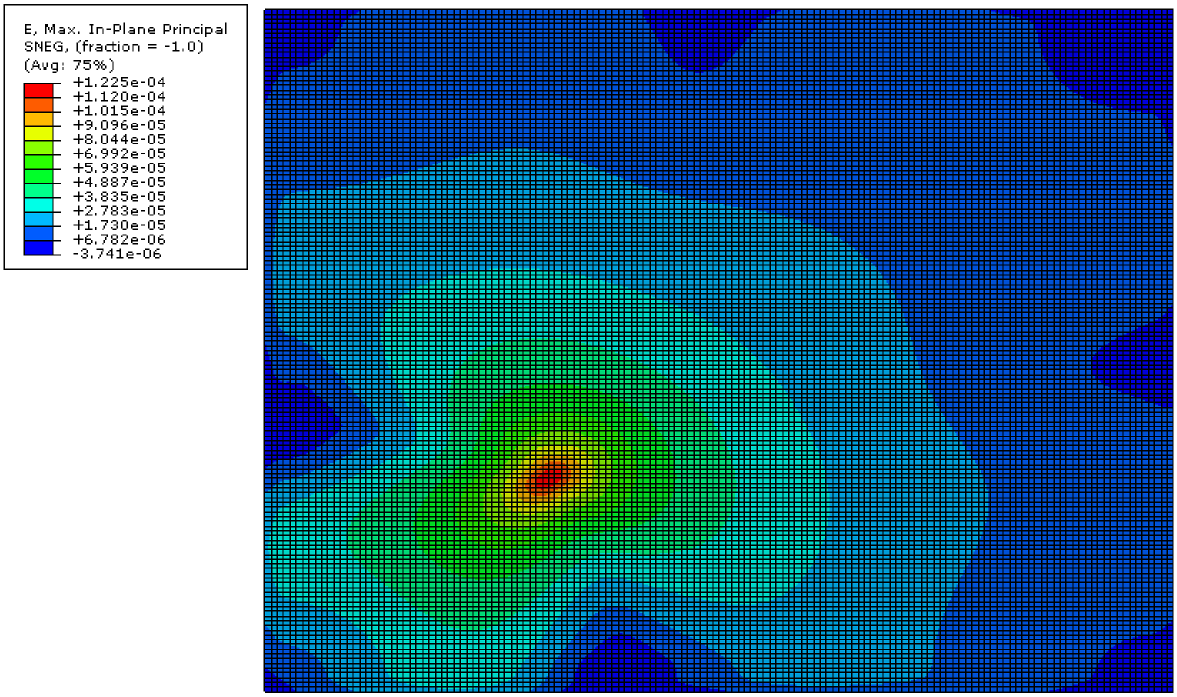

Figure 5-7: 2.22-kN diagonal load simulation average material property glass strain contours

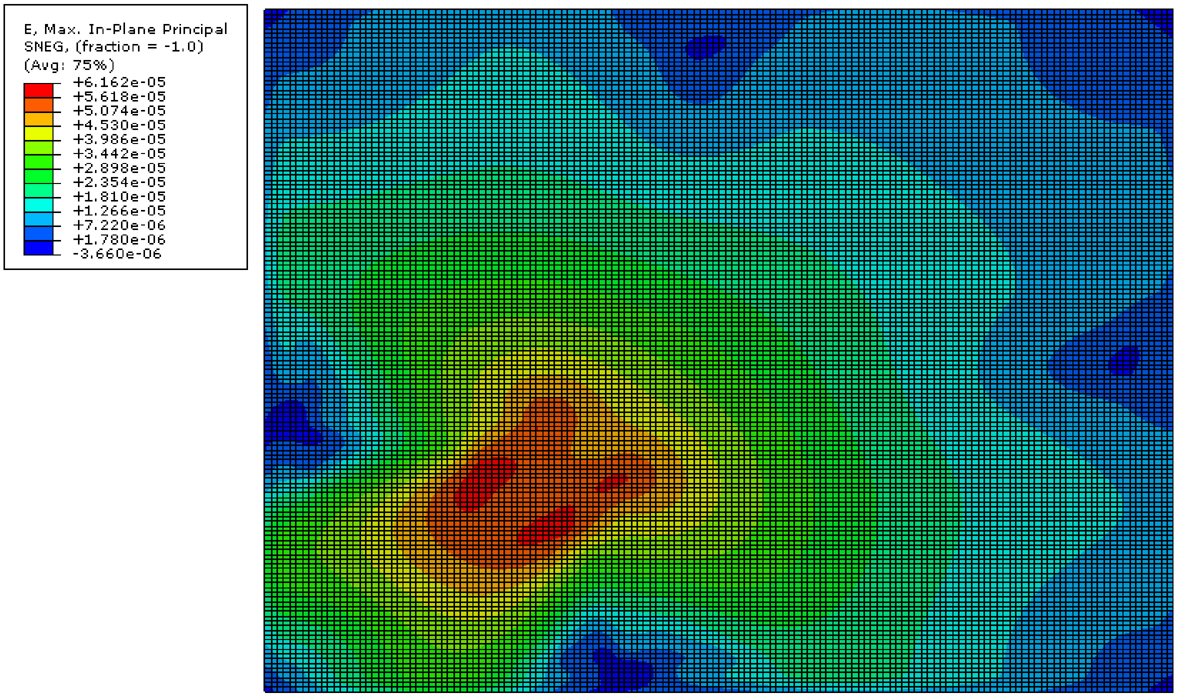

Figure 5-8: 2.22-kN diagonal load simulation average material property base strain contours

5.2.3 Model Validation

To compare the strain data between the structural testing and the simulations the absolute difference between the two models was calculated. This result for the 2.22-kN diagonal load with average material properties is shown in Figure 5-9. Note that the differences in strain are larger on the boundaries than they are on the inside of the model; this is likely due to difficulty in accurate boundary condition simulation.

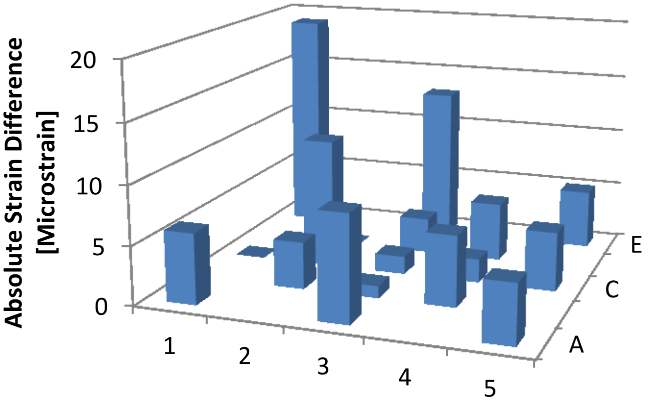

Figure 5-9: 2.22-kN diagonal load absolute strain difference for the average material property model

The results shown in Figure 5-9 were then averaged to provide an average absolute error metric which was used to determine the optimal material property configuration. The results of this are shown in Figure 5-10 and demonstrate that, across the entire model, the rigid material property configuration produces the lowest average absolute strain error.

This figure, however, does not take into account that the boundaries of the model have larger errors due to the boundary conditions. To eliminate these known errors from the decision making, the boundaries were removed from the data set by simple exclusion; the new data set did not include values from grid locations with *A*-, *E*-, -*1*, or -*5* labels.

New average absolute strain errors were determined as shown in Figure 5-11. This figure shows that while the average properties are the best performer for the diagonal load case, that the overall best material property configuration for matching the structural testing is still the rigid configuration.

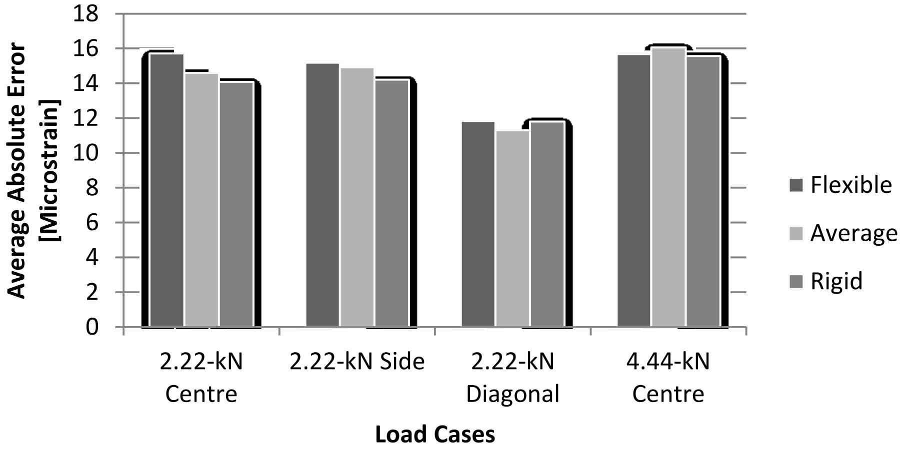

Figure 5-10: Average absolute strain error between testing and simulations

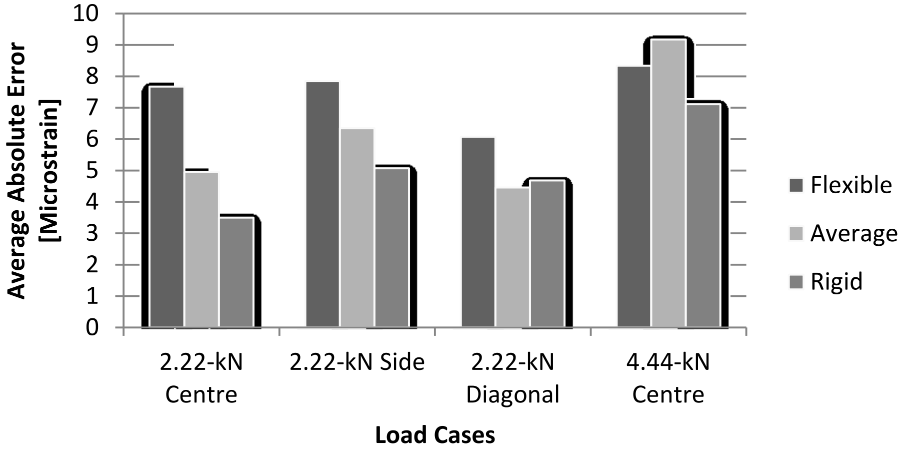

Figure 5-11: Average absolute strain error between testing and simulations for non-boundary locations

5.2.4 Strain Modelling Deficiencies

As has already been noted, the model developed does a poor job of simulating the strains found near the boundaries during the structural testing. From the perspective of solar road panel applications this is not a major concern because the type of cantilevered support for the panel during testing will not be found in the real world. The boundary conditions applied by anchoring the panels may prove to be difficult, but refining meshes around these points can mitigate errors.

The other deficiency of the model that has been developed is its ability to accurately predict the maximum glass strain under the 4.44-kN centred load test. As noted in Figure 5-12, the model under predicts the maximum strain seen in the transparent layer by 41-microstrain. The majority of this difference is likely due to a mechanical defect in the glass specimen, as unsupported glass should not strain that much under similar load and boundary conditions.

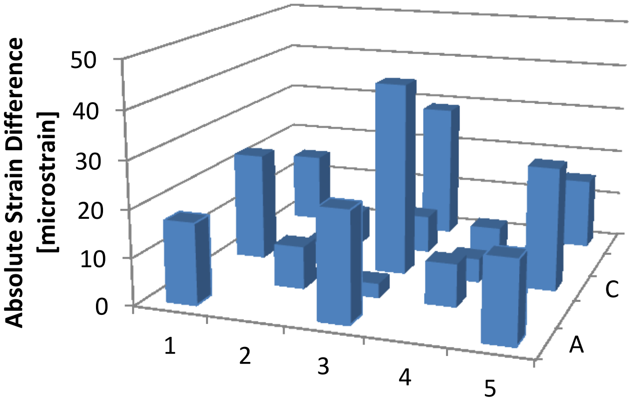

Figure 5-12: 4.44-kN centre load absolute strain difference in the transparent layer for the rigid material property model

5.2.5 Deflection Modelling

As identified in 5.1.2, the deflection results obtained from the structural testing followed the expected trend of the initial FEA but were of a much larger magnitude. The final modeled deflections, based on the validated strain models, are shown in Figure 5-13 and demonstrate that a maximum deflection difference of 0.28-mm is predicted between the 2.22-kN and 4.44-kN centre load tests.

These values compare to the values obtained from testing as shown in

Table 5-2. This information shows that the values measured are all consistently larger than the values that were predicted. In this case there are two groupings of values that are off by similar margins, with C-3, D-3, and D-2 in one group between 300% and 400% and E-3 and E-1 in the other around 600% to 650%. This is similar to the results found from the strain model validation as E-3 and E-1 are both boundary locations and their test values differ from the model by a larger margin than the other central nodes.

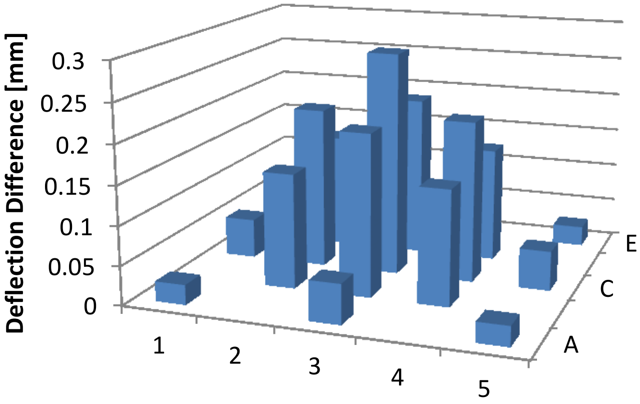

Figure 5-13: Deflection difference from modelling between 2.22-kN and 4.44-kN centre loads

Table 5-2: Deflection result comparison

Transducer Location	C-3	D-3	E-3	D-2	E-1
Test Results [mm]	1.39	0.84	0.38	0.60	0.17
Model Results [mm]	0.29	0.21	0.05	0.15	0.03
% Difference	387%	306%	655%	309%	593%

The results show that there is a clear difference between the deflections that are being measured and those that are being predicted, though the similarity of the deflection profile between the measured and predicted results lends confidence that the modelling procedures accurately depicting the performance of the panel in the laboratory testing conditions. Further study should focus on the deflection performance of these panels, particularly for in-situ applications.

5.3 Pavement Load Case Simulation

5.3.1 Model Development

The summary results of the model development can be found below in Table 5-3 while the detailed results can be found in Appendix E. The results of the validation are as expected, where the layers in closer contact to the panel model require higher resolutions to determine the panel's reactions. Also, larger base areas were required for the higher modulus materials, which is logical as they have properties that naturally spread loads out over a larger area.

Table 5-3: Pavement load case model development results

	Base Structure			
Parameter	**PCC**	**HMA**	**Granular**	**Subgrade**
Subgrade Depth [m]	0.5	1.0	1.0	1.5
Base Length [m]	4.0	3.0	2.0	1.5
Base Width [m]	4.0	3.0	2.0	1.5
HMA Average Mesh Size [m]	-	0.025	-	-
PCC Average Mesh Size [m]	0.025	-	-	-
Granular A Average Mesh Size [m]	0.050	0.050	0.025	-
Granular B Average Mesh Size [m]	-	0.050	0.050	-
Subgrade Average Mesh Size [m]	0.100	0.100	0.100	0.100

5.3.2 Static and Fatigue Load Simulation Results

5.3.2.1 Transparent Layer Stress

The first benchmark for the performance of the panel model in the various conditions is the maximum stress produced in the transparent layer. Being the layer directly loaded from vehicles, it sees the highest stresses within the panel and pavement model. Figure 5-14 demonstrates these values for all of the static load tests. Recall, from Table 3-2, that the compressive stress limit for tempered glass is 5-GPa and that the tensile stress limit is 1-GPa (Alsop & Saunders, 1999).

The most important detail to note from Figure 5-14 is that all of the stresses found within the transparent layer are far below the tensile and compressive yield strengths of glass, meaning that the loads being applied can be safely supported. Also of importance is the ranking order of the pavement structures, with the bases demonstrating the least to most stress, in order, were the PCC, HMA, Granular, and Subgrade bases. This result was expected as the PCC base contains the most rigid materials while each subsequent layer becomes more flexible, providing less resistance to deflection and less load spreading.

The unexpected result from Figure 5-14 is that the centre load case produces the highest stress while the corner case is the lowest for each structural base. The opposite is true in typical pavement applications due to low load transfer between panels limiting the availability of load spreading.

However, Figure 5-15 demonstrates that the maximum stress locations in the solar road panel prototype are more dependent on the optical layer grid pattern.

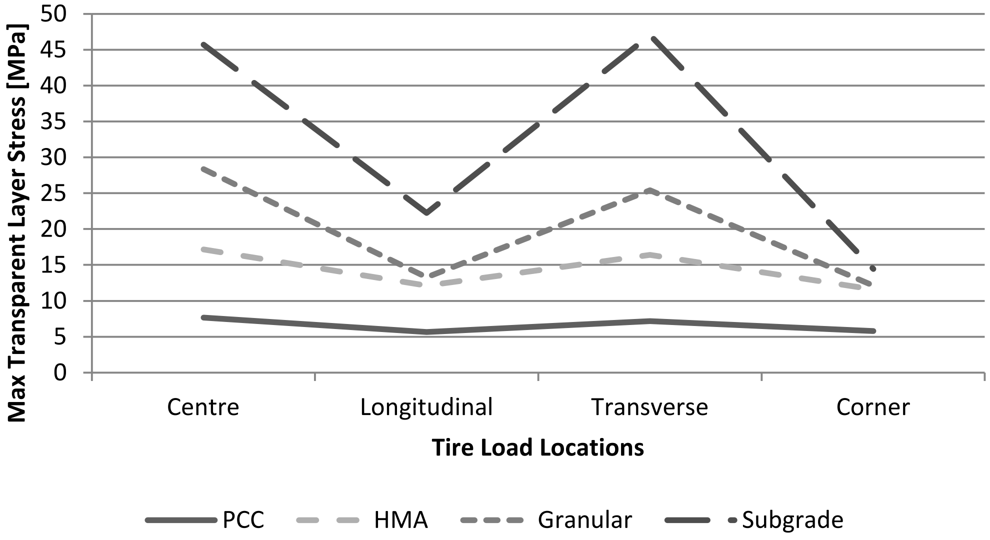

Figure 5-14: Transparent layer stress when subjected to static load

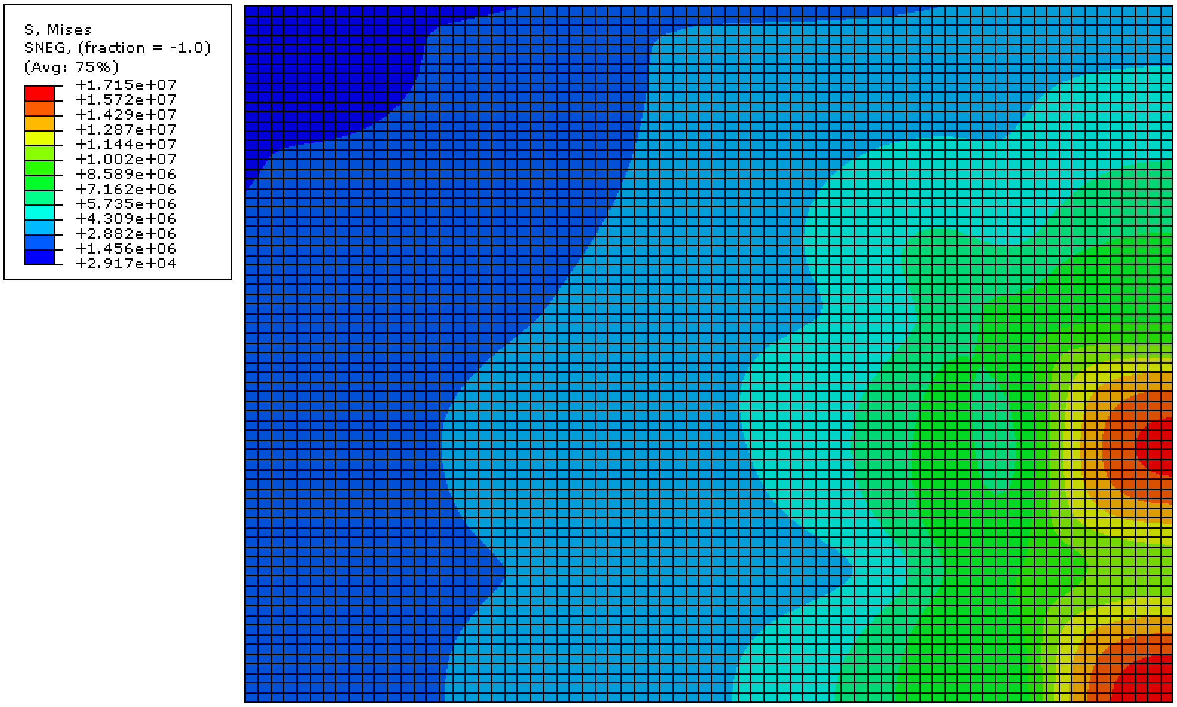

Figure 5-15: Transparent layer stress contours under static, centre load with HMA base

While the maximum stress in Figure 5-15 still occurs in the bottom right corner of the member directly under the applied load, a second maximum stress location appears directly above it and this space corresponds to the adjacent cutout in the optical layer. These higher stresses are a result of the glass being cantilevered over the solar cells at these points, and this proves to be the main structural criteria for the transparent layer as assumed in section 3.1.4. This phenomenon is further illustrated in Figure 5-16 where the maximum stress from the corner load case occurs inset from the corner of the panel due to the location of the first optical layer cutout.

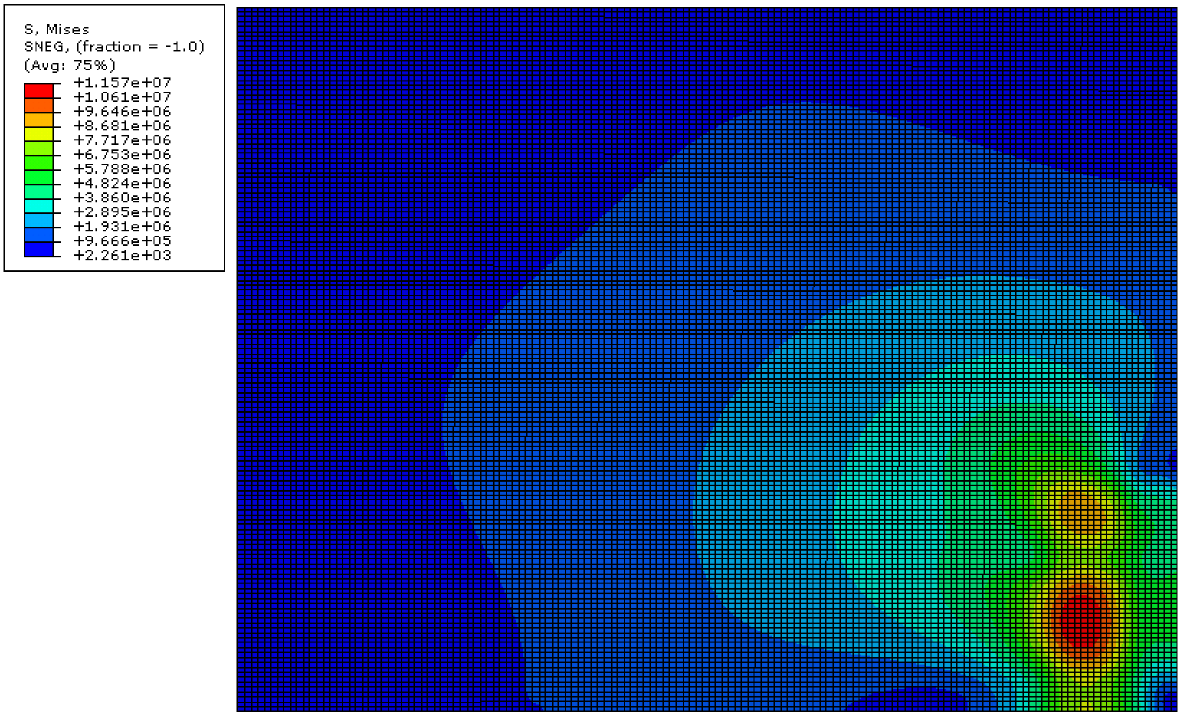

Figure 5-16: Transparent layer stress contours under static, corner load with HMA base

Figure 5-17 demonstrates the maximum stress in the transparent layer as a result from the fatigue load application.

Under the fatigue load case the pattern of the transparent layer stress changes dramatically from the static load case. This is because the load being applied is lower, but has a larger width on the glass surface due to the dual tire configuration of an ESAL. As a result of the lower load and larger application area, the maximum stresses are much smaller than under the static load case. The stress contour from the fatigue, centre load with an HMA base can be found in Figure 5-18, and this image demonstrates again that the maximum stresses occur in the cantilevered glass sections.

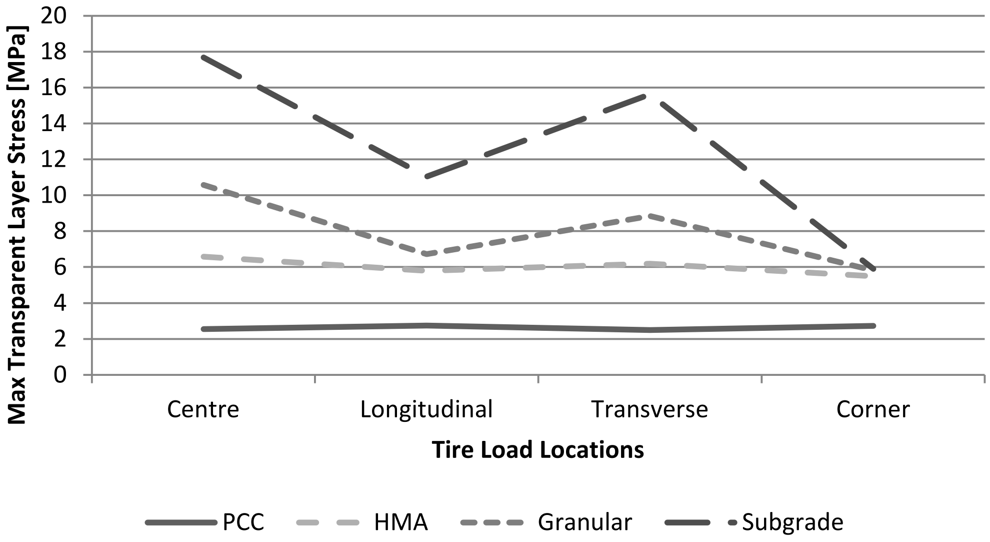

Figure 5-17: Transparent layer stress when subjected to fatigue load

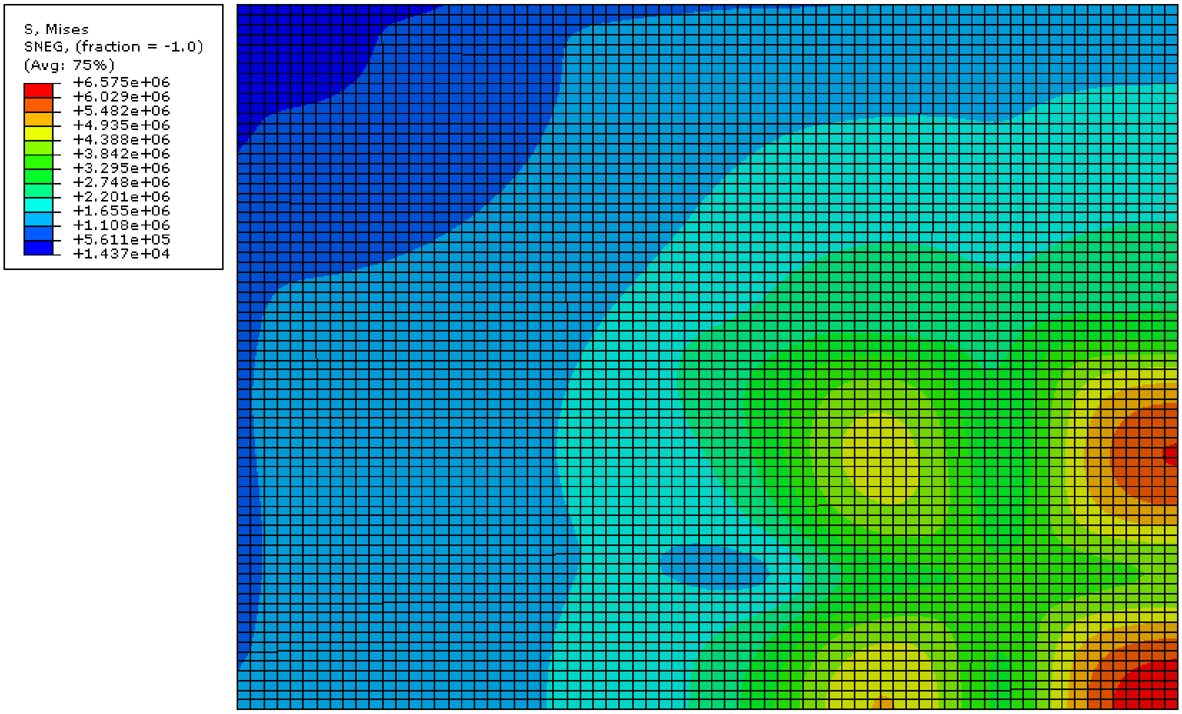

Figure 5-18: Transparent layer stress contours under fatigue, centre load with HMA base

5.3.2.2 Base Layer Stress

The second benchmark is the stress that is developed in the base layer. This characteristic is also important to determine the structural capacity of the panels to vehicle loading as values under 55-MPa are required to avoid yielding, and the results found are shown in Figure 5-19.

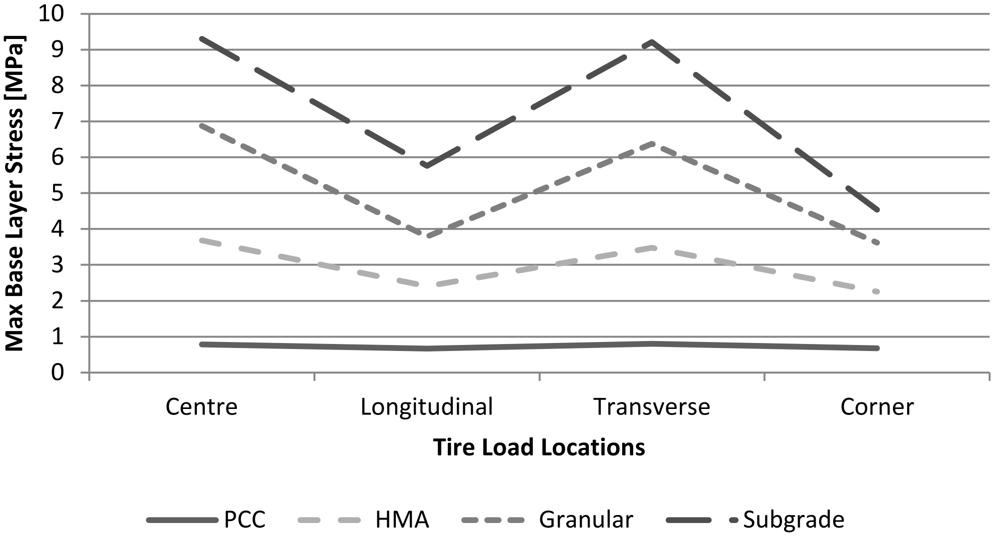

Figure 5-19: Base layer stress when subjected to static load

These results for maximum base layer stress follow the same pattern as was noted for the maximum optical layer stress, which was expected. These maximum stresses developed under the ribbed sections from the optical layer, as shown in Figure 5-20, with the values decreasing as you get farther from the loaded area. It is important to note that the maximum stresses achieved are well under the 55-MPa yield strength of GPO-3, so these components also will not fail due to static loading.

The base layer stress for the fatigue load case, as shown in Figure 5-21, also produces similar results to the static load case but with much lower peaking under the transverse load condition.

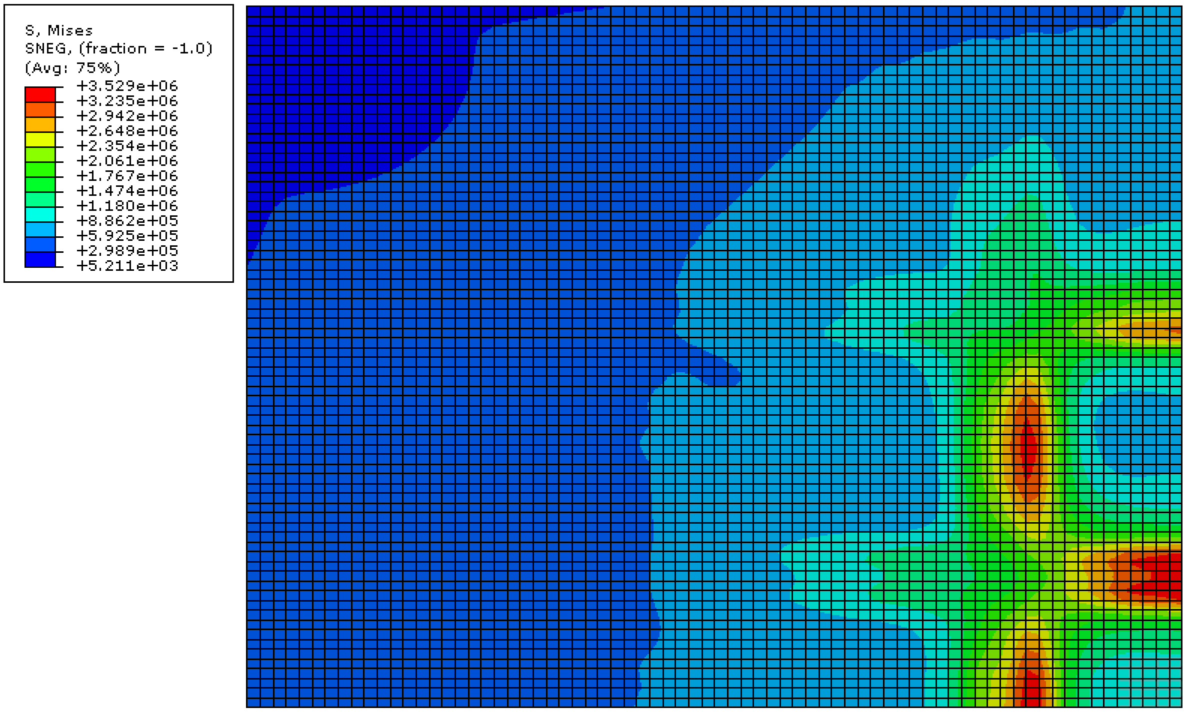

Figure 5-20: Base layer stress contours under static, centre load with HMA base

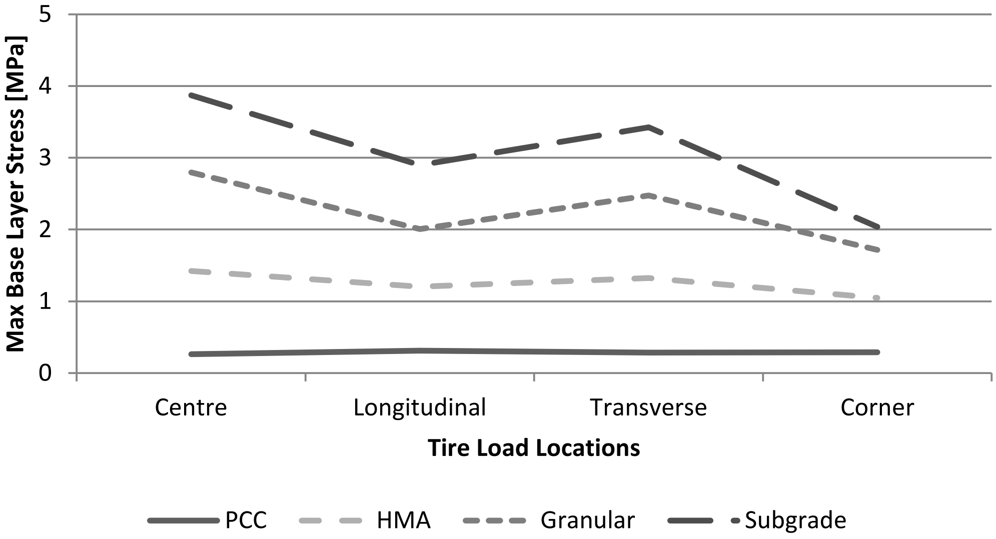

Figure 5-21: Base layer stress when subjected to fatigue load

5.3.2.3 Base Layer Strain

The next benchmark is the strain developed in the base layer. This is important as the mechanical limits for solar cells are typically defined in terms of strain limits, so ensuring that this value is under 6,250-microstrain to prevent damage to the solar cells is critical to the design (Ritchie, 2003). The results for the maximum base layer strain under the static load case are found in Figure 5-22.

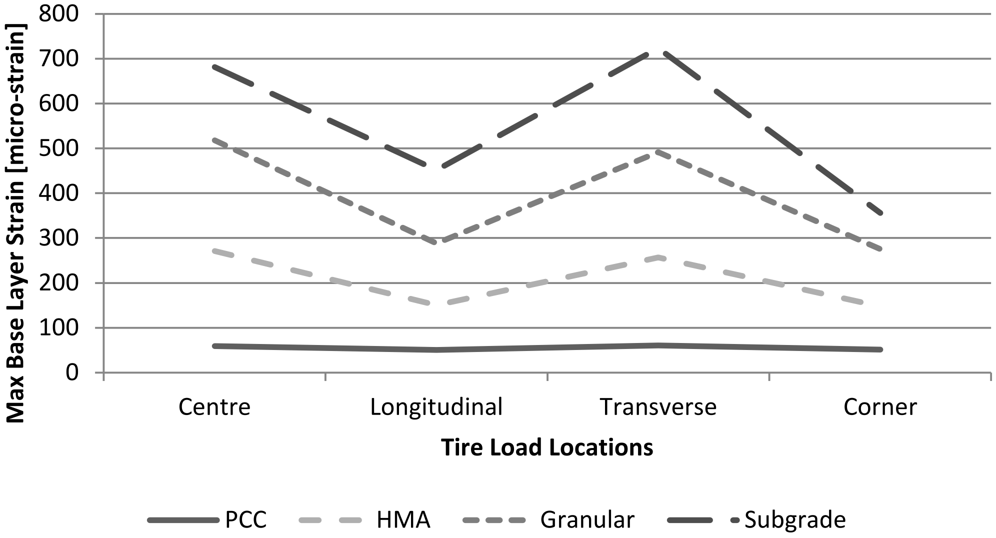

Figure 5-22: Base layer strain when subjected to static load

This figure follows the exact same pattern as the maximum base stress figure, as is expected due to the linear relationship between stress and strain during elastic deformation. It also shows that the maximum strains developed in the base layer are far below the 6,250-microstrain limit that the solar cells can be subjected to. Figure 5-23 shows the locations of these maximum strains and it is important to note that the maximum strains are located under the optical layer ribs and not in the solar cell cutouts, so the actual strains subjected to the solar cells will be far lower than noted in Figure 5-22.

The lower stress state of the fatigue load case produces significantly reduced strain profiles, as shown in Figure 5-24.

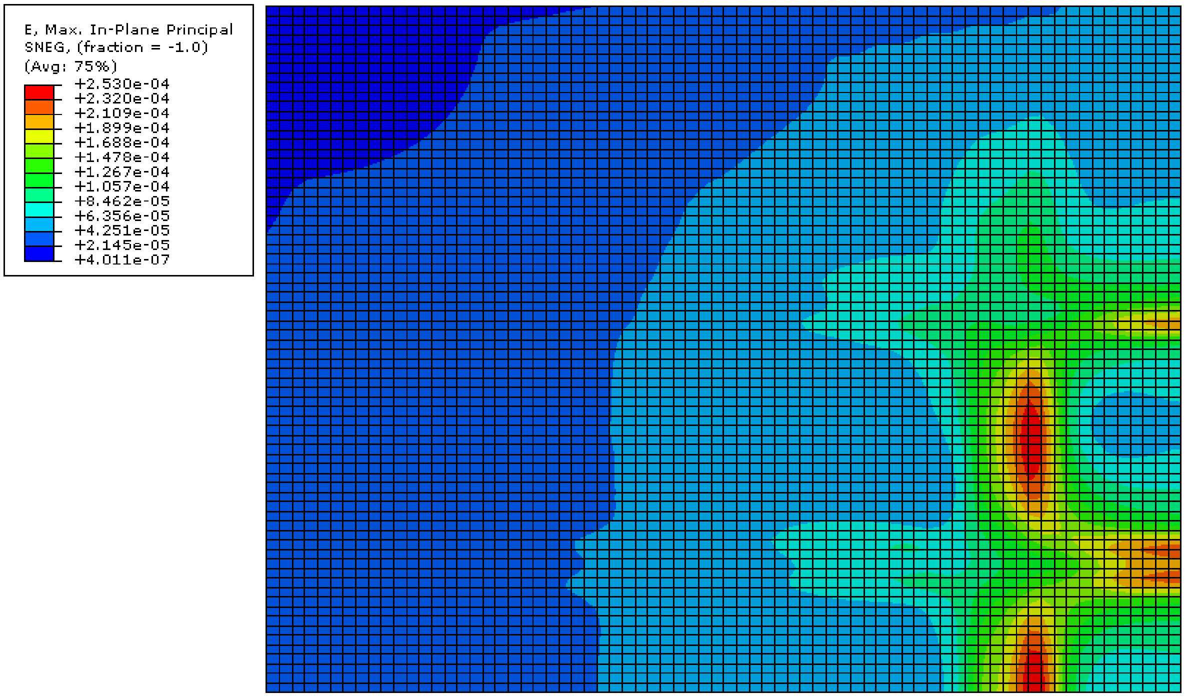

Figure 5-23: Base layer strain contours under static, centre load with HMA base

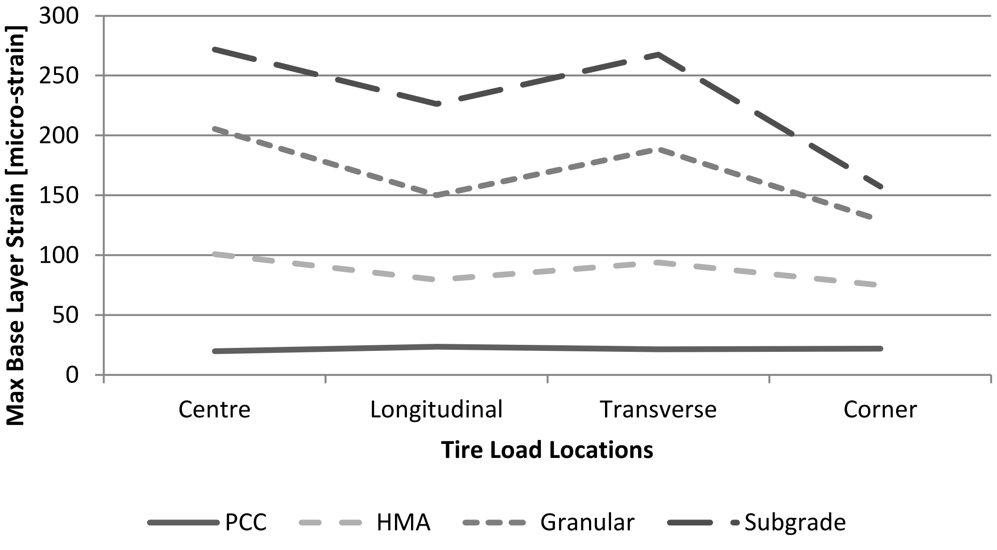

Figure 5-24: Base layer strain when subjected to fatigue load

5.3.2.4 Structural Base Deflection

The final benchmark being assessed is the maximum deflection measured within the structural base. This value is representative of the deflection caused in the panel. The results of this are shown in Figure 5-25.

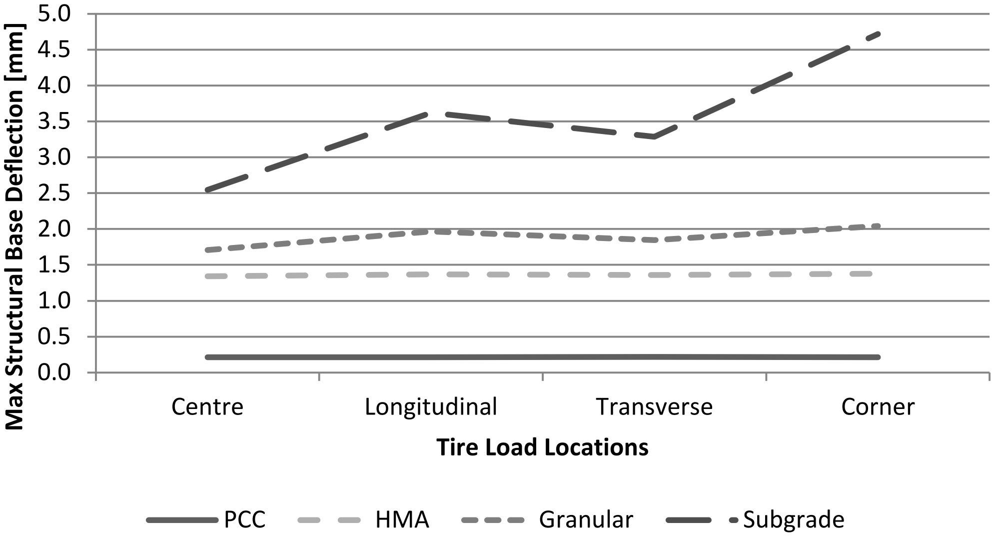

Figure 5-25: Structural base deflection when subjected to static load

The structural base deflections produce similar trends to the structural base strains shown in Figure 5-22, which again is logical due to the typical performance of plates used in pavement reinforcement. The profile of this deflection through the specimens is found in Figure 5-26, and this shows the expected maximum deflection under the loaded section with the deflection reducing quickly as you move away from this point.

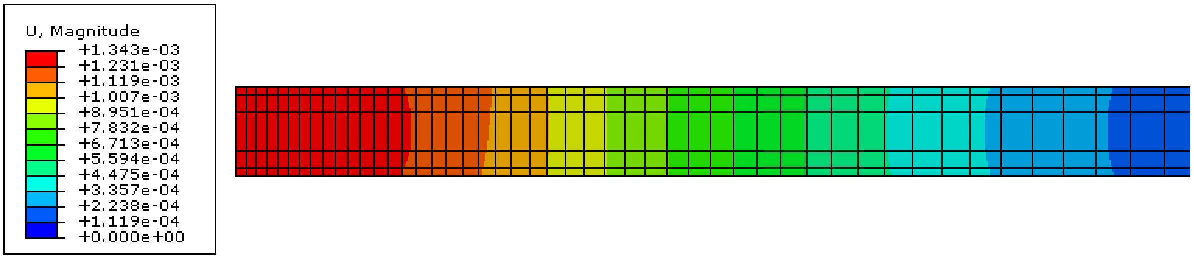

Figure 5-26: HMA layer deflection contours under static, centre load with HMA base

Figure 5-27 shows the structural base deflections determined from the fatigue load case. Once again these values are noticeably lower than those for the static load.

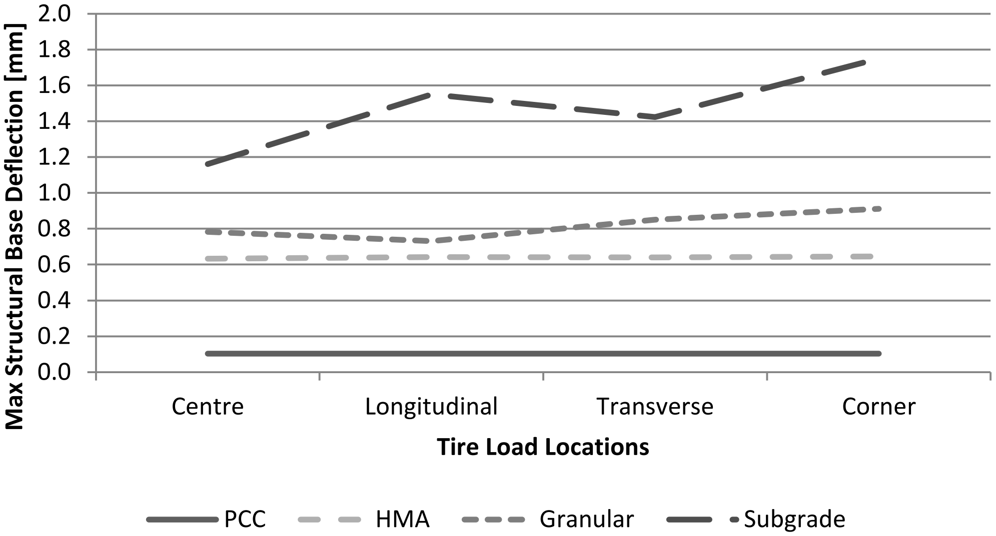

Figure 5-27: Structural base deflection when subjected to fatigue load

5.3.3 Fatigue Life Analysis

5.3.3.1 Transparent Layer

The first criteria for determining if the transparent layer is going to be subjected to fatigue cracking is comparing the maximum stresses developed to the compressive stress state established in the edges of the glass through tempering. In order to develop fatigue cracks there must be a net tensile stress applied to the surface, so the maximum stress measured must be higher than the inherent compressive stress in the glass. The minimum specification for tempered glass is a 69-MPa compressive edge stress. Figure 5-28 shows all of the maximum transparent layer stresses compared against the tempered edge stress.

Figure 5-28 clearly shows that the transparent layer in the prototype would not form fatigue cracks in these configurations. As a result, it is possible to reduce the thickness of the glass panes used in testing, in particular when the panel is installed on a PCC, HMA, or Granular structural base. As a result of this, no fatigue crack growth analysis was completed.

5.3.3.2 Optical and Base Layers

As identified in Figure 4-17, the fatigue criteria for E-glass reinforced polymers such as GPO-3 is based on a logarithmic relation of stress over ultimate stress to the number of cycles. This relation, however, is only valid when this stress ratio is over 0.3 as components have demonstrated infinite fatigue lives and lower stresses. As a result the first check to perform on the optical and base layers is to see if they surpass this limit, which is 16.6-MPa for GPO-3 laminates. This is shown below in Figure 5-29 for the base layer stresses, which in every case were higher than those in the optical layers.

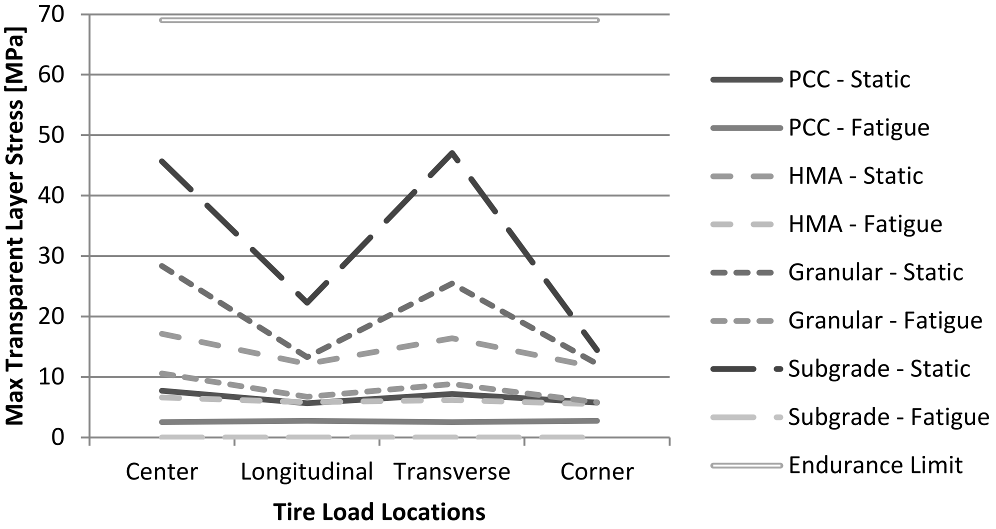

Figure 5-28: Transparent layer fatigue life endurance limit check

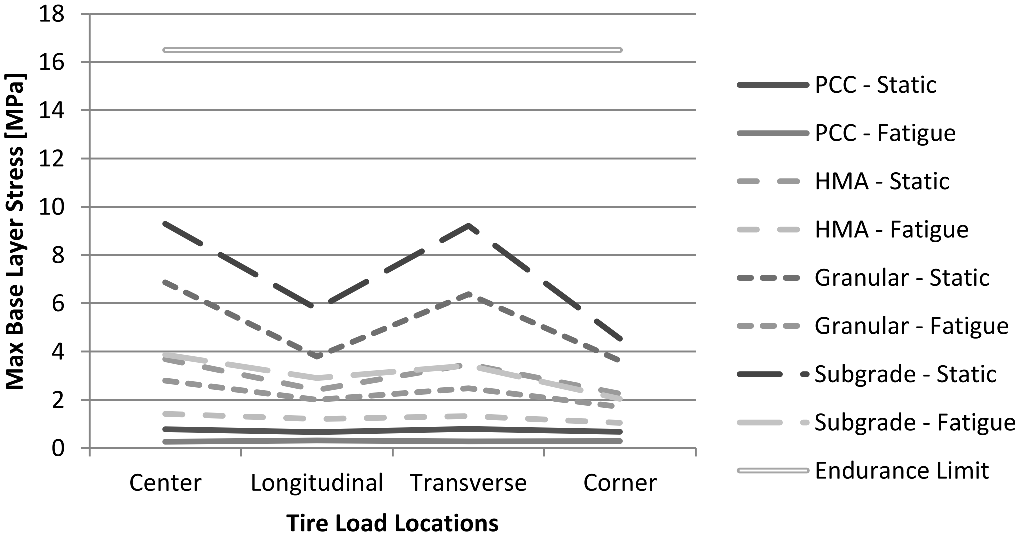

Figure 5-29: Base layer fatigue life endurance limit check

Figure 5-29 also clearly shows that the fiberglass components were designed under the endurance limit of GPO-3, so in the configurations with this prototype design they will not fail either due to cyclic loading.

5.3.3.3 Structural Bases

For the PCC bases, the important parameter for their design life is the stress developed in the layer. This value for the fatigue load cases is plotted in Figure 5-30 against the endurance limit that was identified in Figure 4-18. This figure clearly shows that loads on a solar road panel that is placed above the centre of a concrete slab will do no damage to the concrete slab or underlying structure. The large margin by which the centre-slab stress is under the endurance limit is also an indicator that loading through a solar road panel onto the transverse edge, longitudinal edge, or corner of a concrete slab would also create stresses under the endurance limit.

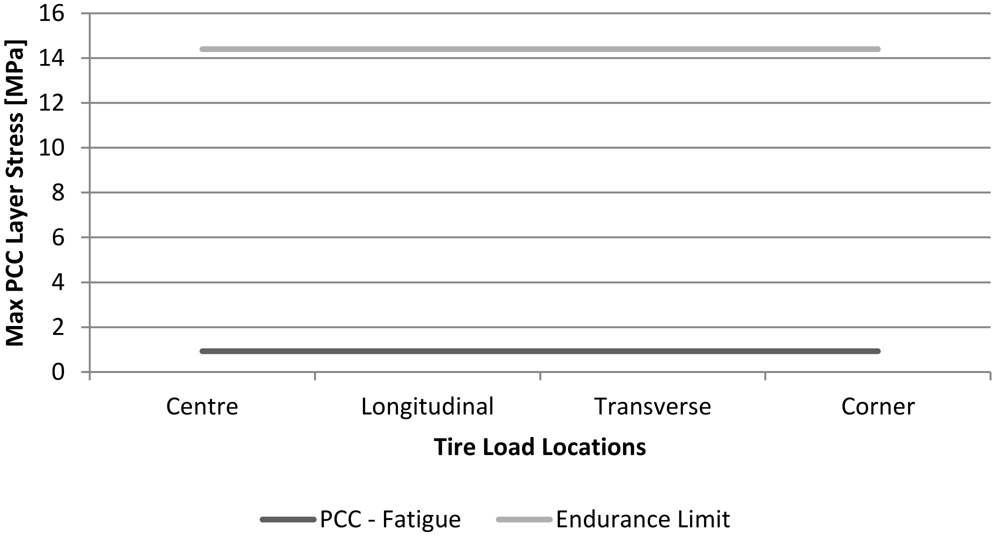

Figure 5-30: PCC layer fatigue life endurance limit check

For the HMA bases there are two critical performance parameters, the horizontal strain at the bottom of the HMA layer and the vertical strain at the bottom of the granular layers. The horizontal strain has a direct empirical relation to fatigue cracking life, where lower developed strain results in longer pavement life. The results noted from this analysis are shown in Figure 5-31 and are compared to the strain developed with the same structural base model without the panel. This figure shows that under the different load conditions the horizontal strain either remains the same or decreases versus the control, so installing a solar road panel on an asphalt pavement structure increases the fatigue cracking life of the asphalt pavement base.

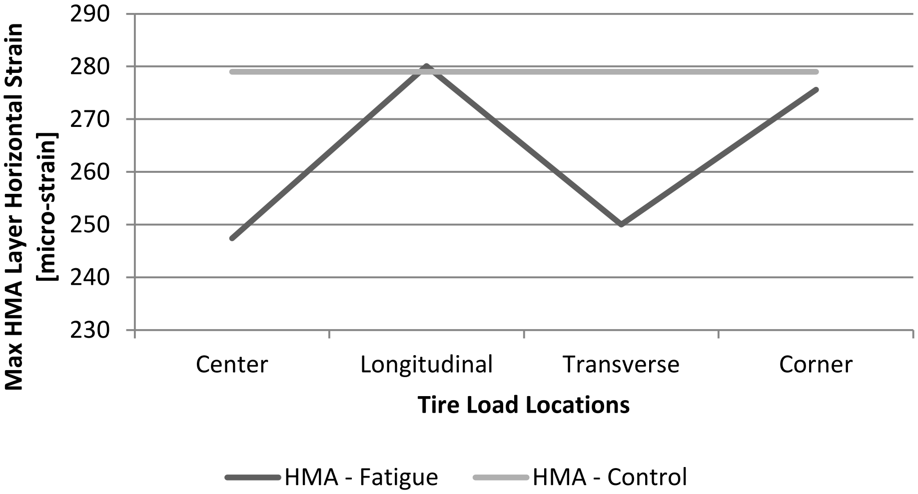

Figure 5-31: HMA layer maximum horizontal strain

In terms of the vertical compressive strain on the Granular B layer in the HMA base an even greater performance improvement is realized by installing the solar road panel. Once again the relation identified in Figure 4-20 indicates that lower strains result in higher rutting resistance, and in each case the solar road panel installation reduces the vertical compressive strain realized in the Granular B layer.

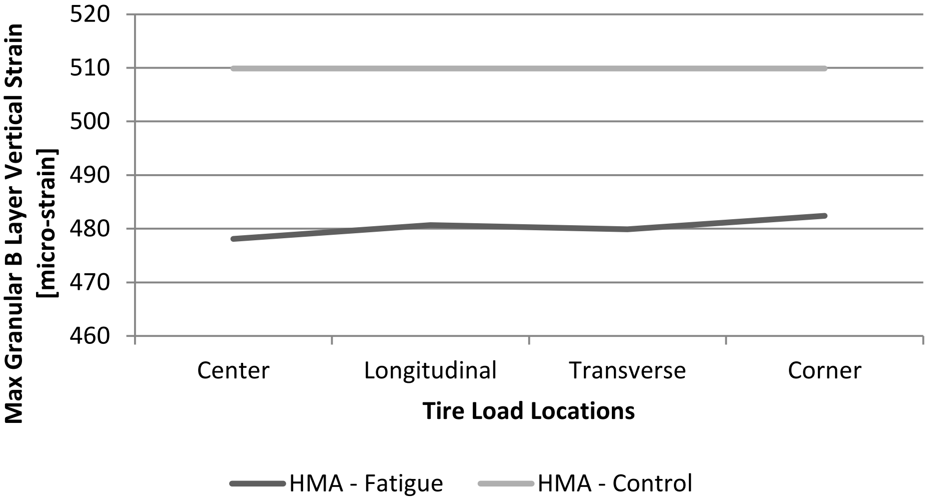

Figure 5-32: HMA base maximum vertical compressive strain in the Granular B layer

The vertical compressive strain on the Granular B layer in the granular base, as shown in Figure 5-33, followed the same trend as identified within the HMA base; adding the solar road panel to the structure increases the rutting resistance of the base in all load conditions.

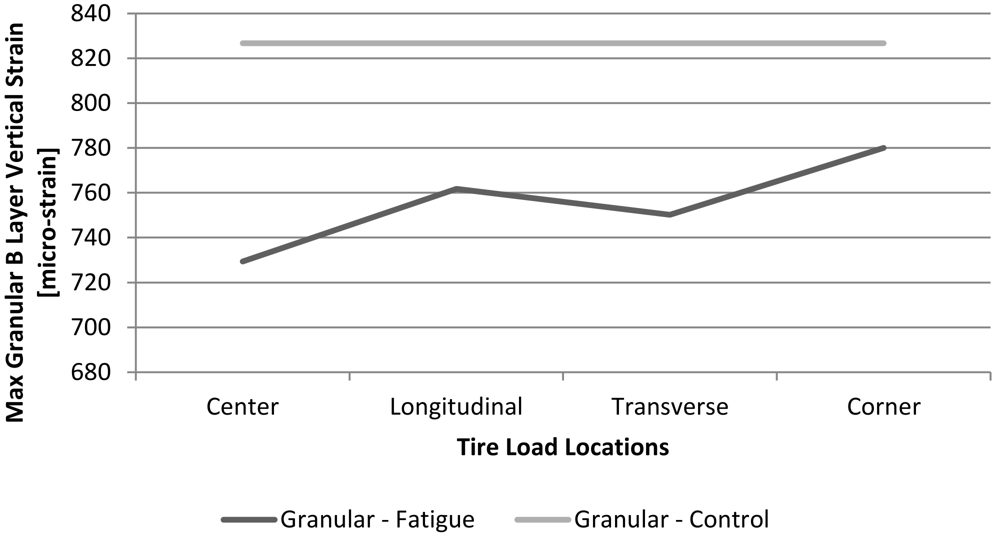

Figure 5-33: Granular base maximum vertical compressive strain in the Granular B layer

5.4 Summary of Key Findings

The first key finding of this section is that it is possible to design and construct a solar road prototype with highly predictable performance. The structural testing and finite element analysis described above thoroughly demonstrate that solar road panels react to loads following traditional material science and can therefore easily have their performance predicted by simulation.

This section also identified that it is possible to build a panel that can withstand the structural loads that pavements are subjected to while incorporating a photovoltaic electrical system. This was demonstrated through the finite element and fatigue analyses which showed that the prototype that was designed and constructed would need to be subjected to far higher loads than traditional vehicle loads in order to induce fatigue based failures. It was also shown that the electrical system would not be damaged through the strain cycling that the solar cells would be subjected to; an important metric for a solar road panel.

Lastly, this section clearly identified that adding solar road panels to the top of existing pavement structures improves their performance or, at worst case, does not change it. This indicates that introduction of the panels provide pavement engineers an opportunity to reduce the amount of traditional paving materials they use in the structural design, which reduces costs and potentially improves the overall sustainability of pavements. The concrete base provides the largest opportunity for optimization, so this will likely be the preferred base choice for solar road panel installations.

Chapter 6

Environmental Material Testing Results and Analysis

Consideration of the environmental performance of potential transparent layer materials, as outlined in the methodology, is detailed in this chapter.

6.1 Scaling Resistance Testing

During the scaling process, no notable effects of scaling were observed on any of the specimens. The changes occurring to the materials were believed to occur at a macroscopic level on the surface. The most noticeable effect that occurred during testing was an accumulation of salt residue on the samples, as identified in Figure 6-1. Figure 6-1 shows examples of glass, acrylic, and polycarbonate (from top to bottom) 3-point bending specimens that had been subjected to 50 freeze-thaw cycles. The specimens on the left are from the normal set while the specimens on the right are from the scaled set.

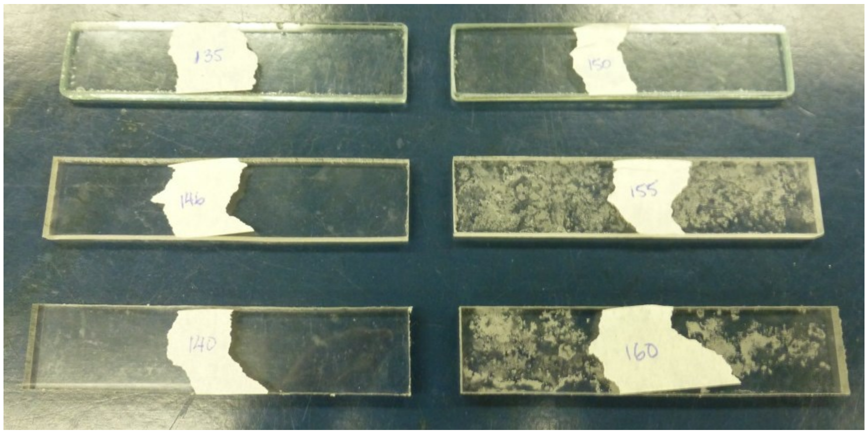

Figure 6-1: Salt accumulation during scaling resistance testing

6.2 Three-Point Bending Testing

6.2.1 Testing Results

The three-point bending test results were collected in terms of compressive load and extension from the datalogger connected to the Instron tester. This data then had to be processed in order to determine the flexural modulus of the materials. The range of information required for the flexural modulus is early in the testing data, before any plastic effects can be determined. Figure 6-2 shows the raw extension and load output for the first tested glass sample, where the peak represents the load at which the sample failed through brittle fracture.

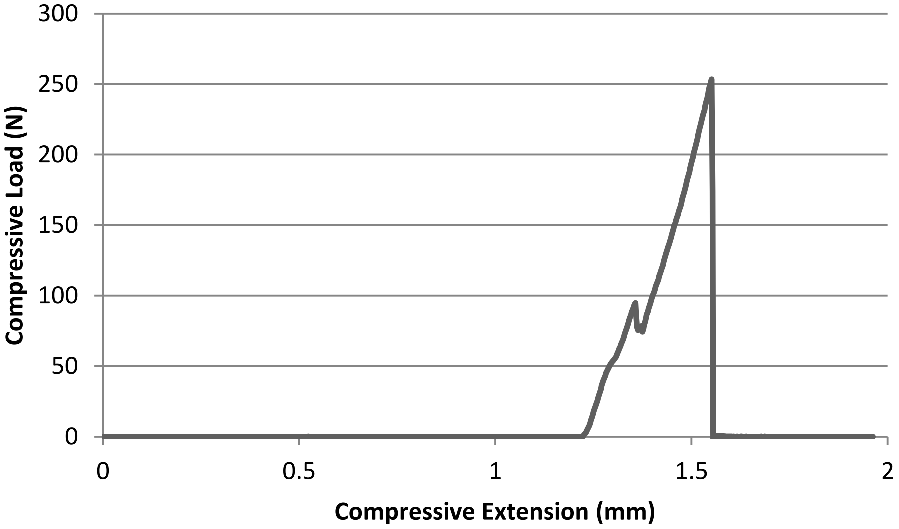

Figure 6-2: 3-point bending raw data for G-0-1

Since glass is a Hookean material, the straight sloping profile until failure was expected for each sample. What was not expected was the dip in the compressive load at approximately 95-N of loading. This dip was apparent in all of the testing data for all of the materials, so it was determined that the dip was caused by settling that was occurring in the testing rig repeatedly at this load. In order to determine the flexural modulus of the materials accurately, the starting point for the flexural measurement was taken after the dip occurred with the ending point being taken from later in the straight portion of the curve in a consistent manner for each material. All of the calculations based on this data were performed as outlined in ASTM D-790.

6.2.1.1 Acrylic Samples

The raw data from the first acrylic test is demonstrated in Figure 6-3. It follows the expected profile of a thermoplastic polymer, where there is a definite elastic deformation region followed by elastic-plastic deformation and then failure. Careful inspection of Figure 6-3 shows a slight adjustment to the elastic curve around the 95-N loading, as noted before.

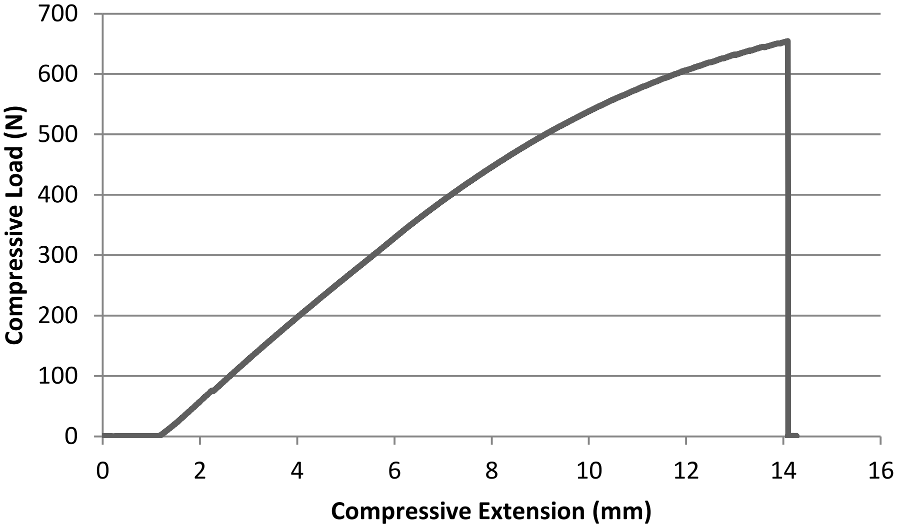

Figure 6-3: 3-point bending raw data for A-0-1

The data output from the testing is summarized in Table 6-1. This data demonstrates that the average flexural modulus remained relatively consistent despite the scaling and freeze-thaw effects. These results are further backed by the very low relative standard deviations, demonstrating the resilience and consistency of the material tested.

Table 6-1: Acrylic 3-point bending results

Conditioning	Measurement	Freeze-Thaw Cycles					
		0	5	10	15	25	50
Normal	**Average Flexural Modulus (GPa)**	**3.21**	**3.18**	**3.13**	**3.19**	**3.27**	**3.17**
	RSD (%)	*3.6*	*3.5*	*2.5*	*2.2*	*3.2*	*3.2*
Scaled	**Average Flexural Modulus (GPa)**	**3.21**	**3.11**	**3.16**	**3.11**	**3.23**	**3.18**
	RSD (%)	*3.6*	*2.0*	*2.9*	*3.9*	*7.0*	*3.5*

The one high RSD, 7.0% for the 25th cycle of the scaled set, is due to a sample that had an abnormally high modulus value from testing. Analysis of the results and specimen could not determine a cause for this variation so the sample was still included in the results. Removal of this sample from the testing pool only reduced the average modulus by 0.08 GPa and the RSD by 2.0%.

6.2.1.2 Glass Samples

The raw data from the glass testing was demonstrated in Figure 6-2, and as described this profile followed the expected results for flexural testing of a glass specimen. The material is very brittle in nature, so the material accepts the load elastically until it reaches its brittle failure point and then shatters. The typical glass specimen failed under flexural load as demonstrated in Figure 6-4.

Figure 6-4: Typical glass 3-point bending test failure (Specimen G-15-US-3)

As shown in Figure 6-4, there was a dominant side from which the failure cracks originated. This was consistent across all of the samples as there was a marginal alignment error between the load nose and the samples under the bending test.

One of the challenges with working with glass is that there is a high variability in the distribution of particles in the glass matrix. This results in some unpredictability in the properties of the materials as the particle distribution also affects where the dislocations are in the material that are where failure cracks will propagate from. This is apparent in the initial results from the 3-point bending testing, which are demonstrated in Table 6-2.

Table 6-2: Glass 3-point bending initial results

Conditioning	Measurement	Freeze-Thaw Cycles					
		0	5	10	15	25	50
Normal	**Average Flexural Modulus (GPa)**	**47.5**	**49.3**	**47.2**	**42.2**	**48.9**	**45.8**
	RSD (%)	*6.3*	*4.2*	*6.2*	*43*	*4.8*	*19*
Scaled	**Average Flexural Modulus (GPa)**	**47.5**	**47.5**	**51.2**	**38.1**	**50.5**	**47.6**
	RSD (%)	*6.3*	*3.7*	*2.6*	*22*	*3.8*	*2.3*

While most of the data set had low RSD values, the 15th and 50th normal cycles and the15th scaled cycle stand out for their very high RSD values of 43%, 19%, and 22% respectively. While there were no discrepancies in the failure mechanisms of the samples in G-15-S, both of the other sets had an odd sample failure that implied an unusual defect in the sample being tested. Figure 6-5 demonstrates these two failure mechanisms, where sample G-15-N-1 broke in a near perfect shear failure and sample G-50-N-1 broke in a more dramatic bending failure than the typical sample identified in Figure 6-4.

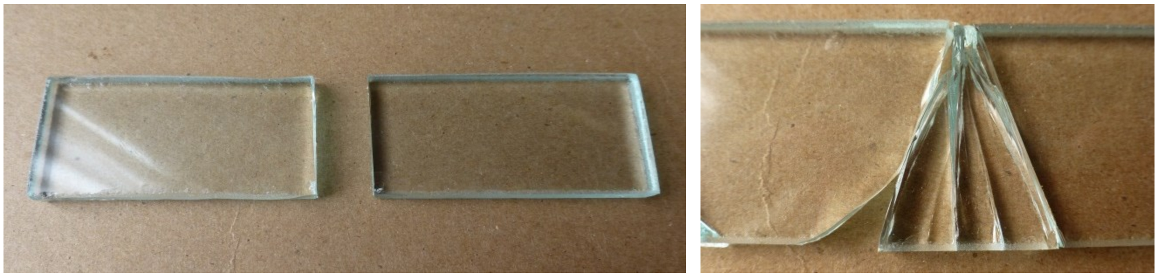

Figure 6-5: Irregular failures of samples a) G-15-N-1 and b) G-50-N-1

With these samples eliminated as outliers, the updated results from the flexural modulus testing are shown in Table 6-3. While the RSD for 15th scaled cycle remains high, the RSD values for 15th and 50th normal cycles have been reduced to 3.9% and 2.3% respectively. This indicates a much more accurate sampling of real flexural modulus data.

Table 6-3: Glass 3-point bending final results

Conditioning	Measurement	Freeze-Thaw Cycles					
		0	5	10	15	25	50
Normal	**Average Flexural Modulus (GPa)**	**47.5**	**49.3**	**47.2**	**51.3**	**48.9**	**49.5**
	RSD (%)	*6.3*	*4.2*	*6.2*	*3.9*	*4.8*	*2.3*
Scaled	**Average Flexural Modulus (GPa)**	**47.5**	**47.5**	**51.2**	**38.1**	**50.5**	**47.6**
	RSD (%)	*6.3*	*3.7*	*2.6*	*22*	*3.8*	*2.3*

6.2.1.3 Polycarbonate Samples

The raw data from the first polycarbonate test is demonstrated in Figure 6-6. It follows the expected profile of polycarbonate, which is a specialized thermoplastic polymer that can undergo large plastic deformations without crack development. The testing of these samples was terminated after an extension of 30.5-mm due to the lack of a brittle failure in the material. Careful inspection of Figure 6-6 shows a slight adjustment to the elastic curve around the 95-N loading, as noted before.

The data output from the testing is summarized in Table 6-4. This data demonstrates that the average flexural modulus remained relatively consistent despite the scaling and freeze-thaw effects. These results are further backed by the very low relative standard deviations, demonstrating the resilience and consistency of the material tested.

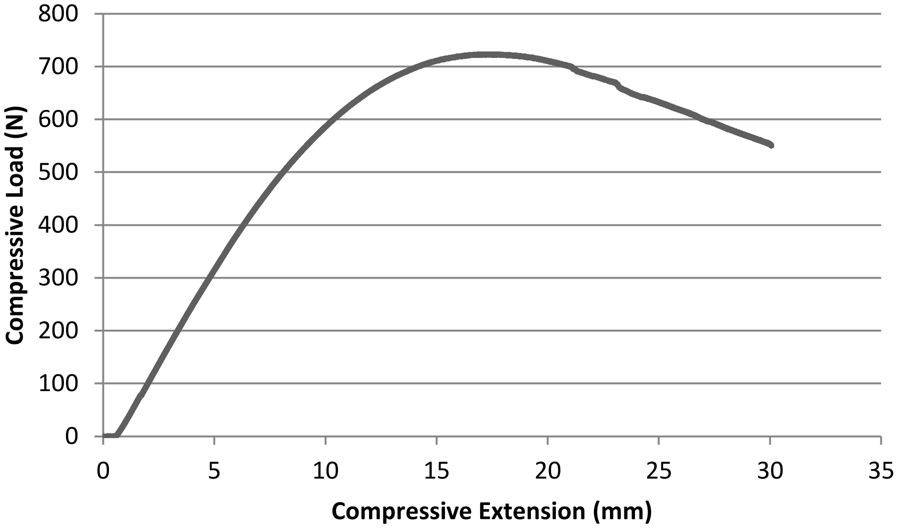

Figure 6-6: 3-point bending raw data for P-0-1

Table 6-4: Polycarbonate 3-point bending results

Conditioning	Measurement	Freeze-Thaw Cycles					
		0	5	10	15	25	50
Normal	**Average Flexural Modulus (GPa)**	**2.46**	**2.35**	**2.39**	**2.37**	**2.41**	**2.44**
	RSD (%)	*3.3*	*2.7*	*2.7*	*1.8*	*1.8*	*1.3*
Scaled	**Average Flexural Modulus (GPa)**	**2.46**	**2.40**	**2.42**	**2.40**	**2.42**	**2.47**
	RSD (%)	*3.3*	*1.8*	*1.1*	*2.3*	*1.4*	*1.0*

6.2.2 Material Comparison

Figure 6-7 shows a comparison of the flexural stress response of the three materials tested, the same three specimens profiled in Section 6.2.1, to displacement. This graph much more clearly identifies the differences between these three materials in terms of their flexural performance.

The figure demonstrates that the glass specimens are much more fragile than both of the polymer options, with failure occurring at around 50-MPa of flexural stress and at well under 1-mm of displacement. However, it is important to note that minimal deflection was outlined as a design requirement for a solar road module so that the solar cells would not be damaged from vehicle traffic. The stress at which the glass fails is an equivalent stress to the acrylic and polycarbonate samples at approximately 4-mm and 5-mm respectively.

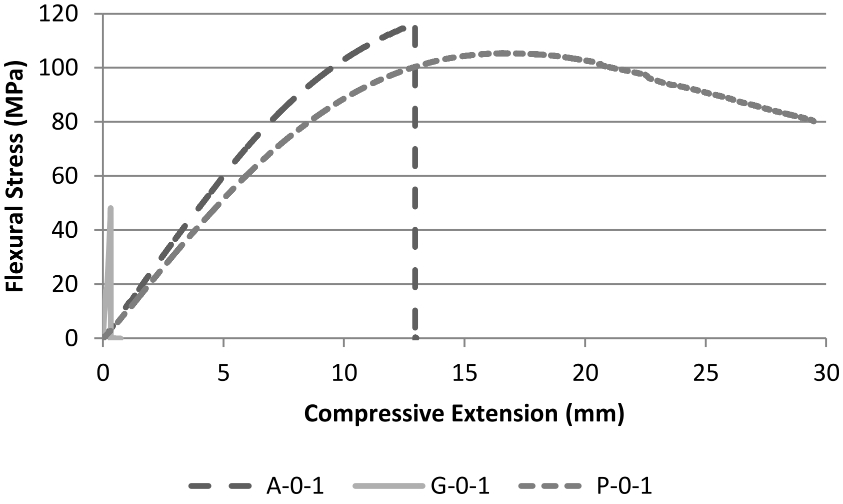

Figure 6-7: Comparative material flexural stress response to displacement

Not only does the lower rigidity of the polymer options impact deflection over the solar cells, it also places a greater emphasis on the rigidity of the panel being based in the structural layer materials. In the current prototype design this is inverted as the rigidity is largely based on the tempered glass optical layer with the fiberglass structural layers acting as support. In a design with acrylic or polycarbonate as the optical layer, aluminum, steel, or some other structural metal would likely be required for the structural layers to make the entire panel rigid enough to minimize stresses on the solar cells.

6.2.3 Statistical Analysis

Table 6-5 summarizes the results of the two-factor ANOVA completed on each material set. The null hypotheses are that the scaled samples will demonstrate a lower flexural modulus than the normal samples, and that the performance gap between them will increase with increasing numbers of freeze-thaw cycles.

Table 6-5: 3-point bending ANOVA results

Material	Variable	F-crit.	F-calc.	P-Value	Null Hypothesis	Statistical Significance
Acrylic	Conditioning	6.61	2.08	0.209	Failed	Same
	Freeze-Thaw	5.05	1.07	0.469	Failed	Same
Glass	Conditioning	6.61	0.61	0.471	Failed	Same
	Freeze-Thaw	5.05	0.36	0.855	Failed	Same
Polycarbonate	Conditioning	6.61	12.96	0.015	Passed	Different
	Freeze-Thaw	5.05	14.62	0.005	Passed	Different

The results in Table 6-5 demonstrate that while there are no measureable trends in the flexural modulus of acrylic of glass with respect to conditioning or freeze-thaw cycling, both trends are substantiated for polycarbonate. This is further demonstrated in Figure 6-8, which shows the average flexural modulus of the normal and scaled polycarbonate samples and plots linear regressions to both data sets.

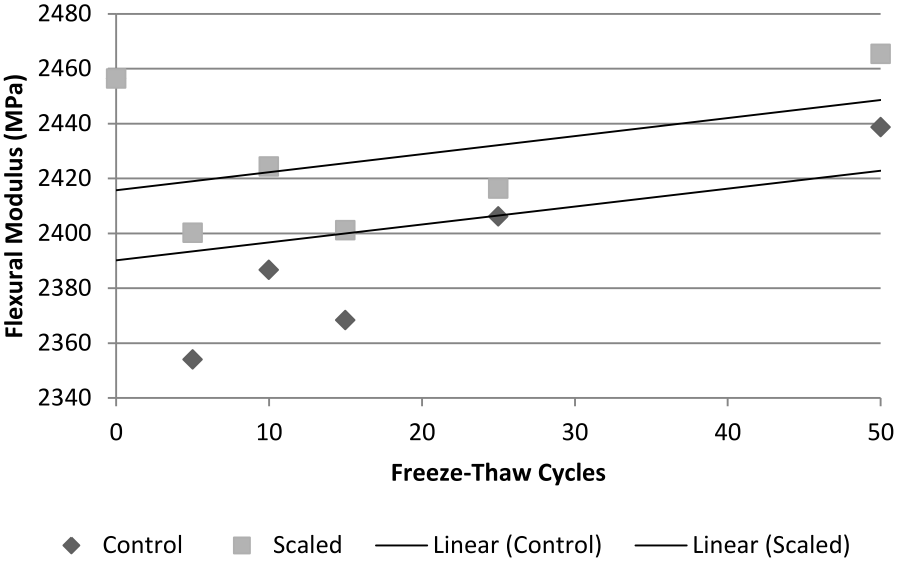

Figure 6-8: Polycarbonate flexural modulus results

Figure 6-8 demonstrates that the scaled specimens perform better than the normal specimens, which is the opposite of what was believed would occur. The general drop in performance and then steady increase of both sets is likely due to an adjustment of the polymer chains within the material that causes an immediate weakening and then steadily strengthens the material over time. The difference in the magnitude of this change between the normal and scaled samples is due to the way the normal samples were conditioned; in air as opposed to submerged. It is believed that the salt brine provided greater thermal insulation to those specimens during the cycling, so they saw less dramatic temperature induced polymer chain relocations. Further study would be required to validate this hypothesis.

Also notable from Figure 6-8 is that the ‘0’ freeze-thaw cycle control set appears to be an outlier from determining a strong linear correlation between freeze-thaw cycles and flexural modulus for both conditions. This is highlighted below in Table 6-6 which shows the results of determining a linear regression fit to both the total and ‘0’-excluded polycarbonate data sets. While the complete set of data does not demonstrate a statistically significant regression, both of the conditions with the ‘0’ set excluded are statistically significant. The ‘0’-excluded data set and regressions are shown in Table 6-6.

Table 6-6: Polycarbonate 3-point bending regression analysis

Data Set	Condition	Intercept	Variable	P-Value	R-squared
All	Control	2390	0.65	0.57	0.09
	Scaled	2416	0.66	0.40	0.18
‘0’ Excluded	Control	2354	1.75	0.02	0.88
	Scaled	2394	1.33	0.04	0.79

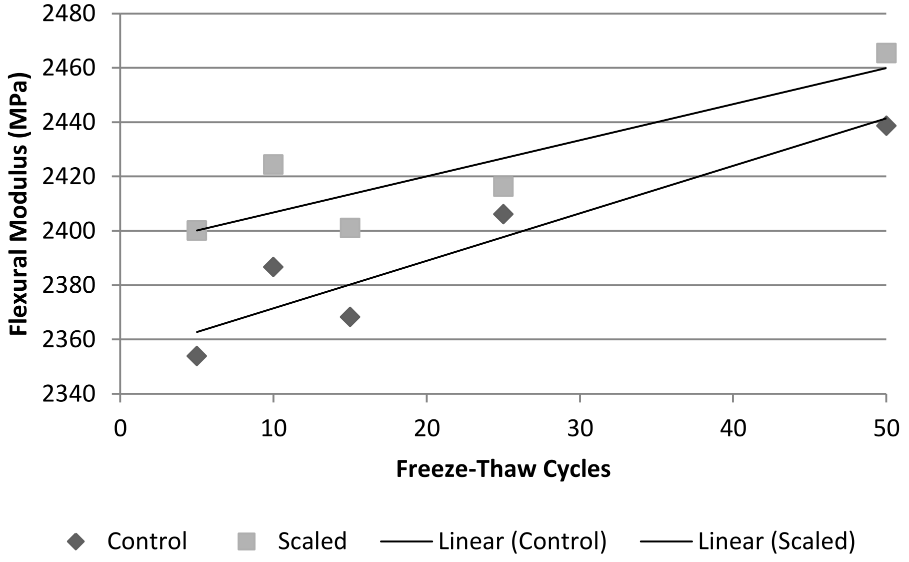

Figure 6-9: Polycarbonate flexural modulus results, excluding '0' cycle data

6.3 Friction Testing

The results from the friction testing of the samples are shown below in Table 6-7. This table shows the average BPN measured at each stage of process and the RSD of each average. For a typical pavement a BPN of 40 provides an excellent wet frictional characteristic for driving on, however all of these tests demonstrate that acrylic, glass, and polycarbonate would require significant micro- and macro-texture improvements to provide enough wet friction as a driving surface.

For the most part the RSD values are low, though for the 10th and 15th cycle data these values are consistently above 10% and in some cases come as high as 30%. This is related to the fact that it is a small range and any variation in the BPN will have a large impact due to the already low average BPN values, though further studies should include a larger sample to minimize this variation.

Table 6-7: Friction testing results

Material	Condition	Measurement	Freeze-Thaw Cycles					
			0	5	10	15	25	50
Acrylic	Control	**Avg. BPN**	**5.4**	**5.2**	**6.6**	**7.7**	**9.7**	**13.7**
		RSD (%)	13.3	5.59	19.5	31.0	5.97	18.5
	Scaled	**Avg. BPN**	**5.1**	**6.5**	**7.6**	**7.6**	**9.8**	**15.8**
		RSD (%)	*2.84*	*10.2*	*13.3*	*11.6*	*25.6*	*8.70*
Glass	Control	**Avg. BPN**	**5.3**	**5.1**	**6.3**	**7.3**	**9.9**	**11.8**
		RSD (%)	*8.25*	*2.84*	*12.0*	*25.8*	*7.70*	*8.54*
	Scaled	**Avg. BPN**	**5.7**	**5.7**	**7.1**	**6.6**	**7.3**	**9.25**
		RSD (%)	*2.55*	*13.5*	*10.8*	*9.56*	*3.45*	*4.68*
Polycarbonate	Control	**Avg. BPN**	**6.0**	**6.8**	**8.2**	**8.9**	**9.3**	**10.8**
		RSD (%)	*4.17*	*7.41*	*20.4*	*13.3*	*10.1*	*6.15*
	Scaled	**Avg. BPN**	**7.3**	**6.7**	**8.4**	**11.3**	**10.0**	**13.7**
		RSD (%)	*3.94*	*23.8*	*6.86*	*23.2*	*6.61*	13.2

Figure 6-10 shows the comparative results of the friction testing between the three material sets. This chart shows that the performance of all of the materials was very similar, with a slightly higher BPN being noted for the polycarbonate samples over the first 15 cycles.

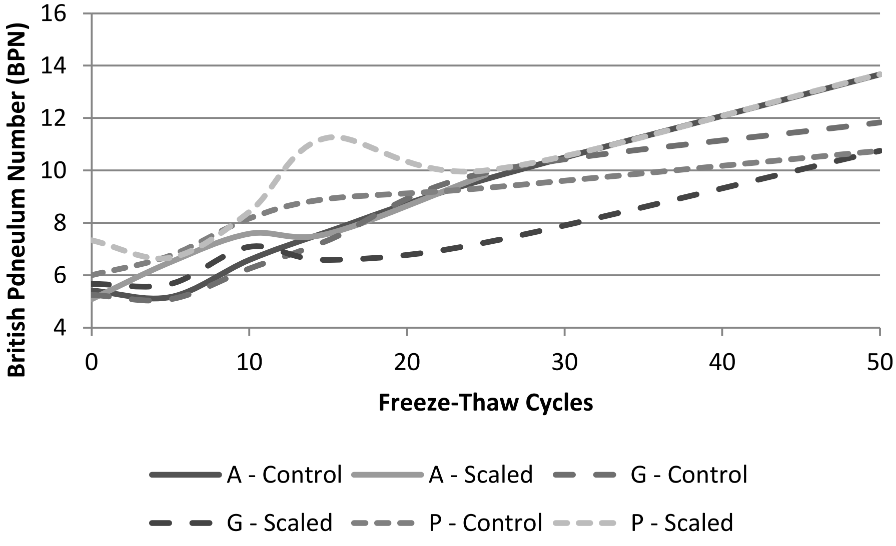

Figure 6-10: Friction testing results

A two-factor ANOVA was run for each of these materials and the results of this can be found below in Table 6-8. While in this analysis there was no statistical difference between the two types of conditioning, statistical differences were found for the freeze-thaw effect in all cases. It should be noted that the conditioning of the polycarbonate samples almost demonstrated a significant difference.

Table 6-8: Friction ANOVA results

Material	Variable	F-crit.	F-calc.	P-Value	Null Hypothesis	Statistical Significance
Acrylic	Conditioning	6.61	3.27	0.130	Failed	Same
	Freeze-Thaw	5.05	52.94	0.0002	Passed	Different
Glass	Conditioning	6.61	0.67	0.451	Failed	Same
	Freeze-Thaw	5.05	11.34	0.009	Passed	Different
Polycarbonate	Conditioning	6.61	6.48	0.052	Failed	Same
	Freeze-Thaw	5.05	13.05	0.007	Passed	Different

The trend established from the results of the acrylic testing is shown in Figure 6-11, where both trendlines have a clear increase of friction over increasing freeze-thaw cycling but that there is essentially no difference between the two conditioning methods. This increase, as there is no change between conditioning methods, is suspected to be related to temperature effects resulting in variations in the microtexture on the surface of the material.

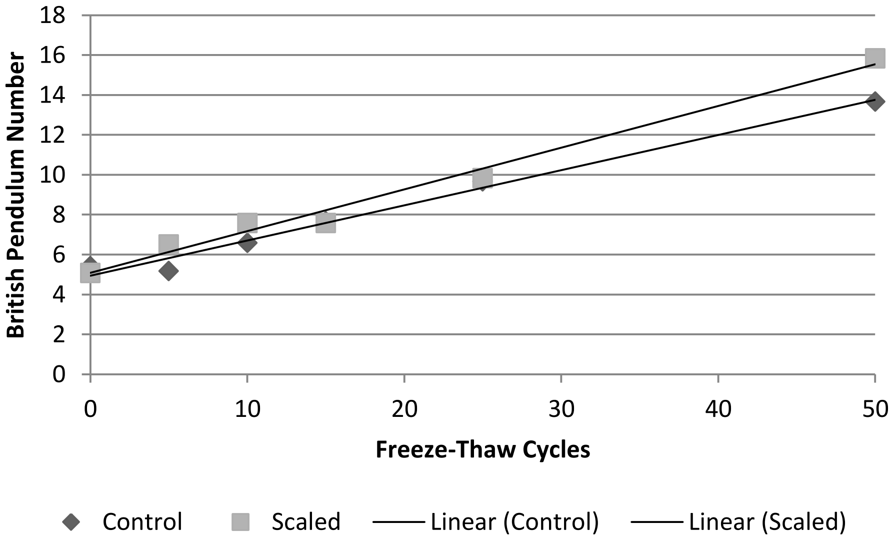

Figure 6-11: Acrylic friction results

The glass friction results are demonstrated in Figure 6-12 and show the steady increase of friction with freeze thaw cycling. While in this case the control samples tend to have higher friction readings, there was no statistically significant trend identified from the data.

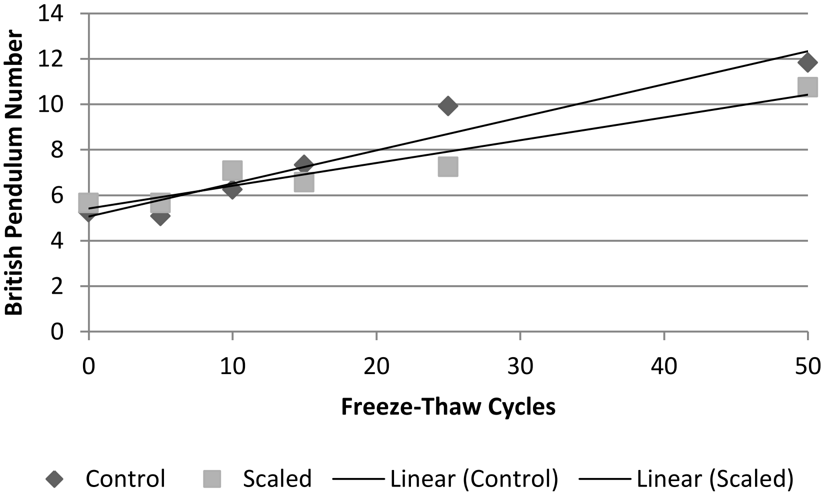

Figure 6-12: Glass friction results

The polycarbonate friction results, as shown in Figure 6-13, demonstrate that while the scaled samples continually demonstrate higher friction than the normal samples, the results of the two are still too similar to identify a difference between them. Overall there is still an increase in friction with increasing freeze-thaw cycling. Similar to the acrylic samples, the increasing friction is likely due to an impact of temperature cycling on the surface microtexture of the material.

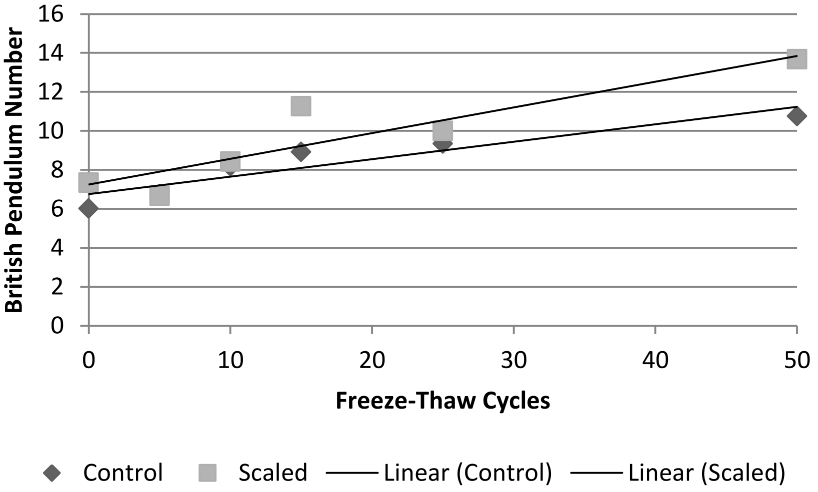

Figure 6-13: Polycarbonate friction results

The statistical parameters of the linear regressions demonstrated in Figure 6-11 through Figure 6-13 are shown below in Table 6-9. This data further demonstrates the strength of the correlations between freeze-thaw cycling and surface friction for all of the normal and scaled conditions of these samples.

Table 6-9: Friction linear regression results

Material	Condition	Intercept	Variable	P-Value	R-squared
Acrylic	Normal	4.942	0.176	8.7E-5	0.985
	Scaled	5.078	0.209	7.5E-5	0.986
Glass	Normal	5.064	0.146	0.0015	0.937
	Scaled	5.683	0.070	0.0023	0.922
Polycarbonate	Normal	6.754	0.089	0.0073	0.864
	Scaled	7.244	0.132	0.0120	0.826

6.4 Optical Testing

6.4.1 Acrylic Results and Analysis

The average results for transmission and reflection for the acrylic samples are shown in Table 6-10 along with the calculated absorption coefficient and the calculated RSD values for each parameter.

Table 6-10: Acrylic optical testing results

Property	Condition	Value	Freeze-Thaw Cycles					
			0	5	10	15	25	50
Transmissivity	Control	**Average**	**81.32**	**82.03**	**82.53**	**82.49**	**81.69**	**80.32**
		RSD (%)	0.60	0.76	0.20	0.59	0.73	3.88
	Scaled	**Average**	**81.32**	**82.68**	**82.23**	**82.83**	**82.26**	**81.81**
		RSD (%)	0.60	0.34	0.60	0.08	0.35	1.35
Reflectivity	Control	**Average**	**8.70**	**8.56**	**8.48**	**8.86**	**8.69**	**8.72**
		RSD (%)	1.96	4.09	5.04	2.60	2.59	0.28
	Scaled	**Average**	**8.70**	**8.78**	**8.74**	**8.89**	**8.85**	**8.76**
		RSD (%)	1.96	2.90	1.96	2.58	3.27	3.19
Absorptivity	Control	**Average**	**9.98**	**9.41**	**8.98**	**8.66**	**9.61**	**10.96**
		RSD (%)	3.80	9.66	6.27	3.11	7.94	28.64
	Scaled	**Average**	**9.98**	**8.54**	**9.03**	**8.28**	**8.90**	**9.44**
		RSD (%)	3.80	1.78	3.86	2.97	6.37	9.50

The very low RSD values demonstrated in Table 6-10 show that the values obtained from the testing are an accurate representation of the actual data. The highest RSD values are for the absorptivity measurements, though these high values are a result of summation errors from determining the absorptivity values.

Table 6-11 shows the results of a two variable ANOVA study on the transmissivity, reflectivity, and absorptivity properties of the acrylic samples. This study found that conditioning was a significant factor for both transmissivity and absorptivity while freeze-thawing was only significant for transmissivity, though it was close for absorptivity as well.

Table 6-11: Acrylic optical ANOVA results

Property	Variable	F-crit.	F-calc.	P-Value	Null Hypothesis	Statistical Significance
Transmissivity	Conditioning	6.61	9.58	0.027	Passed	Different
	Freeze-Thaw	5.05	5.82	0.038	Passed	Different
Reflectivity	Conditioning	6.61	0.40	0.554	Failed	Same
	Freeze-Thaw	5.05	0.27	0.911	Failed	Same
Absorptivity	Conditioning	6.61	9.11	0.029	Passed	Different
	Freeze-Thaw	5.05	4.60	0.060	Failed	Same

The results of Table 6-11 are further outlined below in Figure 6-14, which plots the average transmissivity values and the linear regression fits to this data. This figure also shows that the scaled samples showed a lower drop in transmissivity than the normal samples did, and this is believed to be due to the temperature effects outlined for the polycarbonate specimens in the three point bending testing analysis. The high variability of the scaled transmission values merits further analysis.

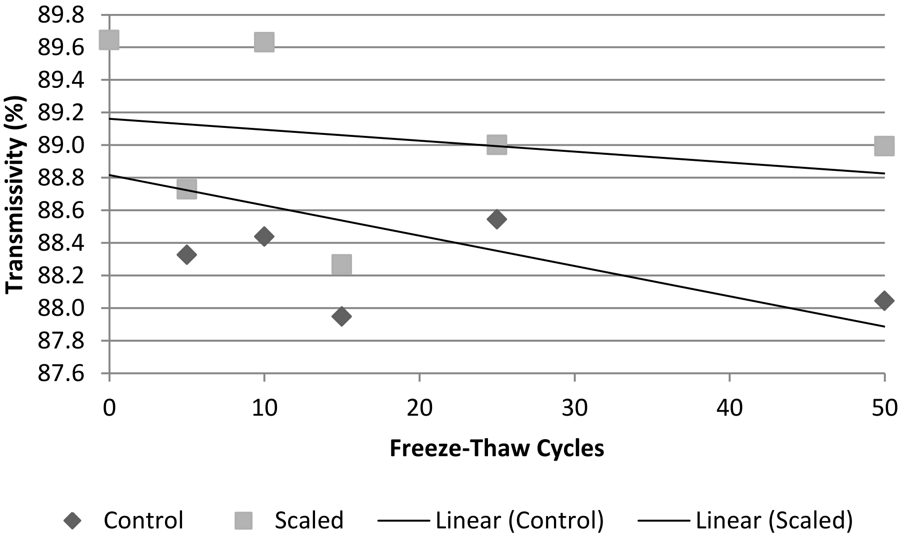

Figure 6-14: Acrylic transmission results

The graph for the average reflectivity values, as shown in Figure 6-15, shows the high variability of the results that was indicated by the ANOVA analysis.

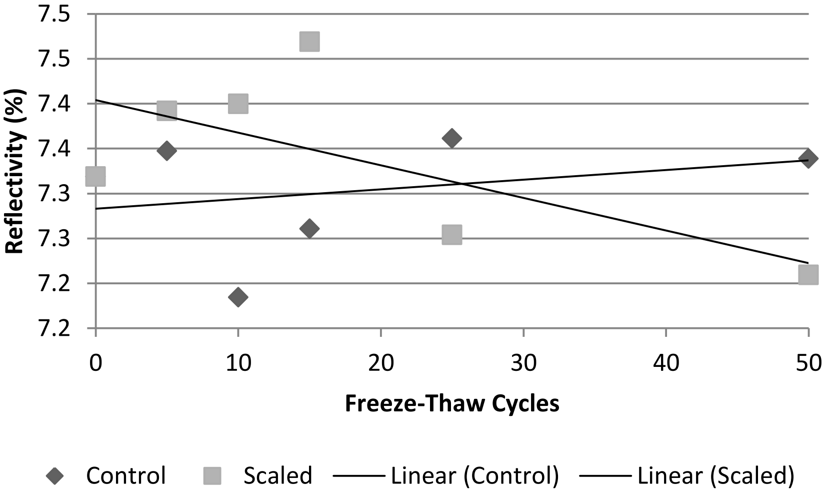

Figure 6-15: Acrylic reflectivity results

The results of the absorptivity calculation, as shown in Figure 6-16, show the close regression fits for increasing absorptivity with increasing freeze-thaw cycles. The result that the normal samples have a higher absorptivity than the scaled samples is believed to be the result of a polymer chain realignment as outlined in the transmissivity section. Overall the increase is small though, registering at approximately one percent over the 50 freeze-thaw cycles for each set of specimens.

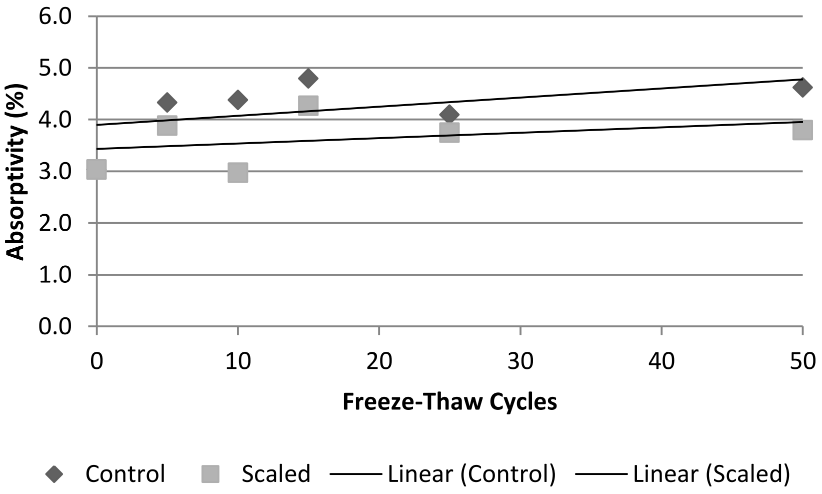

Figure 6-16: Acrylic absorptivity results

6.4.2 Glass Results and Analysis

The average results for transmission and reflection for the glass samples are shown in Table 6-12 along with the calculated absorption coefficient and the calculated RSD values for each parameter.

Table 6-12: Glass optical testing results

Property	Condition	Value	Freeze-Thaw Cycles					
			0	5	10	15	25	50
Transmissivity	Control	**Average**	**79.30**	**79.84**	**80.30**	**80.56**	**79.87**	**79.71**
		RSD (%)	0.98	1.16	1.15	0.07	0.67	2.12
	Scaled	**Average**	**79.30**	**80.57**	**80.28**	**80.12**	**78.81**	**79.98**
		RSD (%)	0.98	1.11	1.12	0.58	0.83	1.18
Reflectivity	Control	**Average**	**7.68**	**7.77**	**7.72**	**7.82**	**7.70**	**7.65**
		RSD (%)	1.33	0.55	0.55	2.87	0.33	0.23
	Scaled	**Average**	**7.68**	**7.70**	**7.66**	**7.73**	**7.66**	**7.69**
		RSD (%)	1.33	0.79	0.48	0.36	0.20	0.75
Absorptivity	Control	**Average**	**13.02**	**12.39**	**11.98**	**11.62**	**12.43**	**12.65**
		RSD (%)	6.17	7.68	7.78	2.06	4.11	13.48
	Scaled	**Average**	**13.02**	**11.73**	**12.06**	**12.14**	**13.53**	**12.33**
		RSD (%)	6.17	7.22	7.19	3.70	4.88	7.71

The overall results are similar to those found for the acrylic samples; the test values are relatively consistent across the range of testing and the RSD values are all low except for the absorptivity measurements where compounding errors are present.

Table 6-13 shows the results of a two variable ANOVA study on the transmissivity, reflectivity, and absorptivity properties of the glass samples. This study found that there were no significant correlations between conditioning method or freeze-thaw cycling and any optical property of the material. This is due to the overall consistent response of the optical properties during testing.

Table 6-13: Glass optical ANOVA results

Property	Variable	F-crit.	F-calc.	P-Value	Null Hypothesis	Statistical Significance
Transmissivity	Conditioning	6.61	0.11	0.750	Failed	Same
	Freeze-Thaw	5.05	2.35	0.185	Failed	Same
Reflectivity	Conditioning	6.61	3.21	0.133	Failed	Same
	Freeze-Thaw	5.05	3.23	0.112	Failed	Same
Absorptivity	Conditioning	6.61	0.22	0.658	Failed	Same
	Freeze-Thaw	5.05	2.57	0.161	Failed	Same

Figure 6-17 demonstrates the profile obtained from the transmissivity testing. Both the normal and scaled specimen sets produced relatively flat regression fits across the 50 cycles, though the scaled set saw slightly greater variability.

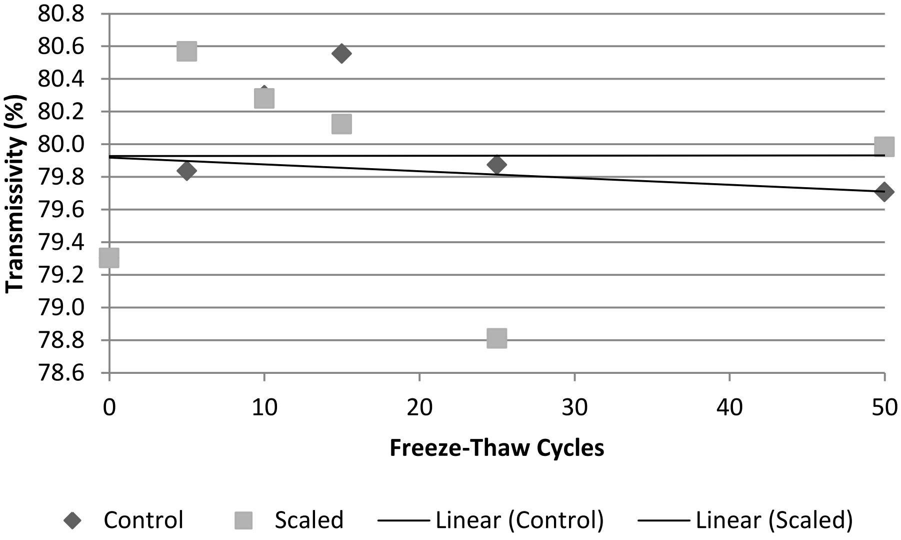

Figure 6-17: Glass transmissivity results

Figure 6-18 shows the reflectivity results from the glass samples. The scaled specimens produced an almost perfectly flat curve fit while the control set of data shows a decrease, but by only 0.08% across the 50 cycles. This demonstrates that in both cases the control and scaled average values are a good representation of each set of data.

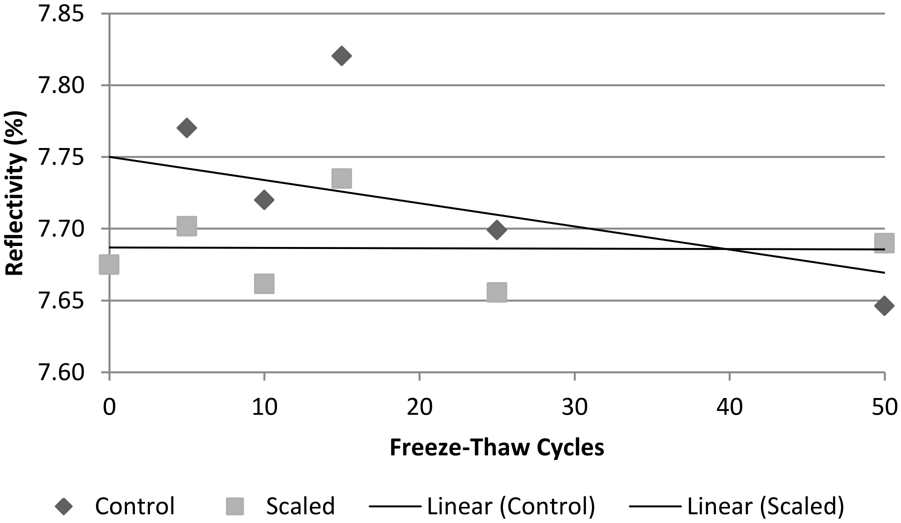

Figure 6-18: Glass reflectivity results

Figure 6-19 shows the profiles that were obtained from determining the absorptivity of the glass specimens. While this graph shows the scaled samples as more absorptive, the previous ANOVA analysis determined that there is statistically no impact from the conditioning method.

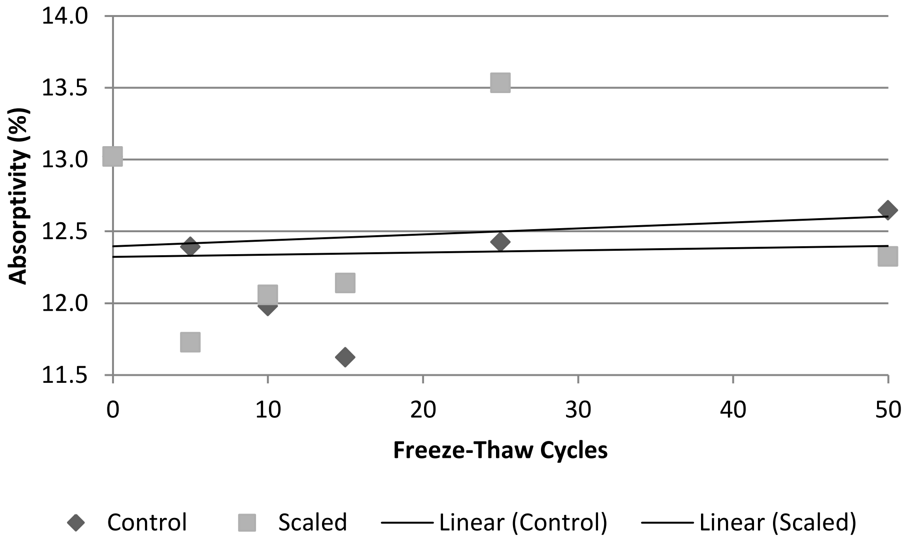

Figure 6-19: Glass absorptivity data

6.4.3 Polycarbonate Results and Analysis

The average results for transmission and reflection for the glass samples are shown in Table 6-14 along with the calculated absorption coefficient and the calculated RSD values for each parameter.

Table 6-14: Polycarbonate optical testing results

Property	Condition	Value	Freeze-Thaw Cycles					
			0	**5**	**10**	**15**	**25**	**50**
Transmissivity	Control	**Average**	**81.32**	**82.03**	**82.53**	**82.49**	**81.69**	**80.32**
		RSD (%)	0.60	0.76	0.20	0.59	0.73	3.88
	Scaled	**Average**	**81.32**	**82.68**	**82.23**	**82.83**	**82.26**	**81.81**
		RSD (%)	0.60	0.34	0.60	0.08	0.35	1.35
Reflectivity	Control	**Average**	**8.70**	**8.56**	**8.48**	**8.86**	**8.69**	**8.72**
		RSD (%)	1.96	4.09	5.04	2.60	2.59	0.28
	Scaled	**Average**	**8.70**	**8.78**	**8.74**	**8.89**	**8.85**	**8.76**
		RSD (%)	1.96	2.90	1.96	2.58	3.27	3.19
Absorptivity	Control	**Average**	**9.98**	**9.41**	**8.98**	**8.66**	**9.61**	**10.96**
		RSD (%)	3.80	9.66	6.27	3.11	7.94	28.64
	Scaled	**Average**	**9.98**	**8.54**	**9.03**	**8.28**	**8.90**	**9.44**
		RSD (%)	3.80	1.78	3.86	2.97	6.37	9.50

Like the acrylic and glass specimen sets before it, the polycarbonate samples demonstrate consistent test results and low RSD values.

Table 6-15 shows the results of a two variable ANOVA study on the transmissivity, reflectivity, and absorptivity properties of the glass samples. This study found that the only significant effect is of conditioning on the reflectivity data, but the effect of conditioning on absorptivity and the freeze-thaw cycling on both transmissivity and absorptivity come close to being significant.

Table 6-15: Polycarbonate optical ANOVA results

Property	Variable	F-crit.	F-calc.	P-Value	Null Hypothesis	Statistical Significance
Transmissivity	Conditioning	6.61	3.26	0.131	Failed	Same
	Freeze-Thaw	5.05	4.27	0.069	Failed	Same
Reflectivity	Conditioning	6.61	7.09	0.045	Passed	Different
	Freeze-Thaw	5.05	2.82	0.140	Failed	Same
Absorptivity	Conditioning	6.61	5.60	0.064	Failed	Same
	Freeze-Thaw	5.05	4.90	0.053	Failed	Same

Figure 6-20 shows the results from the transmissivity testing on the polycarbonate specimens. This data shows the same fluctuation that the three point bending results did in Figure 6-8, where the transmissivity increases by a substantial margin at first before dropping off with repeated freeze-thaw cycles. This is also believed to be caused by a realignment of the polymer chains in the material.

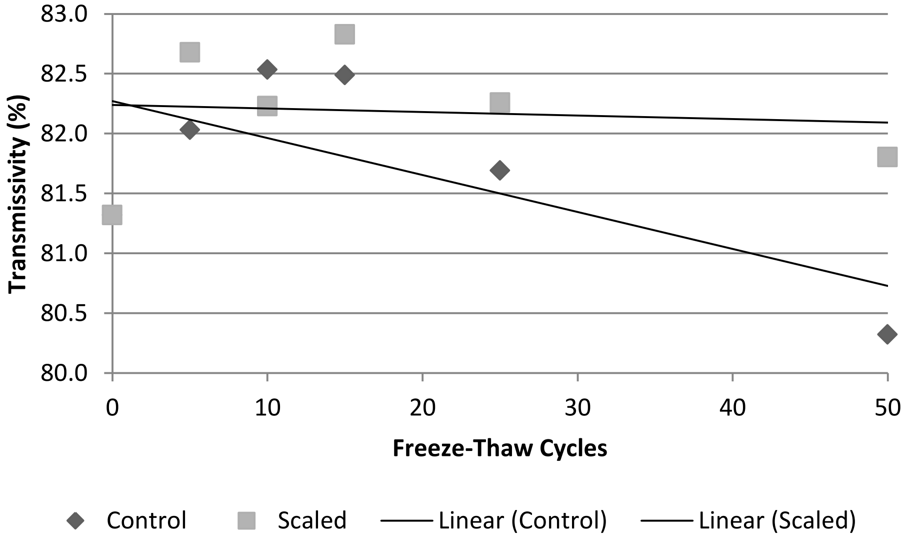

Figure 6-20: Polycarbonate transmissivity results

As noted from the ANOVA analysis, there is little difference between the two conditioning methods until the 50th cycle, causing the lack of statistical difference between these data sets. It is clear though that there is a trend occurring across different freeze-thaw cycles, however the relative plateau of results between 5 and 15 cycles causes the evaluation to fall just outside of statistical significance.

Figure 6-21 shows the results of the reflectivity testing, and demonstrates that there is a clear difference between the two conditioning methods. The normal samples show an overall lower reflectivity than that of the scaled samples, which is likely connected to a combination of the polymer chain realignment and the slightly greater impact of the salt brine on the surface microtexture. This trend was also noted on the friction results from the polycarbonate samples, as noted in Figure 6-13.

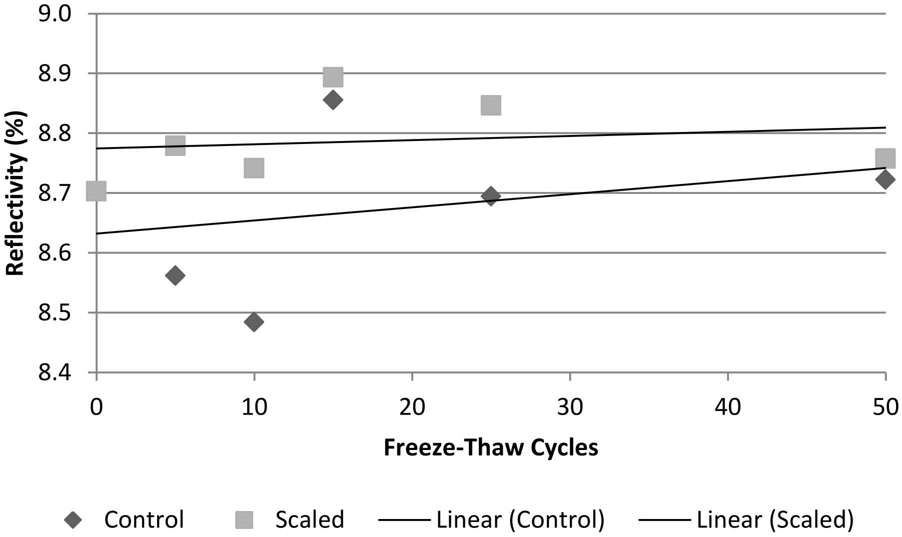

Figure 6-21: Polycarbonate reflectivity results

Figure 6-22 demonstrates the absorptivity of the polycarbonate samples and note the difference between the two conditioning methods and the freeze-thaw cycling. The scaled set of samples is less affected overall than the control ones, though these differences are due to the summation of measurement errors.

6.4.4 Material Comparison

Figure 6-23 shows the comparison between the transmissivity values of the normal and scaled samples from the optical testing. From this chart it is apparent that the optical grade acrylic acquired has the highest overall transmissivity while the polycarbonate samples had the lowest and the glass samples were, overall, slightly higher than the polycarbonate results. The transmissivity is the most important factor in determining the efficiency of the total solar road panel efficiency, as a higher value means more incident radiation on the panel will reach the solar cells, making acrylic the best option from this perspective.

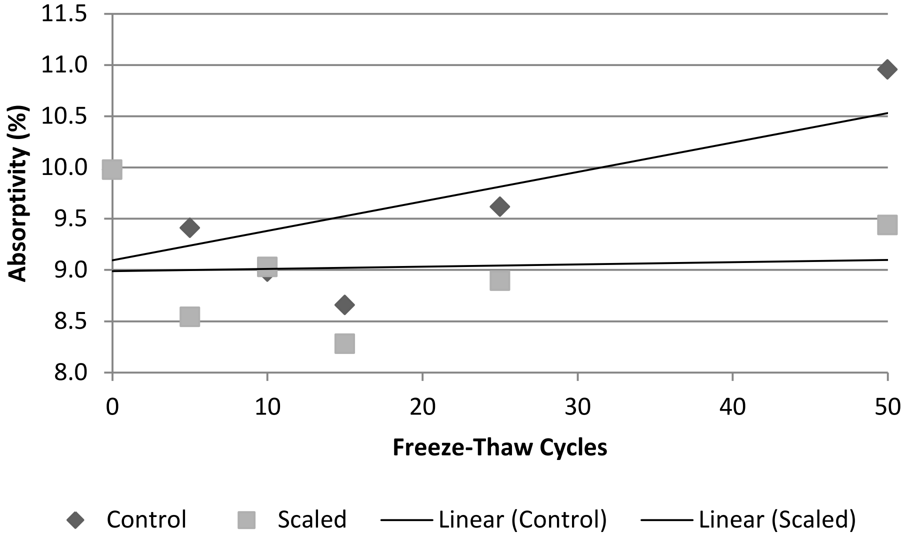

Figure 6-22: Polycarbonate absorptivity results

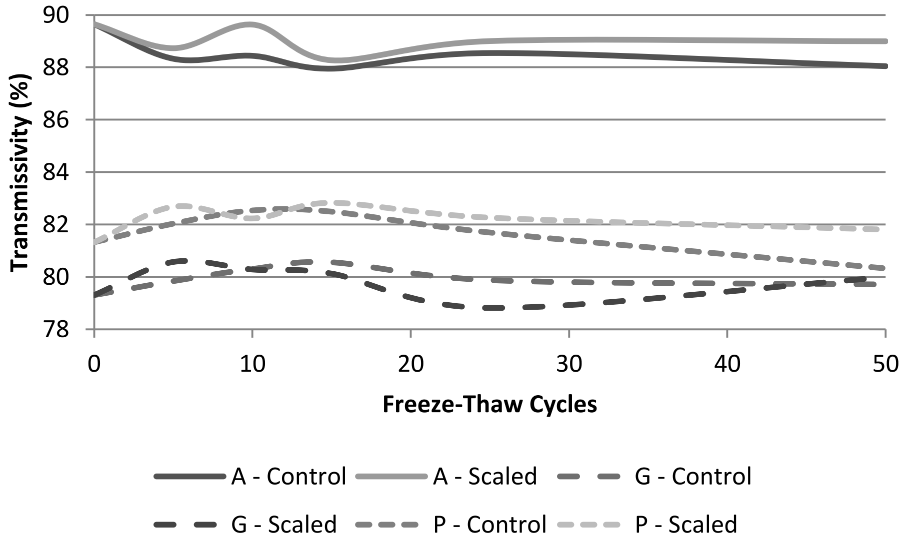

Figure 6-23: Average transmissivity comparison

Figure 6-24 shows the comparison between the average reflectivity values of the specimens used in the optical testing. From this chart it is apparent that the polycarbonate specimens have the highest reflectivity, followed by the glass specimens, and the acrylic specimens have the lowest. In terms of transportation engineering reflectivity is a very important safety property; roads that are too reflective produce glare that can distract drivers and cause accidents. From this perspective both the acrylic and glass materials provide good options in comparison to polycarbonate.

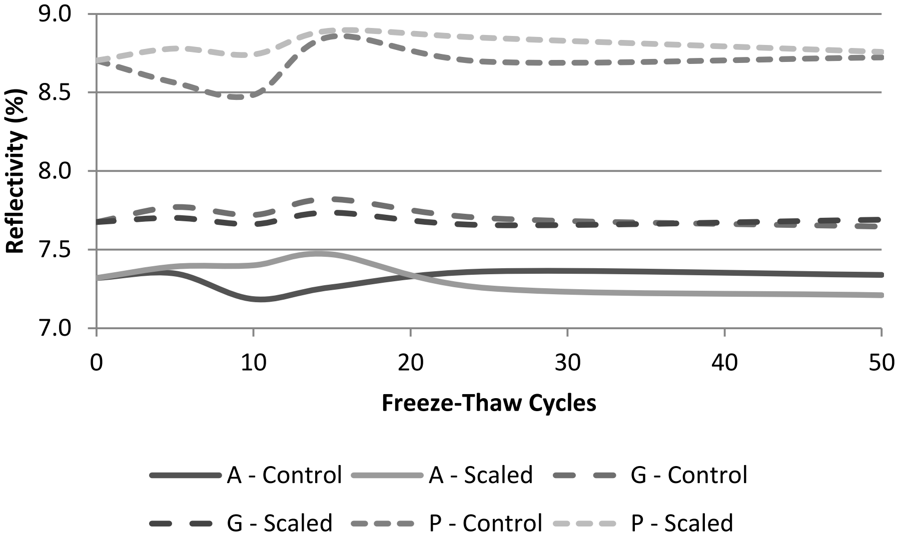

Figure 6-24: Average reflectivity comparison

Finally, Figure 6-25 shows the average calculated values for absorptivity of the materials used in the environmental testing. Here it is clear that the glass specimens are the most absorptive, followed by the polycarbonate samples, and that the acrylic samples are far less absorptive. The energy absorbed by these materials is going to correspond directly to the temperature of the optical layer of a solar road panel, so lower values are more ideal. That being said, the structural layer beneath the optical layer will be absorbing far more radiation and will heat the optical layer through conduction. The benefit of choosing a material with low absorptivity should be studied further.

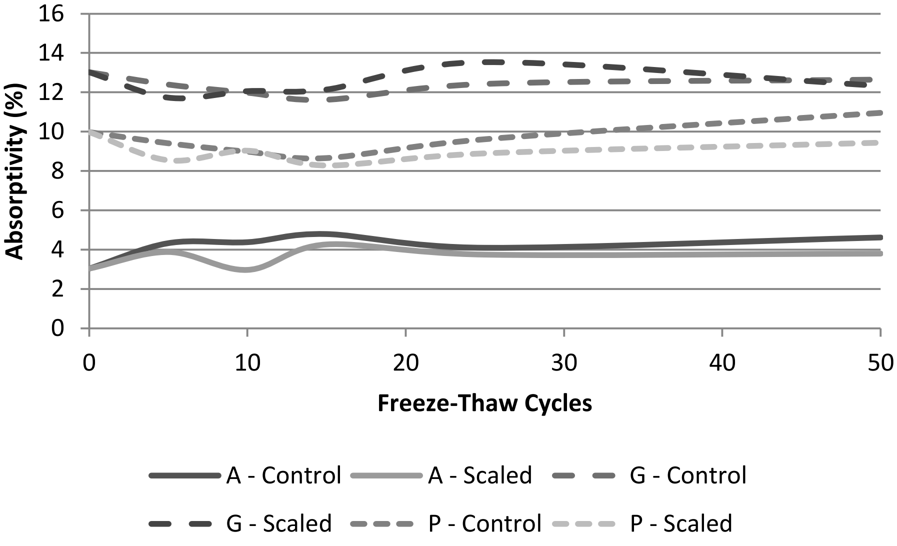

Figure 6-25: Average absorptivity comparison

6.5 Summary of Key Findings

The main finding of the environmental testing is that scaling has a very minimal impact on the performance of acrylic, polycarbonate, and glass. This was an expected result as both polymer should be inert to sodium chloride solutions while glass only corrodes in naturally acidic or basic solutions. Despite this minimal impact it was found that the performance of glass never varied with scaling, acrylic did in terms of reflectivity, and polycarbonate did for reflectivity and flexural modulus.

Freeze thaw cycling was observed to have a much bigger impact on the performance of these materials. In every case friction increased as a result of freeze-thaw cycling, the flexural modulus of polycarbonate increased, and the transmissivity of acrylic decreased. Again glass proved to be the most inert to the conditioning.

As a result, it was found that a properly designed glass surface would make for the best possible transparent layer of a solar road panel.

Chapter 7

Conclusions and Recommendations

7.1 Conclusions

Overall, this research proved the hypothesis and completed the objectives outlined; it is possible to build a solar road panel that can withstand the structural and environmental loads that Ontario pavements are subjected to. It was also found that the prototype designed for this research meets all of these criteria with no adjustments.

7.1.1 Design of a Solar Road Panel

It was found that the optimal starting point for a solar road panel was to build the panels with a two 10-mm tempered glass pane transparent layer supported by a 12.7-mm GPO-3 optical layer and a 19.1-mm base layer of the same material.

This combination of material places the emphasis for the rigidity of the panel on the transparent layer. Other configurations, with different transparent layer materials, would likely need rigid structural layers in order to minimize the strains that the solar cells are subjected to. These other configurations would also suffer from rutting issues similar to those of asphalt pavements, though the rutting would occur over the solar cell compartments. This would likely greatly increase the roughness of pavements, damage vehicles, and increase the susceptibility of the surface to hydroplaning.

7.1.2 Applicability of Solar Road Panels in Ontario

7.1.2.1 Structural Considerations

Given typical materials and structural designs, solar road panels can definitely have a place within Ontario's pavement infrastructure. This research demonstrated that with an adequately designed asphalt or concrete base, these panels can improve the life of our pavement structures as the stresses from vehicle traffic are distributed further through the panel before they are applied to the base underneath.

The prototype designed for this research demonstrated an infinite design life under both fatigue and static load conditions, which indicates that optimizations can be made to reduce the volume of material needed in each panel and this will directly lower the cost of the structures. This is especially true when a concrete structural base is considered, as the threshold stresses for failure of the concrete are also far from being reached from these load conditions.

It was also found that this panel was safely designed to ensure that the solar cells will not fail due to strain cycling. This finding clears one of the main concerns of the traditional solar module industry, which is highly focused on the strain induced microcracking of solar cells due to the flexural performance of their encapsulating solar module. Especially in the cases with concrete or asphalt bases there is room for design optimization before the strain fatigue criteria would be met.

7.1.2.2 Environmental Considerations

This research showed that the typical salting methods applied to roads in Ontario for deicing will not have a negative impact on the performance of the driving surface of a solar road panel. Acrylic and polycarbonate both showed occasional effects from salt brine application, however the glass specimens proved to be inert through all of the testing making it the ideal material choice for this application.

Greater impacts were found from the freeze-thaw cycling of the materials. In particular it was found that this conditioning increased the friction available on the surface of all of the specimens in a linear fashion over the 50-cycles of testing. This would be a major benefit to solar road panels as these transparent surfaces have very poor friction characteristics without textures and coatings, so improvements that can be gained through normal operation are highly beneficial.

Overall it was found that glass proved to be the best transparent material to deal with the environmental conditions subjected to Ontario’s pavement infrastructure. It’s inertness to the environmental conditioning found in this study confirmed the prototype design decision made to use this material for its structural benefits over acrylic and polycarbonate.

7.2 Recommendations

The recommendations consist of two main categories; future research that continues the work outlined in this thesis and additional areas of study in order to make solar road panels a viable product.

7.2.1 Future Research

First and foremost, work should be completed towards the design optimization of solar road panels and their structural bases. This research showed that the current solar road panel and concrete pavement base structure is heavily overdesigned. Performing an optimization of this with a heavy focus on costs would help make a more sustainable case for solar road panels.

Structural testing of solar road panel prototypes should be expanded to include in-situ testing. If frictional issues cannot be resolved easily this could be mitigated by testing the panels in a single wheel path, allowing traction to be supplied by all of the wheels not loading the panel. This testing would allow for better analysis of fatigue effects on the edges in the optical layer and validate the work shown here in the fatigue and static simulations in general.

Work should be conducted on the wet and dry friction characteristics of coated and uncoated glass surfaces. It is highly likely that in order to develop enough friction for safe travel on a tempered glass surface that both macro- and micro-textural improvements will be required; these are developed through surface texturing and surface coating. Different types of high-impact resistant glasses should also be examined for their applicability to this research.

The pavement load case analysis performed in this research should be updated to include the viscoelastic characteristics of asphalt and granular materials as structural bases. It is likely that the deterioration of these layers over time will increase the stresses seen in the solar road panel and, as a result, will decrease the design life of the panel.

7.2.2 Additional Areas of Study for Solar Road Panels

Research should be conducted on the types of solar cells that are best situated for installing in a solar road panel. This research prototype was designed considering monocrystalline silicon photovoltaic cells, however due to the expected characteristics of the light reaching the solar cells this may be a better application for solar cells which are better at diffuse light capturing.

The research suggested above on the frictional characteristics of textured and coated glasses should also include an optimization for the optical properties of the panel as a whole. The texturing and coating have the potential to increase the reflectivity of the surface, but also the air pocket between the glass and the solar cell encapsulant should be considered to determine what the net electricity generation of these panels could be.

Research should also be done on the costs of solar road panels and their related infrastructure, with a focus on the return of investment from installing the infrastructure. Aspects of this should include panel design, structural base design, associated grid connecting hardware, and revenue from selling the electricity or offsetting buying electricity from the grid.

References

AASHTO. (1993). *AASHTO guide for design of pavement structures.* (). Washington, DC: AASHTO.

Abaqus. (2013). *Abaqus CAE 6.13 documentation* Dassault Systems.

ACI. (2013). Matweb material property data. Retrieved May 13, 2013, from http://www.matweb.com/index.aspx

Adams, W. M. (2006). *The future of sustainability: Re-thinking environment and development in the twenty-first century.* ().IUCN.

Agro, S., & Tucker, R. (2004). *Development of new low-cost, high-performance, PV module encapsulant/packaging materials: Annual technical progress report.* (No. SR-520-35683). Golden: NREL.

Alagusundaramoorthy, P., Harik, I. E., & Choo, C. C. (2006). Structural behavior of FRP composite bridge deck panels. *Journal of Bridge Engineering, July/August*, 384.

Alsop, D. J. A., & Saunders, R. J. (1999). *Structural use of glass in buildings*. London: Institute of Structural Engineers.

ARA. (2011). *Methodology for the development of equivalent pavement structural design matrix for municipal roadways.* (No. 000830). Toronto, Ontario: RMCAO.

ASCE. (2013). Orthotropic bridge. Retrieved September, 5, 2013, from http://www.orthotropic-bridge.org/

Askeland, D., & Phule, P. (2006). *The science and engineering of materials* (5th ed.). Toronto: Thomson.

ASTM. (2009). *Standard test method for determining solar or photopic reflectance, transmittance, and absorptance of materials using a large diameter integrating sphere.* (No. ASTM E1175-87).American Society for Testing and Materials.

ASTM. (2010). *Standard test methods for flexural properties of unreinforced and reinforced plastics and electrical insulating materials.* (No. ASTM D790-10).American Society for Testing and Materials.

ASTM. (2012a). *Sandard test method for solar absorptance, reflectance, and transmittance of materials using integrating spheres.* (No. ASTM E903-12).American Society for Testing and Materials.

ASTM. (2012b). *Standard test method for scaling resistance evaluation of concrete surfaces exposed to deicing chemicals.* (No. ASTM C672-12).American Society for Testing and Materials.

ASTM. (2013). *Standard test methods for total normal emittance of surfaces using inspection-meter techniques.* (No. ASTM E408-13).American Society for Testing and Materials.

Bergamin, L., & Sammaraee, T. (2010). Waved glass: Towards optimal light distribution on solar cell surfaces for high efficient modules. *Solar Energy, 84*(1), 90-100.

Bijsterveld, W. T. e. a. (2001). Using pavement as solar collector: Effect on pavement temperature and structural response. *Transportation Research Record: Journal of the Transportation Research Board, 1778*, 140.

Budynas, R. G., & Nisbett, J. K. (2008). *Shigley's mechanical engineering design* (8th ed.). New York: McGraw Hill.

Caliendo, C., & Parisi, A. (2010). Stress-prediction model for airport pavements with jointed concrete slabs. *Journal of Transportation Engineering, July*, 664.

Cho, Y. H., McCullough, B. F., & Weissmann, J. (1996). Considerations on finite-element method application in pavement structural analysis. *Transportation Research Record: Journal of the Transportation Research Board, 1539*, 96.

Chung, K., Chang, K., & Liu, Y. (2008). Reduction of wind uplift of a solar collector model. *Journal of Wind Engineering and Industrial Aerodynamics, 96*(8), 1294-1306.

Costello, S. B., Bargh, L. S., Henning, T. F. P., & Hendry, M. (2013). Proposed new performance indicator - vehicle operation cost index (VOCi) due to road roughness. *Transportation Research Board 92nd Annual Meeting,* Washington, D.C.

CSA. (2006). *Canadian highway bridge deisgn code.* ().CSA International.

Demers, C. E. (1998). Fatigue strength degradation of E-glass FRP composites and carbon FRP composites. *Construction and Building Materials, 12*(1998), 311.

Deubener, J., Helsch, G., Moiseev, A., & Bornhöft, H. (2009). Glasses for solar energy conversion systems. *Journal of the European Ceramic Society, 29*(7), 1203-1210.

El Amrani, A., Mahrane, A., Moussa, F., & Boukennous, Y. (2007). Solar module fabrication. *International Journal of Photoenergy, 2007*

El-Hakim, M. Y. (2009). *Instrumentation and overall evaluation of perpetual and conventional flexible pavement designs.* (Masters of Applied Science, University of Waterloo).

Enfiinty. (2011). Europe's first "green" train leaves the station thanks to Belgium's solar tunnel. Retrieved July 5, 2012, from http://www.enfinitycorp.com/downloads/news-releases/europes-first-green-train

Environment Canada. (2013). *Canadian climate normals 1971-2000: Waterloo wellington airport*. Ottawa: Environment Canada.

FAUN. (2012). *FAUN TRACKWAY brochure*. Llangefni, UK: FAUN Trackway.

Foster, D., & Anderson, M. (2003). Rapid forward deployment made easier with composite airfield matting. *AMPTIAC Quarterly, 7*(1), 17-22.

Grand Canyon National Park. (2013). Grand canyon sky walk. Retrieved August 1, 2013, from http://www.grandcanyon-nationalpark.org/grand-canyon-skywalk/

Greene, J., Toros, U., Kim, S., Byron, T., & Choubane, B. (2010). Impact of wide-base single tires on pavement damage. *Transportation Research Record: Journal of the Transportation Research Board, 2155*, 82.

Holley Jr, W., Agro, S., Galica, J., & Yorgensen, R. (1996). UV stability and module testing of nonbrowning experimental PV encapsulants. *Photovoltaic Specialists Conference, 1996., Conference Record of the Twenty Fifth IEEE,* 1259-1262.

Hsieh, H. H., Lin, F. M., & Yu, S. P. (2011). Performance of low series-resistance interconnections on the polycrystalline solar cells. *Solar Energy Materials and Solar Cells, 95*(1), 39-44.

Huang, Y. H. (2004). *Pavement analysis and design* (2nd ed.). New Jersey: Pearson Prentice Hall.

IEA. (2011). *IEA statistics: CO_2 emissions from fuel combustion: 2011 edition.* (). Paris: International Energy Agency.

ISG. (2013). ISG glass flooring system details. Retrieved September, 5, 2013, from http://www.structuralglass.com/eledet/ISG-GF-A.pdf

Jorgensen, G., Terwilliger, K., DelCueto, J., Glick, S., Kempe, M., Pankow, J., . . . McMahon, T. (2006). Moisture transport, adhesion, and corrosion protection of PV module packaging materials. *Solar Energy Materials and Solar Cells, 90*(16), 2739-2775.

Kempe, M. D., & Thapa, P. (2008). Low-cost single-layer replacement for the back-sheet and encapsulant layers. *Society of Photo-Optical Instrumentation Engineers (SPIE) Conference Series, , 7048* 12.

KNMI. (2013). *Long term average 1981-2010 - average yearly precipitation*. De Bilt: Royal Netherlands Meteorological Institute.

Lange, R. F. M., Luo, Y., Polo, R., & Zahnd, J. (2011). The lamination of (multi) crystalline and thin film based photovoltaic modules. *Progress in Photovoltaics: Research and Applications, 19*(2), 127-133.

Luque, A., & Hegedus, S. (2003). *Handbook of photovoltaic science and engineering*. Chichester: Wiley.

Mak, T. L. A. (2012). *Modular road plate system.* (Master of Applied Science, University of Waterloo).

MTO. (1990). *Pavement design and rehabilitation manual*. Toronto: Ontario Ministry of Transportation.

MTO. (2012). *Ontario's default parameters for AASHTOWare pavement ME design interim report.* (). Toronto: Ontario Ministry of Transportation.

Neamen, D. A. (2003). *Semiconductor physics and devices: Basic principles* (3rd ed.). New York: McGraw-Hill.

Northmore, A., & Tighe, S. (2012a). Developing innovative roads using solar technologies. *CSCE 9th International Transportatoin Specialty Conference,* Edmonton.

Northmore, A., & Tighe, S. (2012b). Innovative pavement design: Are solar roads feasible? *2012 Conference of the Transportation Association of Canada,* Fredericton.

NRC. (2012). Photovoltaic potential and solar resouce maps of canada. Retrieved February 8, 2013, from http://pv.nrcan.gc.ca/

Ooms. (2013). SolaRoad. Retrieved February 13, 2013, from http://www.ooms.nl/nl/1/480/solaroad.aspx

OPSS. (2003). *Material specification for aggregates - base, subbase, select subgrade, and backfill material.* (No. OPSS 1010). Toronto: Ontario Provincial Standard Specification.

Perkins, S. W. (1999). *Geosynthetic REinforcement of flexible pavements: Laboratory based pavement test sections.* (No. FHWA/MT-99-001/8138). Helena: Montana DoT.

Perret-Aebi, L. E., Li, H. -., Chapuis, V. & Heinstein, P. (2011). PV module design. Retrieved May 30, 2012, from http://pvlab.epfl.ch/pv_module_design

Pokharel, S. K., Han, J., Manandhar, C., Yang, X., Leshchinsky, D., Halahmi, I., & Parsons, R. L. (2011). Accelerated pavement testing of geocell-reinforced unpaved roads over weak subgrade. *Transportation Research Record: Journal of the Transportation Research Board, 2204*, 67-75.

Ritchie, R. O. (2003). Feilure of silicon: Crack formation and propogation. *13th Workshop on Crystalline Solar Cell Materials and Processes,* Vail, Colorado.

RMSolar. (2012). Mono 125S0R2 solar cell. Retrieved March 14, 2012, from http://www.rmsolarpanel.com/html/49/2010-12-13/content-34.html

Roark, R. J., & Young, W. C. (1975). *Formulas for stress and strain* (5th ed.). New York: McGraw-Hill.

Robinson, M. C. (2005). Landing mat development at WES. In B. M. Fowle (Ed.), *Builders and fighters* (pp. 195-206) University Press of the Pacific.

Rochling. (2013). *Grade UTR Arc/Track & flame resistant laminate.* (). Cleveland: Rochling Glastic Composites.

Rollings, R. S. (1975). *Comparison of the british class 60 trackway and AM-2 mat for bomb damage repair applications.* (No. AFWL-TR-75-149). Washington, D.C.: NTIS.

Rose, D., Jester, T., & Bunea, G. (2008). Automated manufacturing of high efficiency modules.

Rushing, T. S., & Tingle, J. S. (2009). Full-scale evaluation of mat surfacings for roads over sand subgrades. *Journal of Terramechanics, 46*(2009), 57-63.

Sánchez-Illescas, P., Carpena, P., Bernaola-Galván, P., Sidrach-de-Cardona, M., Coronado, A., & Álvarez, J. (2008). An analysis of geometrical shapes for PV module glass encapsulation. *Solar Energy Materials and Solar Cells, 92*(3), 323-331.

Skoplaki, E., & Palyvos, J. (2009). On the temperature dependence of photovoltaic module electrical performance: A review of efficiency/power correlations. *Solar Energy, 83*(5), 614-624.

Solar Roadways. (2013). Solar roadways - A real solution. Retrieved February 13, 2013, from http://solarroadways.com/main.html

Statistics Canada. (2012). *Electric power generation, by class of electricity producer, annual (megawatt hour).* (No. Table 127-0007).Statistics Canada.

TAC. (2012). *Pavement asset design and management guide*. Ottawa: Transportation Association of Canada.

Tingle, J. S., & Jersey, S. R. (2005). Cyclic plate load TEsting of geosynthetic-reinforced unbound aggregate roads. *Transportation Research Record: Journal of the Transportation Research Board, 1936*, 60-69.

TNO. (2013). SolaRoad combines road and solar cells. Retrieved February 13, 2013, from http://www.tno.nl/content.cfm?context=thema&content=inno_case&laag1=895&laag2=912&item_id=1234

Torontoist. (2013). Doors closed. Retrieved August 1, 2013, from http://torontoist.com/attachments/toronto_vald/20090522-cntower.jpg

Transport Canada. (2008). *Transportation in canada 2007: An overview.* (No. TP 14816E). Ottawa: Transport Canada.

Ulery, H. H., & Wolf, D. P. (1971). *Thickness requirements for soils beneath landing mats; bare base support.* (No. S-71-3). Washington, D.C.: NTIS.

US DoD. (1987). *Military specification (MIL)-M-52612A(ME); mats, landing, aluminum; medium duty XM19.* (). Washington, D.C.: U.S. Department of Defence.

US DoT. (2012). *Alternative uses of highway right-of-way: Accommodating renewable energy technologies and alternative fuel facilities.* (). Cambridge: U.S. Department of Transportation.

US EIA. (2011). *International energy outlook 2011.* (). Washington, D.C.: U.S. Energy Information Administration.

Walbridge, S., & de la Chevrotiere, A. (2012). *Opportunities for the use of aluminum in vehicular bridge construction.* (). Montreal: MAADI Group.

Webster, S. L., & Tingle, J. S. (1998). *Espedient road construction over sands using lightweight mats.* (No. N-1472). Washington, D.C.: NTIS.

World Commission on Environment and Development. (1987). *Our common future.* (). Oxford: Oxford University Press.

Wu, G., & Yu, X. (2012). Thermal energy harvesting across pavement structure. *Transportation Research Board 91st Annual Meeting,* Washington DC.

Wu, Z., Chen, X., & Yang, X. (2011). *Finite element simulation of structrual performance on flexible pavements with stabilized Base/Treated subbase materials under accelerated loading.* (No. FHWA/LA.10/452). Baton Rouge: LTRC.

Xia, K. (2010). A finite element model for Tire/Pavement interaction: Application to predicting pavement damage. *International Journal of Pavement Research and Technology, 3*(3), 135.

Appendix A

Solar Road Panel Prototype Design Drawings

PARTS LIST			
ITEM	QTY	PART NUMBER	DESCRIPTION
1-2-000	1	BASE FG LAYER - THICK	
1-3-000	2	OPTICAL FG LAYER	
1-4-000	1	GLASS ASSY	
1-1-000	1	BASE FG LAYER - THIN	
1-5-000	4	FRAME MEMBER	

DETAIL #	QTY
1-0-000	1

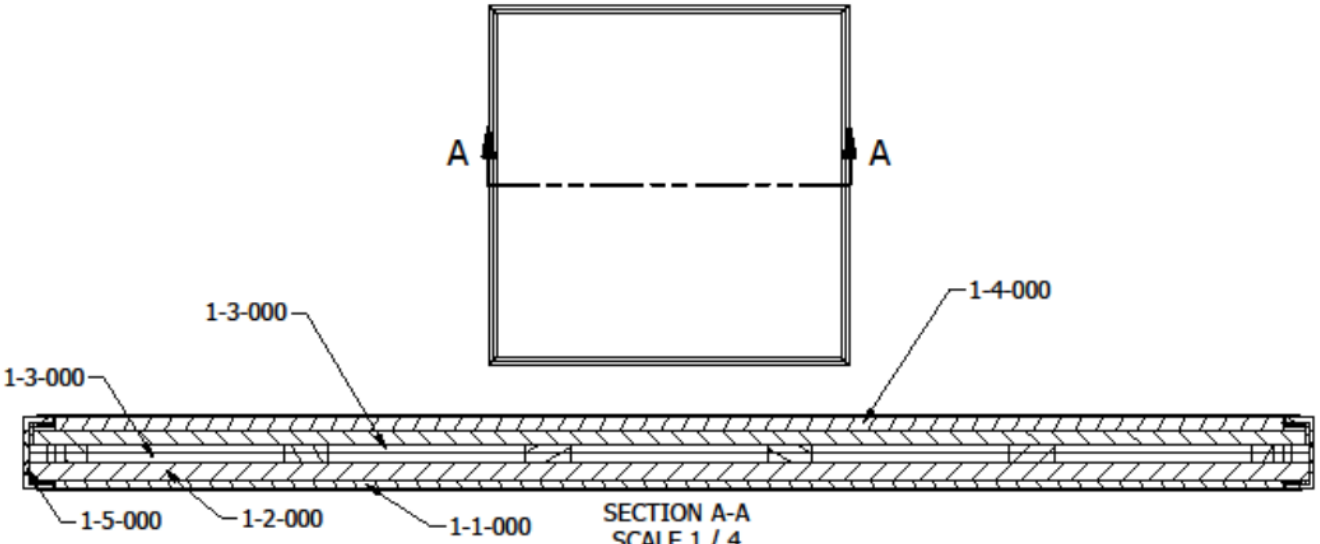

SECTION A-A
SCALE 1 / 4

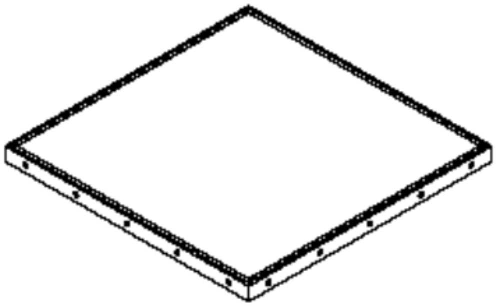

DRAWN A. NORTHMORE	11/29/2013	CPATT - UNIVERSITY OF WATERLOO		
CHECKED		TITLE PANEL ASSEMBLY		
QA				
MFG				
APPROVED				
		SIZE A	DWG NO 1-0-000	REV 4
		SCALE		SHEET 1 OF 1

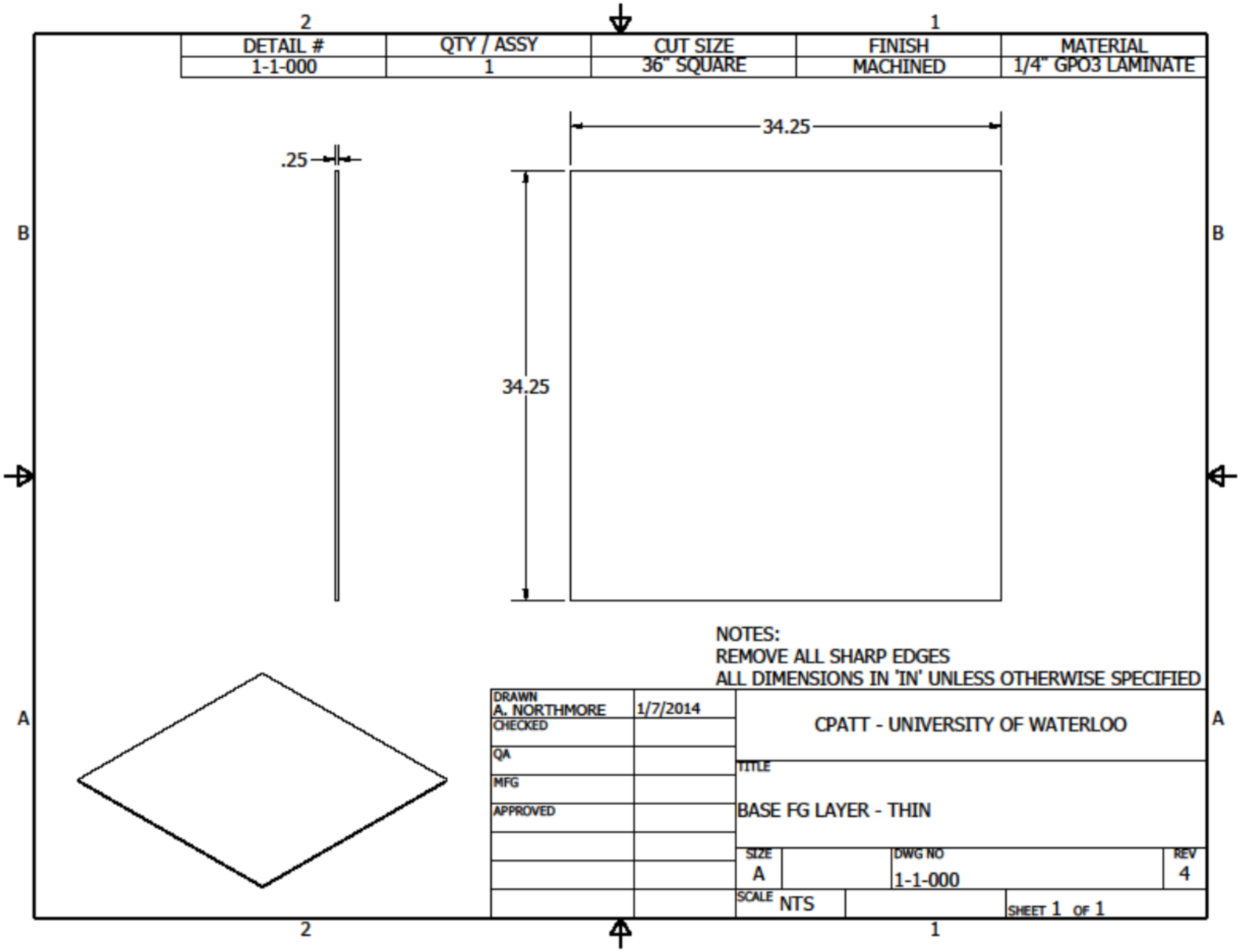

DETAIL #	QTY / ASSY	CUT SIZE	FINISH	MATERIAL
1-1-000	1	36" SQUARE	MACHINED	1/4" GPO3 LAMINATE

NOTES:
REMOVE ALL SHARP EDGES
ALL DIMENSIONS IN 'IN' UNLESS OTHERWISE SPECIFIED

DRAWN A. NORTHMORE	1/7/2014
CHECKED	
QA	
MFG	
APPROVED	

CPATT - UNIVERSITY OF WATERLOO

TITLE
BASE FG LAYER - THIN

SIZE	DWG NO	REV
A	1-1-000	4

SCALE NTS
SHEET 1 OF 1

DETAIL #	QTY / ASSY	CUT SIZE	FINISH	MATERIAL
1-2-000	1	36" SQUARE	MACHINED	1/2" GPO3 LAMINATE

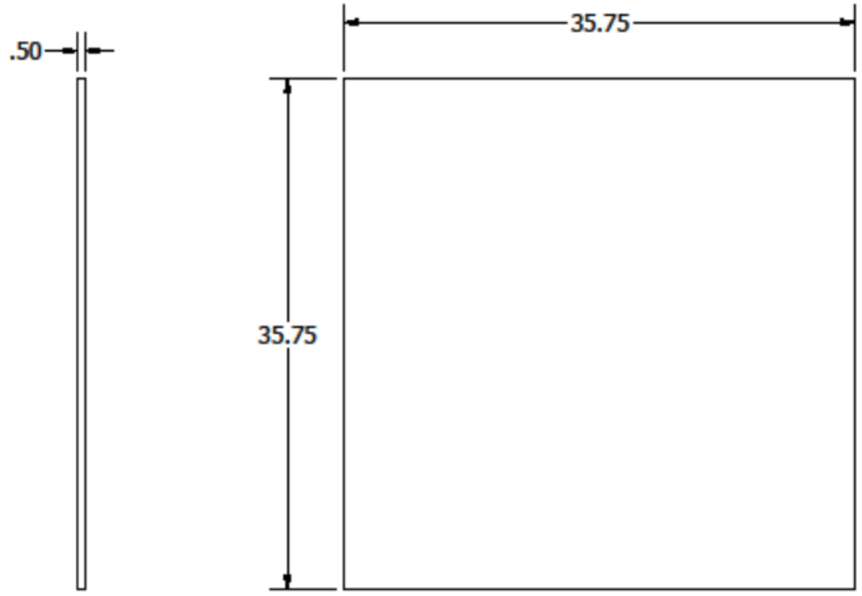

NOTES:
REMOVE ALL SHARP EDGES
ALL DIMENSIONS IN 'IN' UNLESS OTHERWISE SPECIFIED

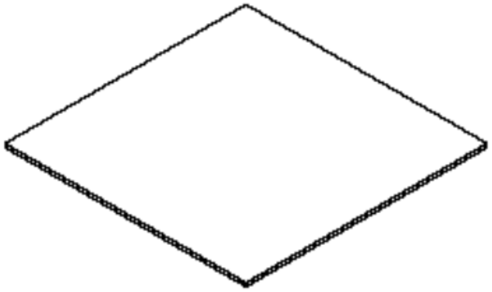

DRAWN A. NORTHMORE	1/7/2014	CPATT - UNIVERSITY OF WATERLOO			
CHECKED					
QA		TITLE			
MFG		BASE FG LAYER - THICK			
APPROVED					
		SIZE A		DWG NO 1-2-000	REV 4
		SCALE NTS		SHEET 1 OF 1	

PARTS LIST			
ITEM	QTY	PART NUMBER	DESCRIPTION
1-3-001	4	FG OPTICAL BAR 1	
1-3-002	4	FG OPTICAL BAR 2	
1-3-003	20	FG OPTICAL BAR 3	

DETAIL #	QTY
1-3-000	2

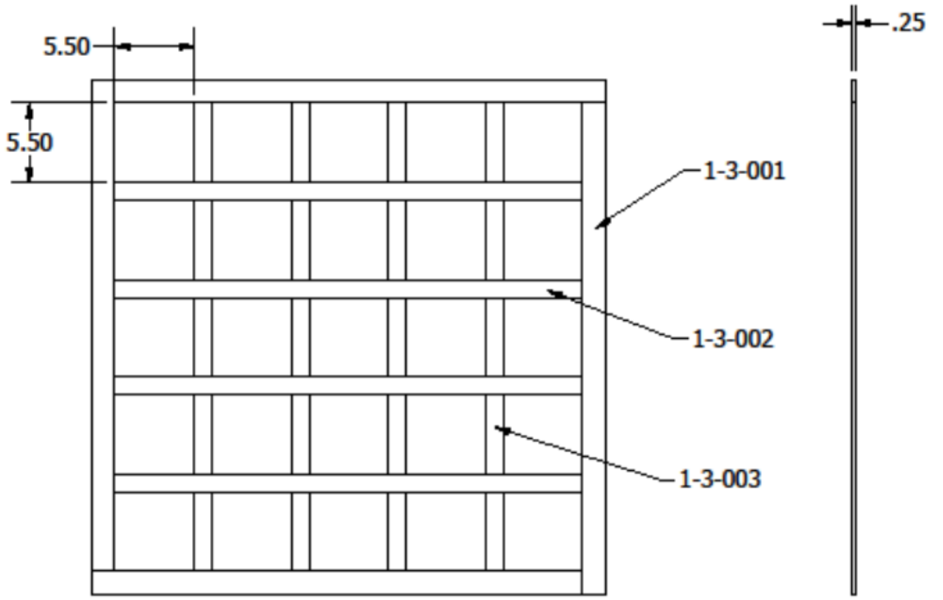

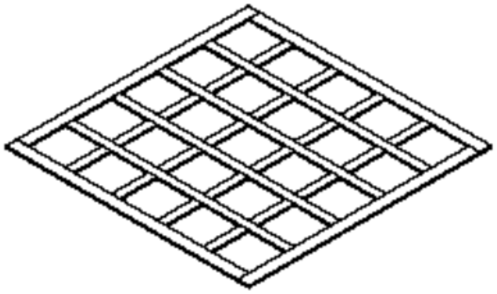

DRAWN A. NORTHMORE	1/7/2014
CHECKED	
QA	
MFG	
APPROVED	

CPATT - UNIVERISITY OF WATERLOO

TITLE

OPTICAL FG LAYER

SIZE A
DWG NO 1-3-000
REV 4
SCALE
SHEET 1 OF 1

DETAIL #	QTY / ASSY	CUT SIZE	FINISH	MATERIAL
1-3-001	4	36" X 1-5/8"	MACHINED	1/4" GPO3 LAMINATE

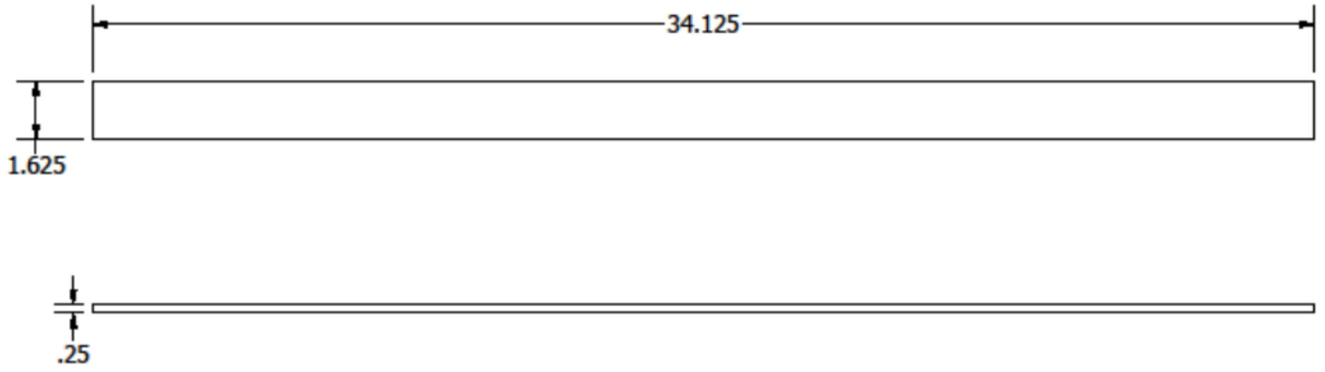

NOTES:
REMOVE ALL SHARP EDGES
ALL DIMENSIONS IN 'IN' UNLESS OTHERWISE SPECIFIED

DRAWN A. NORTHMORE	1/7/2014	CPATT - UNIVERSITY OF WATERLOO
CHECKED		
QA		TITLE
MFG		FG OPTICAL BAR 1
APPROVED		
		SIZE A · DWG NO 1-3-001 · REV 4
		SCALE NTS · SHEET 1 OF 1

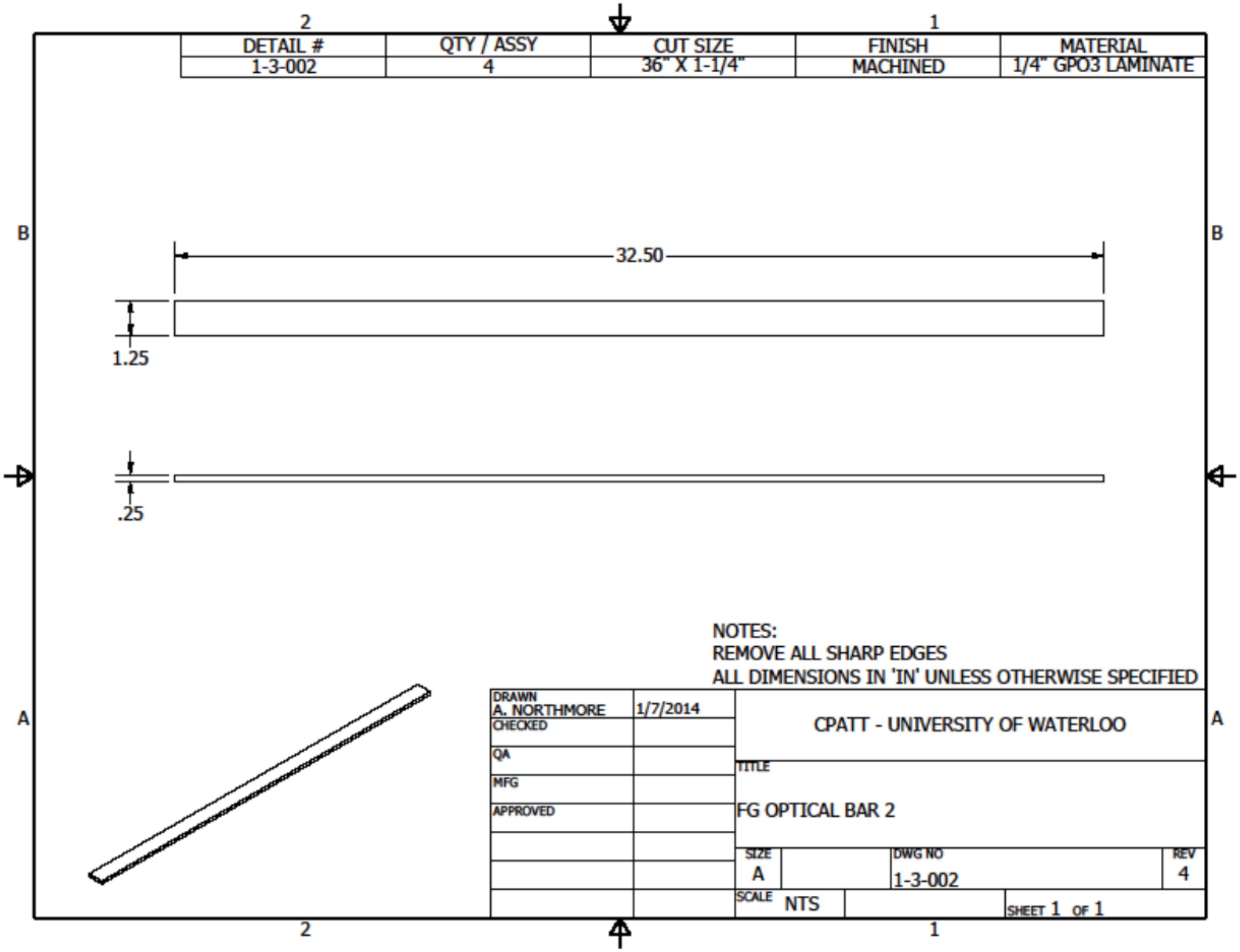

DETAIL #	QTY / ASSY	CUT SIZE	FINISH	MATERIAL
1-3-002	4	36" X 1-1/4"	MACHINED	1/4" GPO3 LAMINATE

NOTES:
REMOVE ALL SHARP EDGES
ALL DIMENSIONS IN 'IN' UNLESS OTHERWISE SPECIFIED

DRAWN A. NORTHMORE	1/7/2014
CHECKED	
QA	
MFG	
APPROVED	

CPATT - UNIVERSITY OF WATERLOO

TITLE
FG OPTICAL BAR 2

SIZE	DWG NO	REV
A	1-3-002	4

SCALE NTS
SHEET 1 OF 1

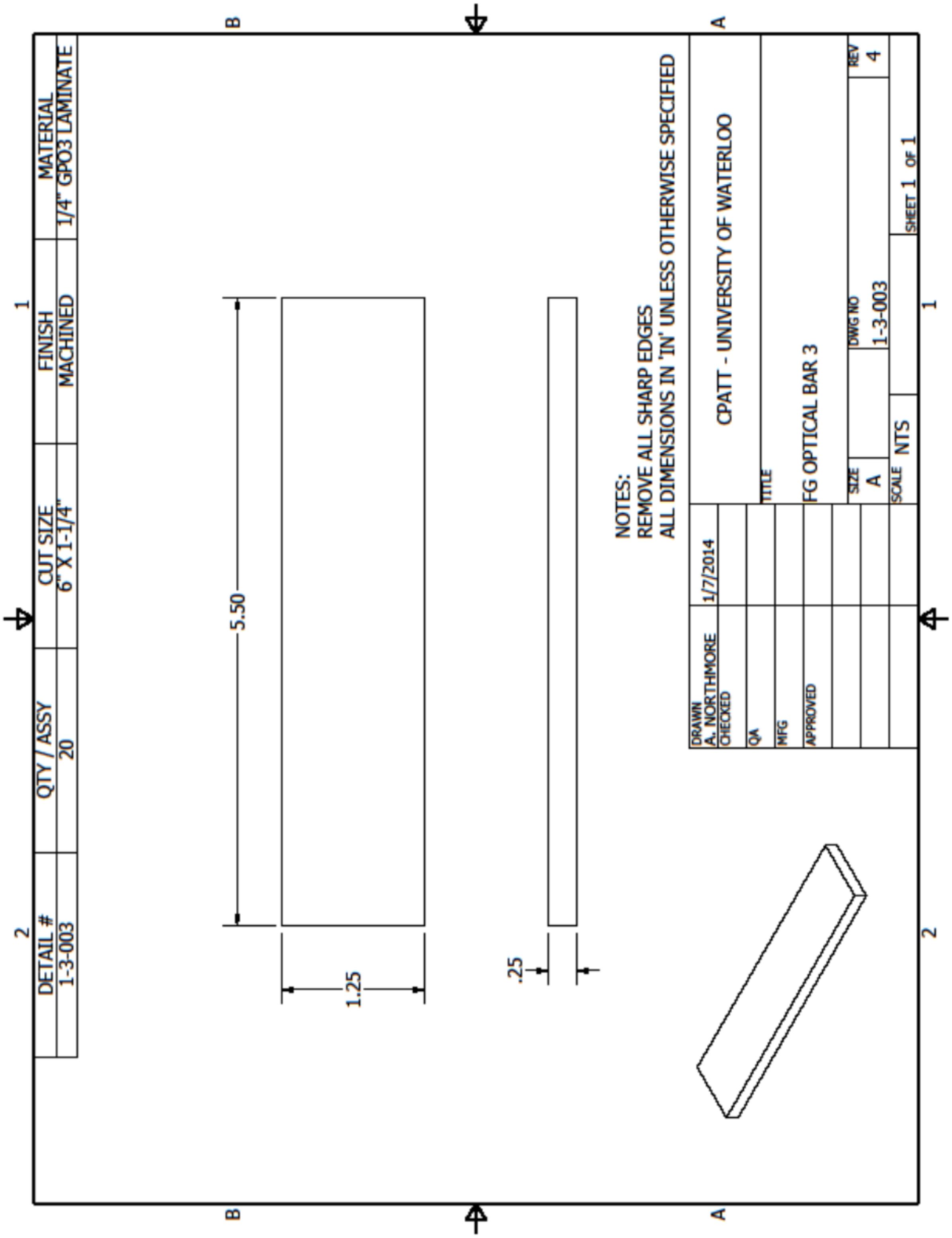
DETAIL #
1-3-003
QTY / ASSY
20
CUT SIZE
6" X 1-1/4"
FINISH
MACHINED
MATERIAL
1/4" GPO3 LAMINATE
5.50
1.25
.25
NOTES:
REMOVE ALL SHARP EDGES
ALL DIMENSIONS IN 'IN' UNLESS OTHERWISE SPECIFIED
CPATT - UNIVERSITY OF WATERLOO
DRAWN
A. NORTHMORE
1/7/2014
CHECKED
QA
MFG
APPROVED
TITLE
FG OPTICAL BAR 3
SIZE
A
DWG NO
1-3-003
REV
4
SCALE
NTS
SHEET 1 OF 1
A
B
1
2

DETAIL #	QTY / ASSY	FINISH	MATERIAL
1-4-000	1	TEMPERED AND LAMINATED	10-MM TEMPERED GLASS

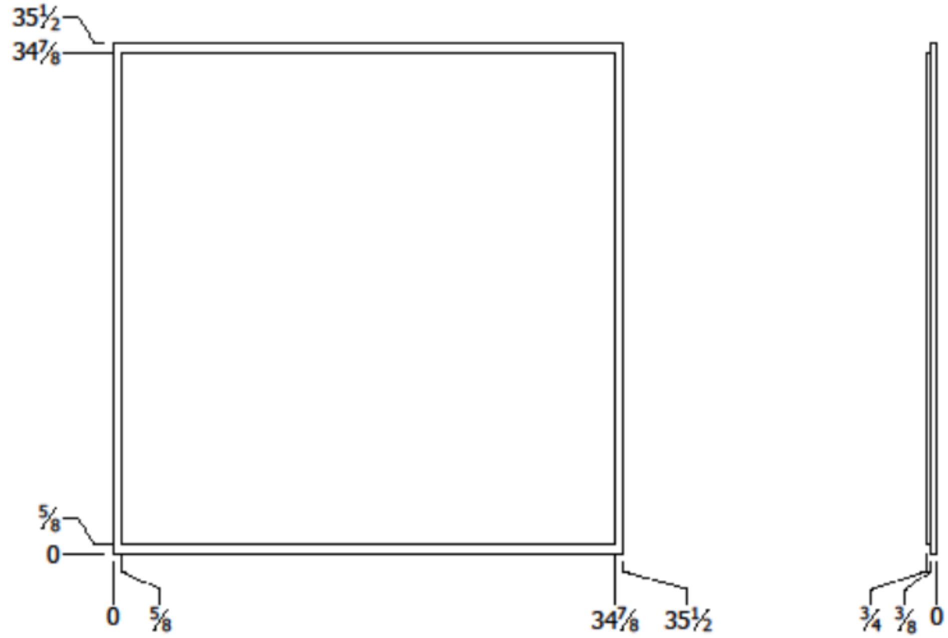

NOTES:
REMOVE ALL SHARP EDGES
ALL DIMENSIONS IN 'IN' UNLESS OTHERWISE SPECIFIED

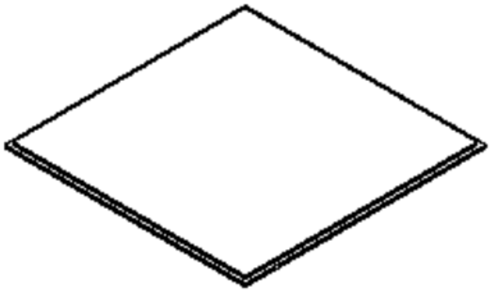

DRAWN A. NORTHMORE	1/7/2014	CPATT - UNIVERSITY OF WATERLOO			
CHECKED					
QA		TITLE			
MFG		GLASS ASSEMBLY			
APPROVED					
		SIZE A	DWG NO 1-4-000		REV 4
		SCALE NTS		SHEET 1 OF 1	

PARTS LIST			
ITEM	QTY	PART NUMBER	DESCRIPTION
1-5-001	1	FRAME CHANNEL	2" X 1/4" C-CHANNEL, 36" LENGTH
1-5-002	3	RUBBER SEAL	1/4" X 1/8" ADHESIVE BACKED RUBBER
1-5-003	2	EDGE SEAL	1/8" POLYETHELYNE EDGE TRIM

DETAIL #	QTY
1-5-000	1

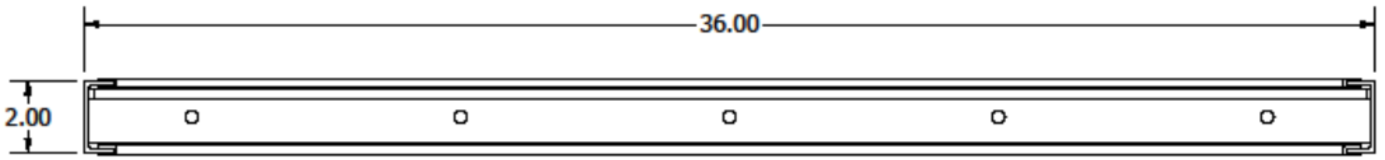

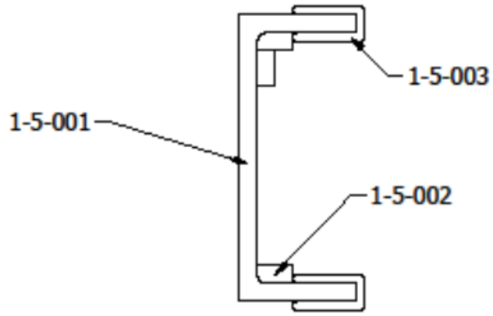

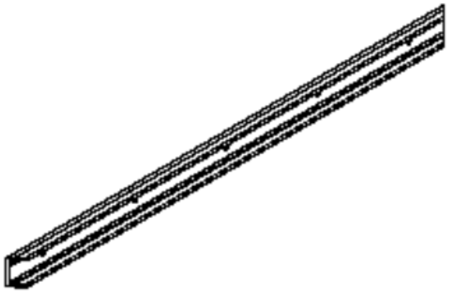

NOTES:
REMOVE ALL SHARP EDGES
ALL DIMENSIONS IN 'IN' UNLESS OTHERWISE SPECIFIED

DRAWN A. NORTHMORE	1/7/2014	CPATT - UNIVERSITY OF WATERLOO			
CHECKED					
QA		TITLE FRAME ASSEMBLY			
MFG					
APPROVED					
		SIZE A		DWG NO 1-5-000	REV 4
		SCALE	NTS		SHEET 1 OF 1

Appendix B

Solar Road Panel Prototype Bill of Materials

	Item	Supplier	Part Number	Unit	Qty Req	Pack Qty	Pack Cost	Panel Cost	Total Cost	Description
Structural	Fiberglass	McMaster-Carr	8549K86	Each	1	1	$203.87	$183.48	$203.87	Electrical-Grade Fiberglass (GP03) 1/4" Thick, 36" X 72"
	Fiberglass	McMaster-Carr	8549K88	Each	0.5	1	$313.14	$156.57	$313.14	Electrical-Grade Fiberglass (GP03) 1/2" Thick, 36" X 72"
	Aluminum Channel	Metal Supermarket	AC6063/2118	Inches	144	144	$ 45.99	$45.99	$45.99	2"x1"x0.125" 6063 T5 Channel
	Frame Nuts	McMaster-Carr	98694A110	Each	25	100	$ 5.90	$1.48	$5.90	1/4"-20 round top, zinc-plated Grade 5 steel nut
	Frame Bolts	McMaster-Carr	91263A562	Each	25	25	$ 8.05	$8.05	$8.05	1/4"-20 zinc-plated alloy steel flat socket head cap screw
	Weather Seal	McMaster-Carr	8645K35	Feet	36	15	$ 12.55	$30.12	$37.65	1/4"w x 1/8"t rubber seal, adhesive backed
	Edge Seal	McMaster-Carr	86875K141	Feet	36	100	$ 45.00	$16.20	$45.00	1/8" edge polyethelyne edge trim
	Epoxy	Canadian Tire	67-1406-2	Each	10	1	$ 8.49	$84.90	$84.90	LePage Epoxy Gel
	Glass Assembly	All-Brite Glass	N/A	Each	1	1	$ 661.00	$661.00	$661.00	2 layer, 20mm, laminated, textured glass assembly
Electrical	Solar Cells	Parallax	750-00043	Each	1	1	$39.99	$39.99	$39.99	6-pack of 125mm solar cells
	Solar Cells	Parallax	750-00044	Each	2	2	$79.99	$79.99	$79.99	13-pack of 125mm solar cells
	22G Black Wire	McMaster-Carr	7587K921	Feet	50	1	$ 0.09	$4.66	$4.66	22 Gauge black wire
	22G Red Wire	McMaster-Carr	7587K922	Feet	50	1	$ 0.09	$4.66	$4.66	22 Gauge red wire
	12G Black Wire	McMaster-Carr	7587K212	Feet	25	1	$ 0.56	$13.91	$13.91	12 Gauge black wire
	12G Red Wire	McMaster-Carr	7587K226	Feet	25	1	$ 0.56	$13.91	$13.91	12 Gauge red wire
	Heat-Shrink Tubing	McMaster-Carr	7132K6	Feet	25	25	$ 16.25	$16.25	$16.25	25' roll of 1/16" final OD heat shrink
	Barrier Strip	Digi-Key	WM5805-ND	Each	1	1	$ 6.80	$6.80	$6.80	4 terminal barrier strip
	Barrier Diode	Digi-Key	SB540-E3/54GICT-ND	Each	1	1	$ 0.79	$0.79	$0.79	5A, 40V schottky barrier diode
	Barrier Box	Digi-Key	377-1178-ND	Each	1	1	$ 2.16	$2.16	$2.16	3"x2"x1.5" housing box
	Barrier Box Lid	Digi-Key	377-1184-ND	Each	1	1	$ 0.90	$0.90	$0.90	box cover for 377-1178-ND
	Wire Solder	Digi-Key	473-1125-ND	Each	1	1	$ 20.08	$20.08	$20.08	1/2 lb of 22 GA rosin core wire solder
	Encapsulant	Everbright Solar	06103	Each	1	1	$ 49.95	$49.95	$49.95	SYLGARD 184 encapsulation kit
	Interconnect	Everbright Solar	05110	Each	1	1	$ 12.95	$12.95	$12.95	80' tabbing wire w/ solder
	Totals							$1,454.77	$1,672.48	

Appendix C

Structural Testing Frame Design Drawings

PARTS LIST			
ITEM	QTY	PART NUMBER	DESCRIPTION
1-1-000	1	BASE ASSEMBLY	
1-2-000	4	LEG ASSEMBLY	
1-3-000	1	BASE PLATE HOLE PATTERN	

DETAIL #	QTY
1-0-000	1

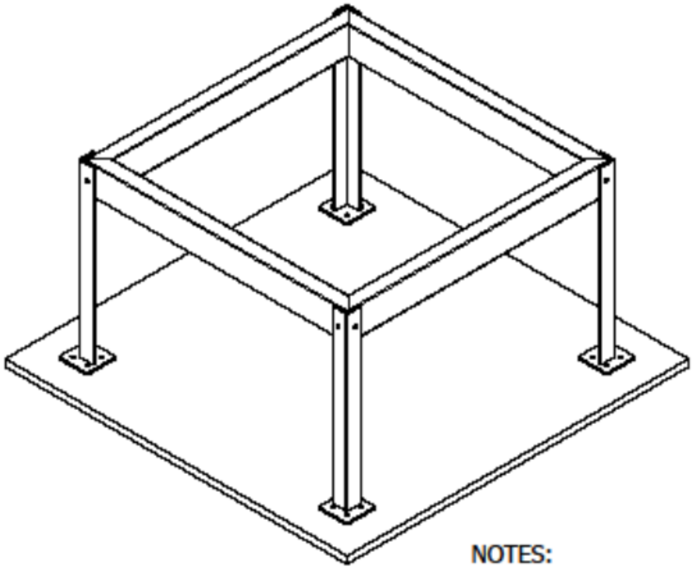

NOTES:
REMOVE ALL SHARP EDGES
ALL DIMENSIONS IN 'IN' UNLESS OTHERWISE SPECIFIED

DRAWN A. NORTHMORE	8/15/2013	CPATT - UNIVERSITY OF WATERLOO
CHECKED		
QA		TITLE
MFG		TESTING FRAME ASSEMBLY
APPROVED		
		SIZE A · DWG NO 1-0-000 · REV 0
		SCALE · SHEET 1 OF 1

PARTS LIST			
ITEM	QTY	PART NUMBER	DESCRIPTION
1-1-001	4	BASE TUBE	

DETAIL #	QTY
1-1-000	1

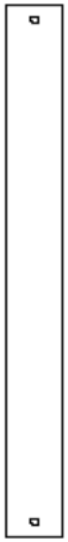

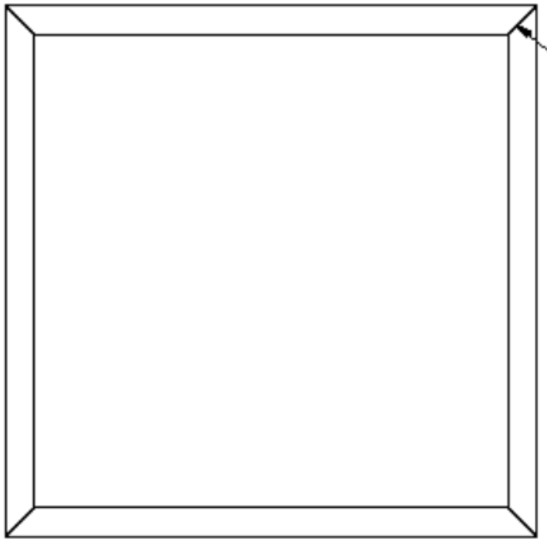

CONNECTIONS TO BE WELDED
WELD PARAMETERS TBD

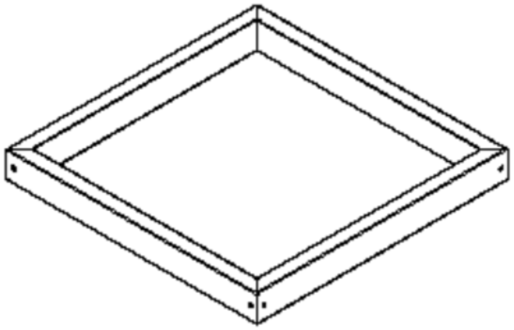

NOTES:
REMOVE ALL SHARP EDGES
ALL DIMENSIONS IN 'IN' UNLESS OTHERWISE SPECIFIED

DRAWN A. NORTHMORE	8/15/2013	CPATT - UNIVERSITY OF WATERLOO			
CHECKED		TITLE LOAD RING ASSEMBLY			
QA					
MFG					
APPROVED					
		SIZE A	DWG NO 1-1-000		REV 0
		SCALE NTS		SHEET 1 OF 1	

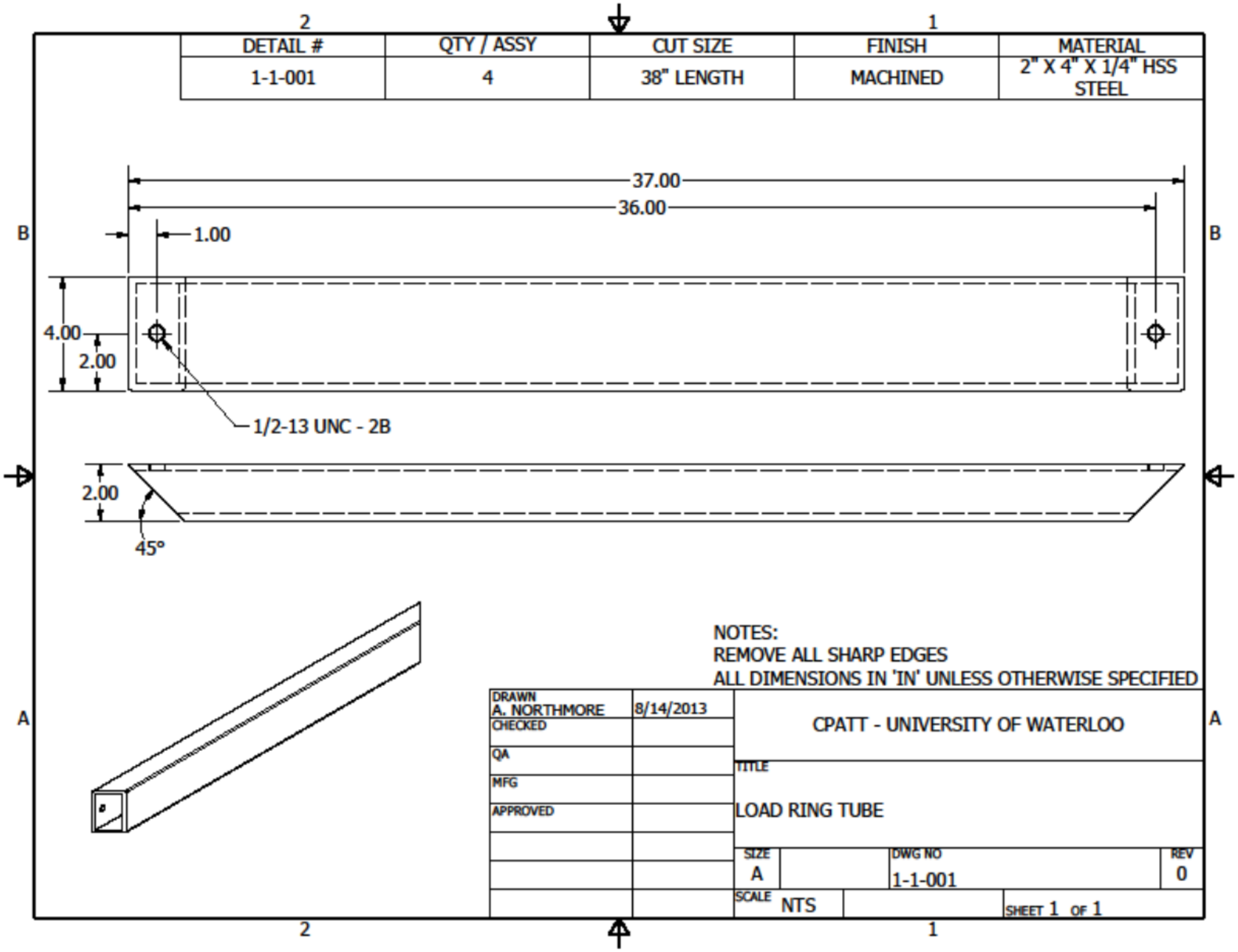

DETAIL #	QTY / ASSY	CUT SIZE	FINISH	MATERIAL
1-1-001	4	38" LENGTH	MACHINED	2" X 4" X 1/4" HSS STEEL

NOTES:
REMOVE ALL SHARP EDGES
ALL DIMENSIONS IN 'IN' UNLESS OTHERWISE SPECIFIED

PARTS LIST			
ITEM	QTY	PART NUMBER	DESCRIPTION
1-2-001	1	LEG ANGLE	
1-2-002	1	LEG FOOTING	

DETAIL #	QTY
1-2-000	4

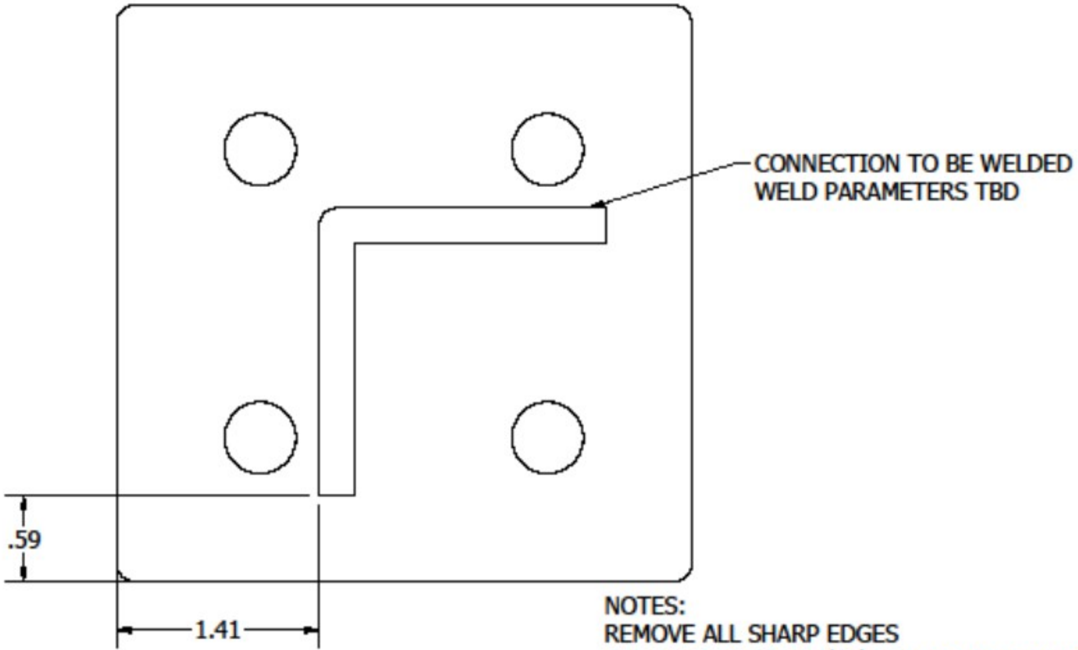

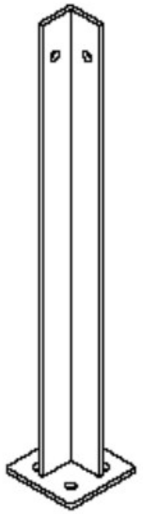

NOTES:
REMOVE ALL SHARP EDGES
ALL DIMENSIONS IN 'IN' UNLESS OTHERWISE SPECIFIED

DRAWN A. NORTHMORE	8/15/2013	CPATT - UNIVERSITY OF WATERLOO
CHECKED		
QA		TITLE
MFG		
APPROVED		LEG ASSEMBLY
		SIZE A · DWG NO 1-2-000 · REV 0
		SCALE NTS · SHEET 1 OF 1

DETAIL #	QTY / ASSY	CUT SIZE	FINISH	MATERIAL
1-2-001	1 (16 TOT)	24" LENGTH	MACHINED	2" X 2" X 1/4" STEEL ANGLE

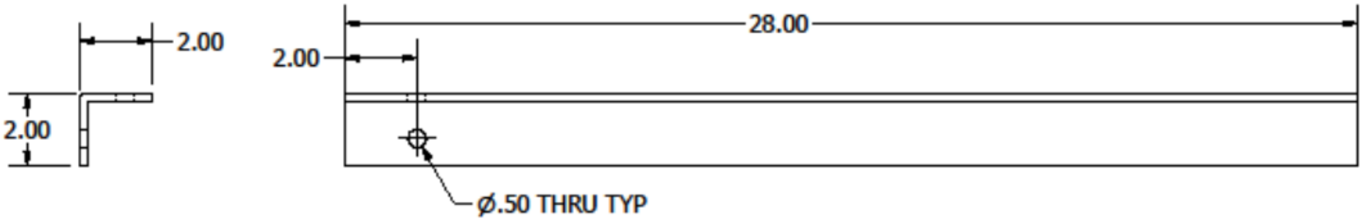

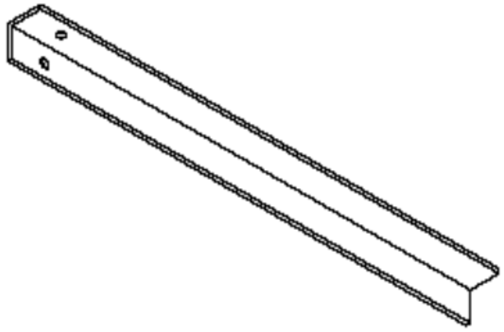

NOTES:
REMOVE ALL SHARP EDGES
ALL DIMENSIONS IN 'IN' UNLESS OTHERWISE SPECIFIED

DRAWN A. NORTHMORE	8/14/2013	CPATT - UNIVERSITY OF WATERLOO			
CHECKED					
QA		TITLE			
MFG		LEG ANGLE			
APPROVED					
		SIZE A		DWG NO 1-2-001	REV 0
		SCALE NTS		SHEET 1 OF 1	

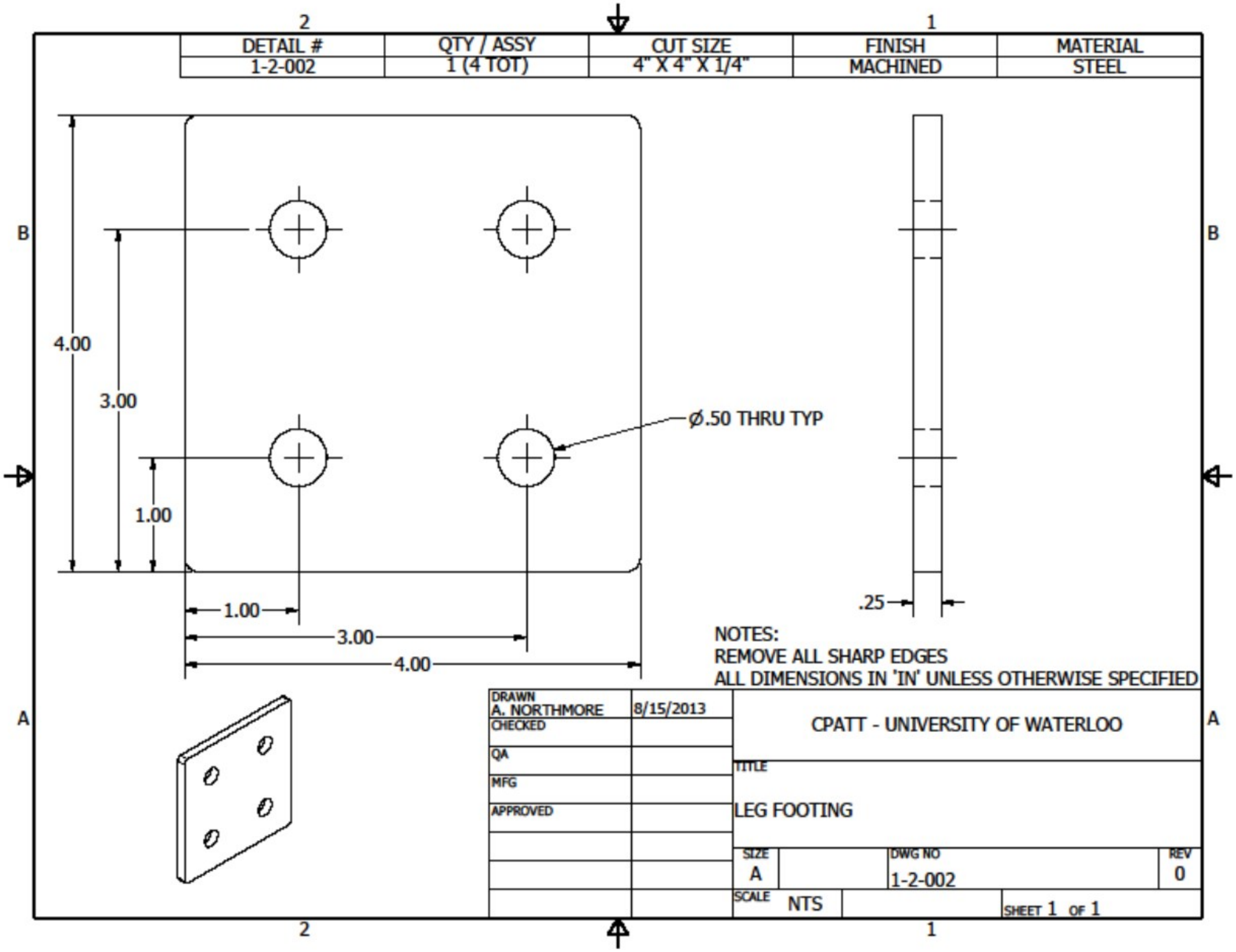

DETAIL #	QTY / ASSY	CUT SIZE	FINISH	MATERIAL
1-2-002	1 (4 TOT)	4" X 4" X 1/4"	MACHINED	STEEL

NOTES:
REMOVE ALL SHARP EDGES
ALL DIMENSIONS IN 'IN' UNLESS OTHERWISE SPECIFIED

DRAWN A. NORTHMORE	8/15/2013
CHECKED	
QA	
MFG	
APPROVED	

CPATT - UNIVERSITY OF WATERLOO

TITLE
LEG FOOTING

SIZE A
DWG NO 1-2-002
REV 0
SCALE NTS
SHEET 1 OF 1

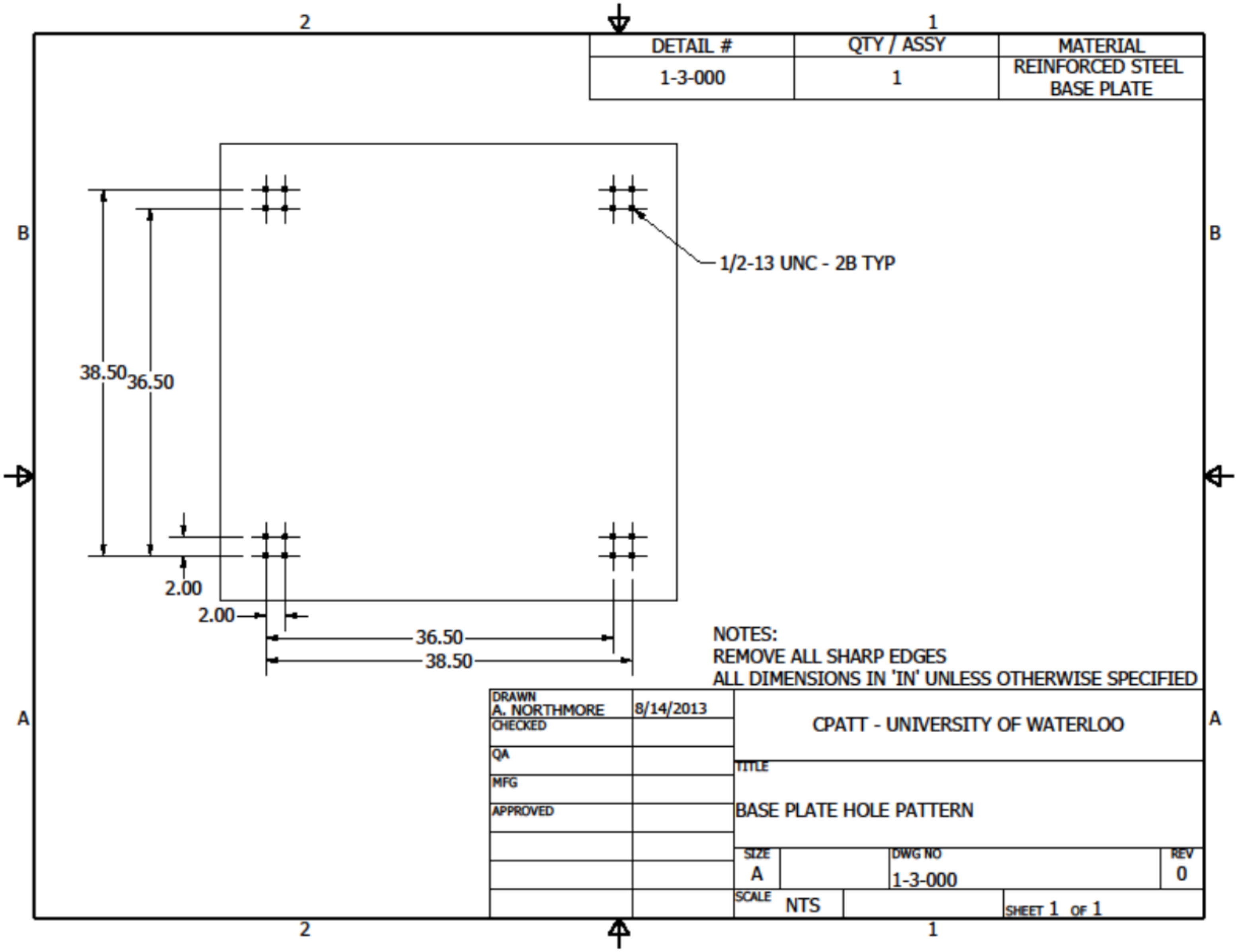

DETAIL #	QTY / ASSY	MATERIAL
1-3-000	1	REINFORCED STEEL BASE PLATE

NOTES:
REMOVE ALL SHARP EDGES
ALL DIMENSIONS IN 'IN' UNLESS OTHERWISE SPECIFIED

DRAWN A. NORTHMORE	8/14/2013
CHECKED	
QA	
MFG	
APPROVED	

CPATT - UNIVERSITY OF WATERLOO

TITLE
BASE PLATE HOLE PATTERN

SIZE	DWG NO	REV
A	1-3-000	0

SCALE NTS
SHEET 1 OF 1

Appendix D

Three-Point Bending Apparatus Fixture Drawings

DETAIL #	QTY / ASSY	CUT SIZE	FINISH	MATERIAL
1-001	1	1 3/8" D X 3 1/4" LG	MACHINED	STRUCTURAL STEEL - COLD ROLLED

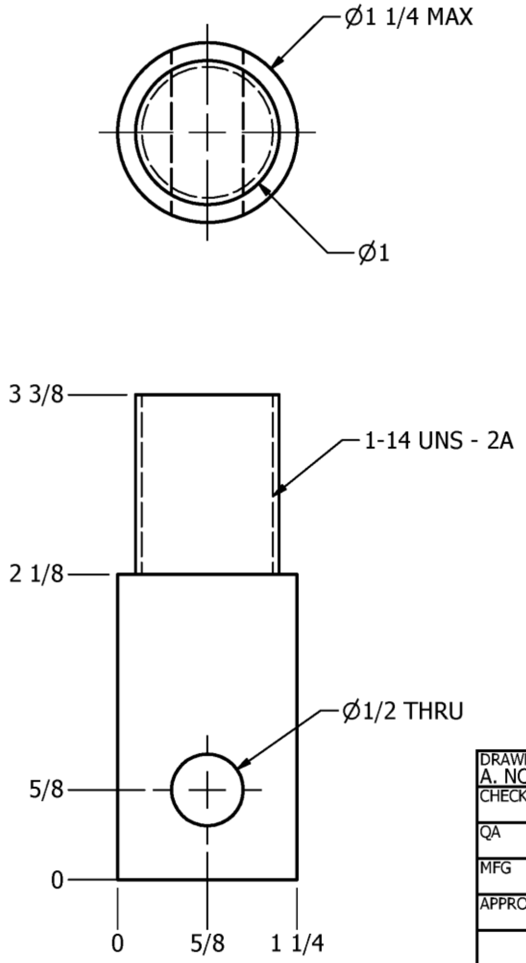

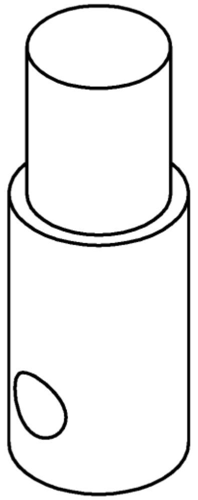

NOTES:
REMOVE ALL SHARP EDGES
ALL DIMENSIONS IN 'IN' UNLESS OTHERWISE SPECIFIED

DRAWN A. NORTHMORE	6/13/2013	CPATT - UNIVERSITY OF WATERLOO
CHECKED		
QA		TITLE
MFG		BASE COLLAR ADAPTER
APPROVED		
		SIZE A · DWG NO 1-001 · REV 0
		SCALE NTS · SHEET 1 OF 1

PARTS LIST			
ITEM	QTY	PART NUMBER	DESCRIPTION
2-001	1	LOAD NOSE BASE	
2-002	1	LOAD NOSE SUPPORT	

DETAIL #	QTY
2-000	1

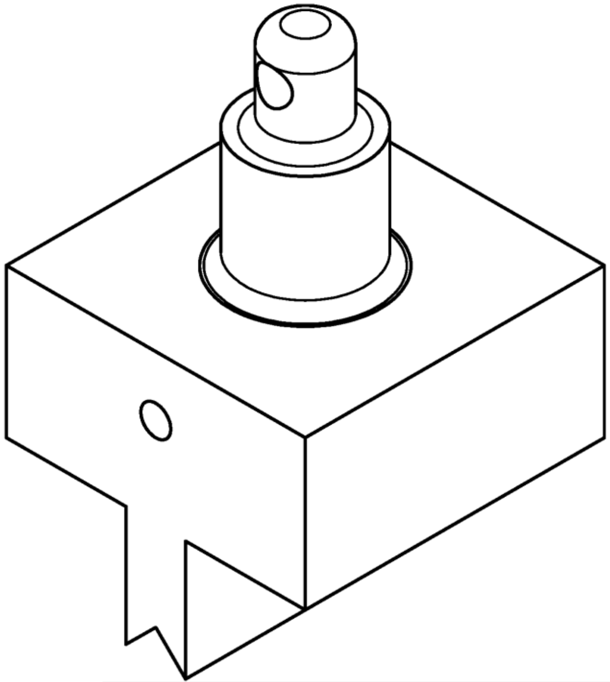

DRAWN A. NORTHMORE	6/7/2013
CHECKED	
QA	
MFG	
APPROVED	

CPATT - UNIVERSITY OF WATERLOO

TITLE
LOAD NOSE ASSEMBLY

SIZE		DWG NO	REV
A		2-000	0

SCALE NTS

SHEET 1 OF 1

DETAIL #	QTY / ASSY	CUT SIZE	FINISH	MATERIAL
2-001	1	2" X 2" X 2" LG	MACHINED	STRUCTURAL STEEL - COLD ROLLED

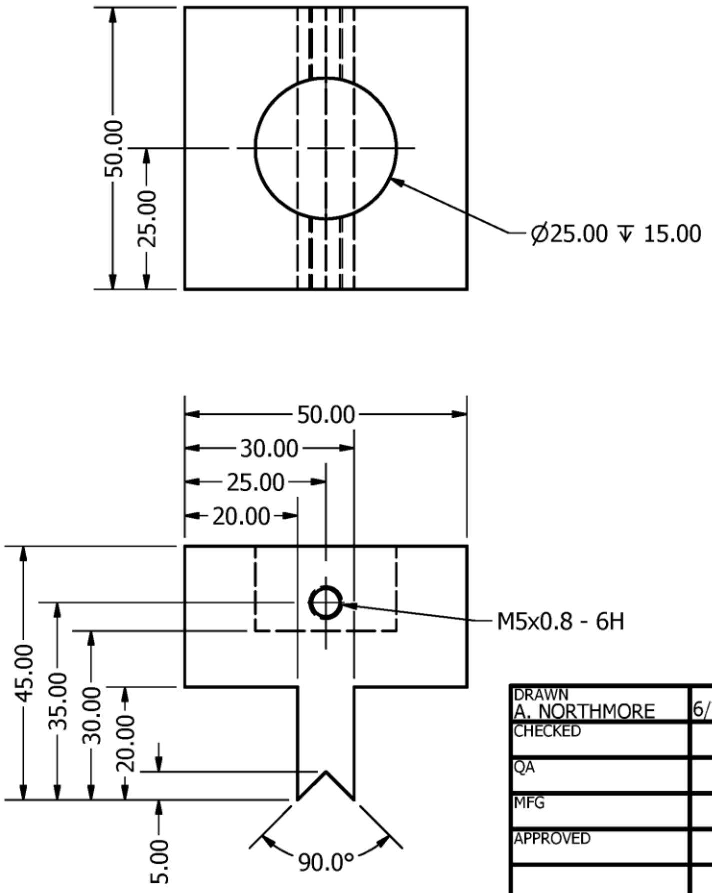

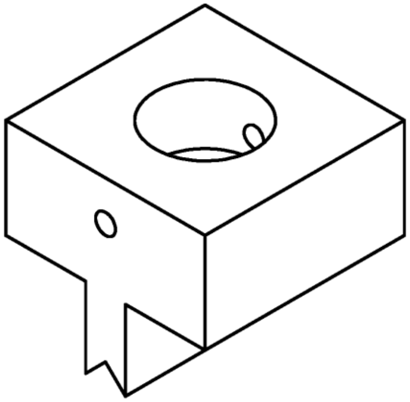

NOTES:
REMOVE ALL SHARP EDGES
ALL DIMENSIONS IN 'MM' UNLESS OTHERWISE SPECIFIED

DRAWN A. NORTHMORE	6/7/2013	CPATT - UNIVERSITY OF WATERLOO	
CHECKED			
QA		TITLE LOAD NOSE BASE	
MFG			
APPROVED			
		SIZE A	DWG NO 2-001 / REV 0
		SCALE NTS	SHEET 1 OF 1

DETAIL #	QTY / ASSY	CUT SIZE	FINISH	MATERIAL
2-002	1	1 1/8" D X 2" LG	MACHINED	STRUCTURAL STEEL - COLD ROLLED

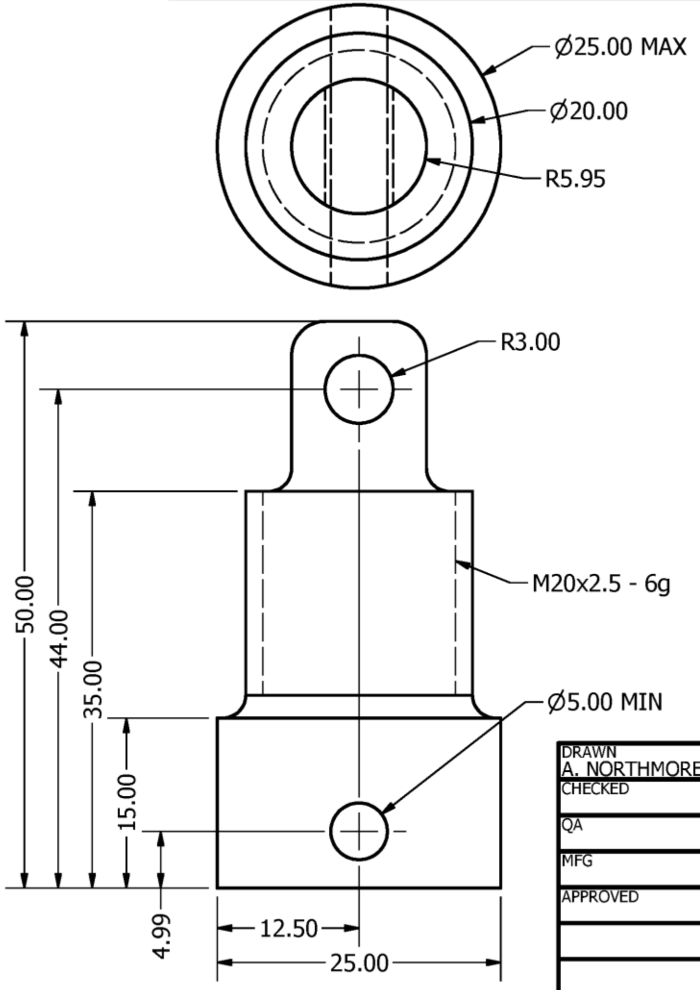

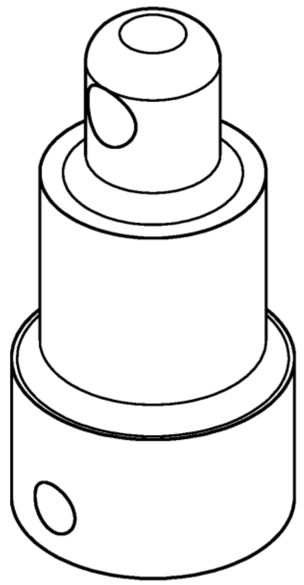

NOTES:
REMOVE ALL SHARP EDGES
ALL DIMENSIONS IN 'MM' UNLESS OTHERWISE SPECIFIED

DRAWN A. NORTHMORE	6/7/2013	CPATT - UNIVERSITY OF WATERLOO
CHECKED		TITLE LOAD NOSE SUPPORT
QA		
MFG		
APPROVED		
		SIZE A · DWG NO 2-002 · REV 0
		SCALE NTS · SHEET 1 OF 1

PARTS LIST			
ITEM	QTY	PART NUMBER	DESCRIPTION
3-001	1	SUPPORT NOSE MAIN	
3-002	1	SUPPORT NOSE CLAMP	

DETAIL #	QTY
3-000	2

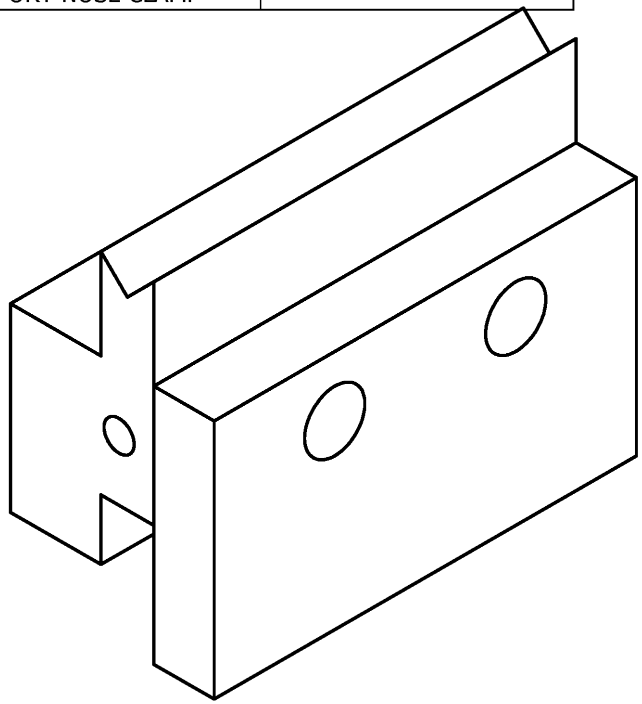

DRAWN A. NORTHMORE	6/4/2013	CPATT - UNIVERSITY OF WATERLOO
CHECKED		TITLE SUPPORT NOSE ASSEMBLY
QA		
MFG		
APPROVED		
		SIZE A · DWG NO 3-000 · REV 0
		SCALE NTS · SHEET 1 OF 1

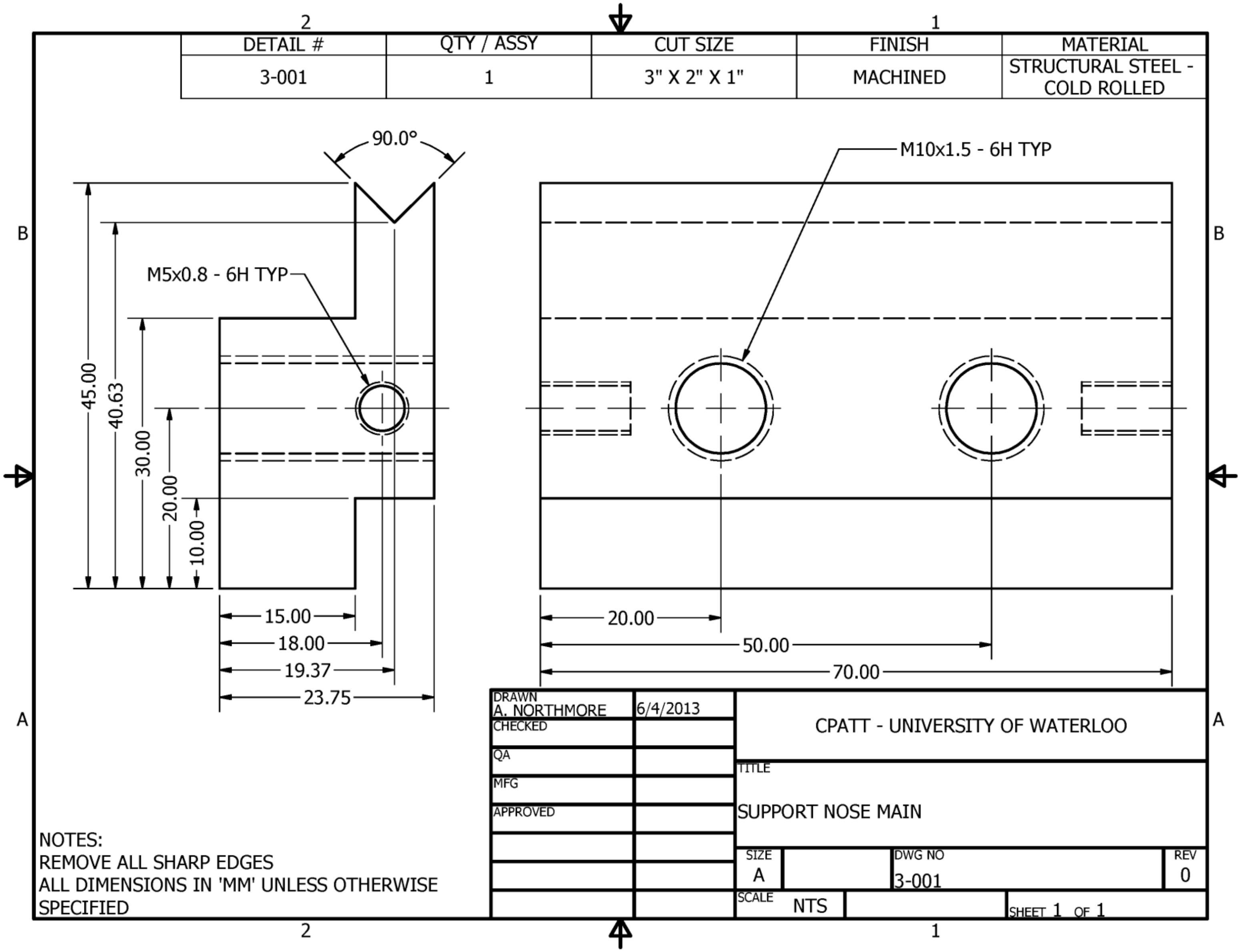

DETAIL #	QTY / ASSY	CUT SIZE	FINISH	MATERIAL
3-001	1	3" X 2" X 1"	MACHINED	STRUCTURAL STEEL - COLD ROLLED

NOTES:
REMOVE ALL SHARP EDGES
ALL DIMENSIONS IN 'MM' UNLESS OTHERWISE SPECIFIED

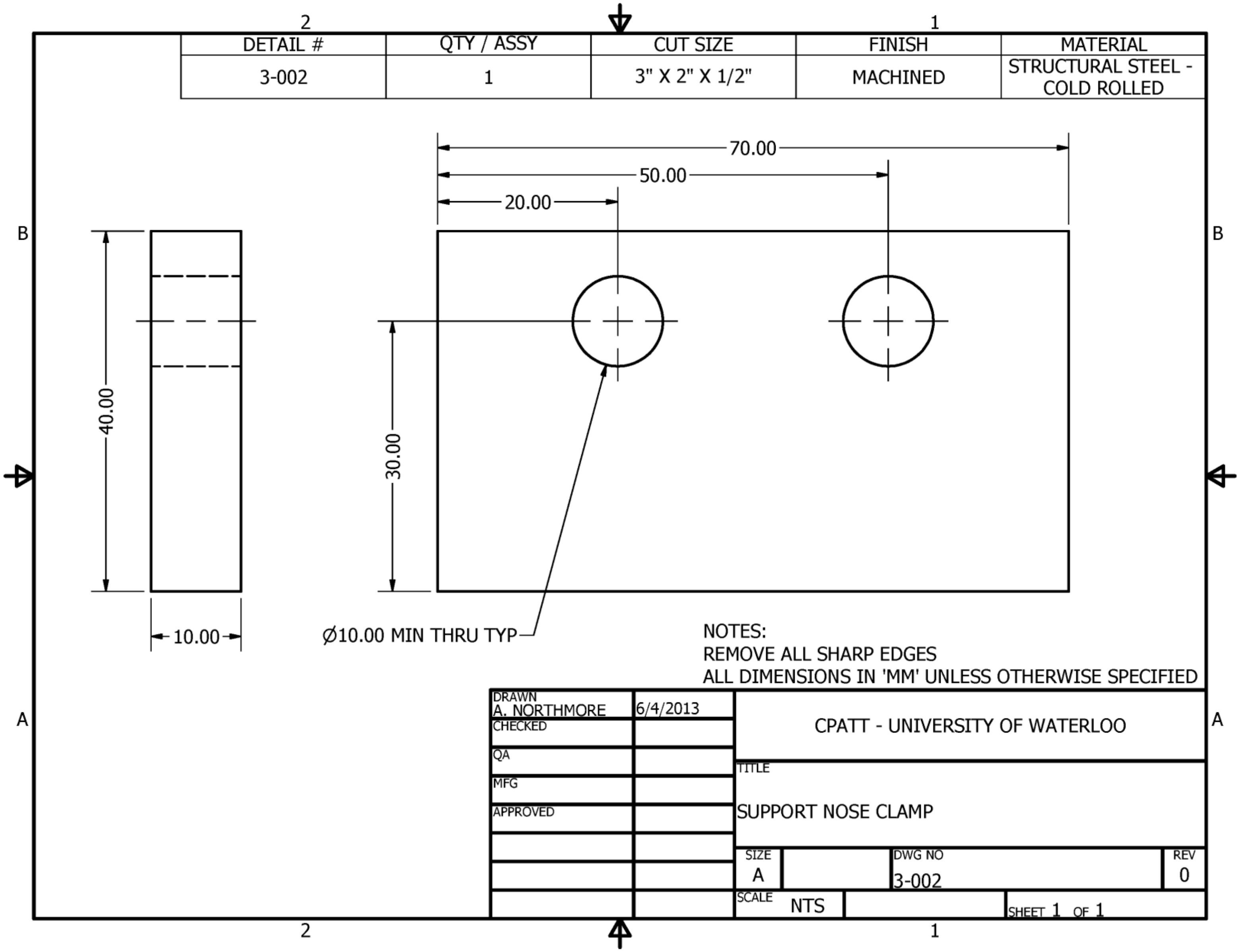

DETAIL #	QTY / ASSY	CUT SIZE	FINISH	MATERIAL
3-002	1	3" X 2" X 1/2"	MACHINED	STRUCTURAL STEEL - COLD ROLLED

NOTES:
REMOVE ALL SHARP EDGES
ALL DIMENSIONS IN 'MM' UNLESS OTHERWISE SPECIFIED

Appendix E

Prototype Model Validation Results

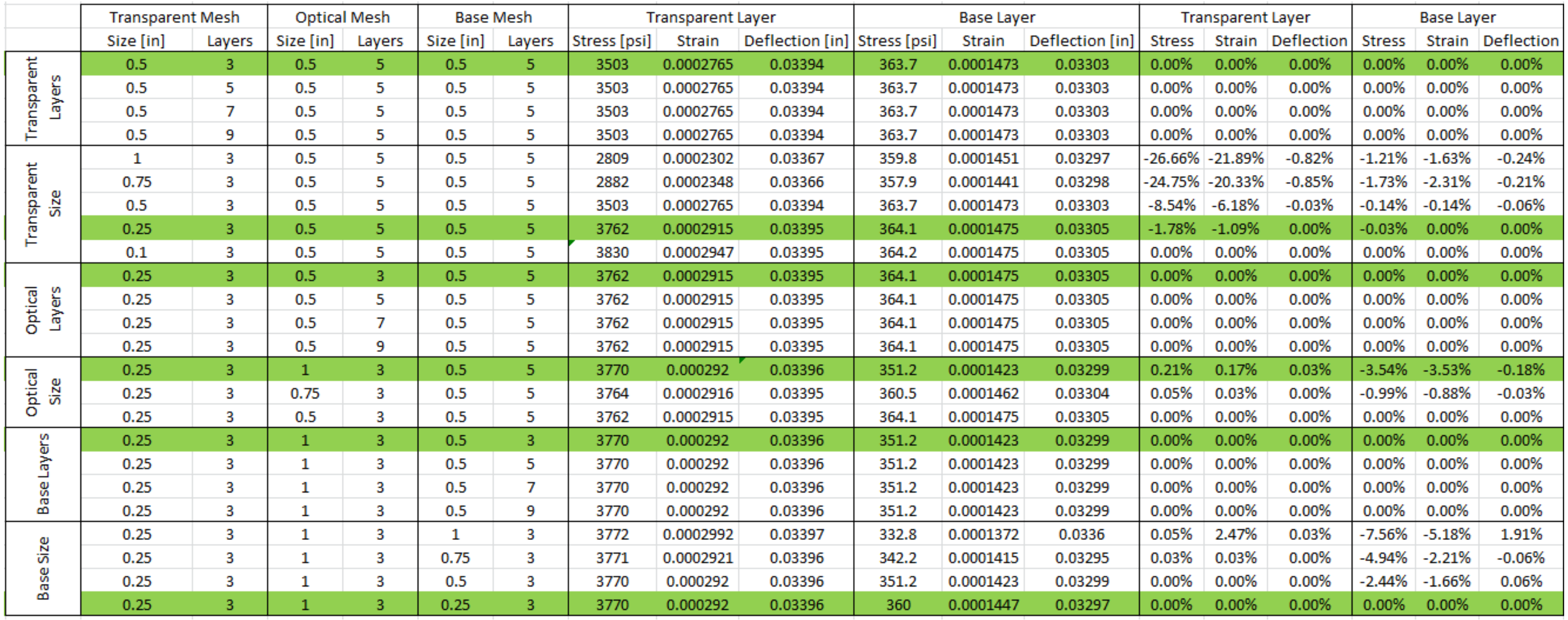

	Transparent Mesh		Optical Mesh		Base Mesh		Transparent Layer			Base Layer			Transparent Layer			Base Layer		
	Size [in]	Layers	Size [in]	Layers	Size [in]	Layers	Stress [psi]	Strain	Deflection [in]	Stress [psi]	Strain	Deflection [in]	Stress	Strain	Deflection	Stress	Strain	Deflection
Transparent Layers	0.5	3	0.5	5	0.5	5	3503	0.0002765	0.03394	363.7	0.0001473	0.03303	0.00%	0.00%	0.00%	0.00%	0.00%	0.00%
	0.5	5	0.5	5	0.5	5	3503	0.0002765	0.03394	363.7	0.0001473	0.03303	0.00%	0.00%	0.00%	0.00%	0.00%	0.00%
	0.5	7	0.5	5	0.5	5	3503	0.0002765	0.03394	363.7	0.0001473	0.03303	0.00%	0.00%	0.00%	0.00%	0.00%	0.00%
	0.5	9	0.5	5	0.5	5	3503	0.0002765	0.03394	363.7	0.0001473	0.03303	0.00%	0.00%	0.00%	0.00%	0.00%	0.00%
Transparent Size	1	3	0.5	5	0.5	5	2809	0.0002302	0.03367	359.8	0.0001451	0.03297	-26.66%	-21.89%	-0.82%	-1.21%	-1.63%	-0.24%
	0.75	3	0.5	5	0.5	5	2882	0.0002348	0.03366	357.9	0.0001441	0.03298	-24.75%	-20.33%	-0.85%	-1.73%	-2.31%	-0.21%
	0.5	3	0.5	5	0.5	5	3503	0.0002765	0.03394	363.7	0.0001473	0.03303	-8.54%	-6.18%	-0.03%	-0.14%	-0.14%	-0.06%
	0.25	3	0.5	5	0.5	5	3762	0.0002915	0.03395	364.1	0.0001475	0.03305	-1.78%	-1.09%	0.00%	-0.03%	0.00%	0.00%
	0.1	3	0.5	5	0.5	5	3830	0.0002947	0.03395	364.2	0.0001475	0.03305	0.00%	0.00%	0.00%	0.00%	0.00%	0.00%
Optical Layers	0.25	3	0.5	3	0.5	5	3762	0.0002915	0.03395	364.1	0.0001475	0.03305	0.00%	0.00%	0.00%	0.00%	0.00%	0.00%
	0.25	3	0.5	5	0.5	5	3762	0.0002915	0.03395	364.1	0.0001475	0.03305	0.00%	0.00%	0.00%	0.00%	0.00%	0.00%
	0.25	3	0.5	7	0.5	5	3762	0.0002915	0.03395	364.1	0.0001475	0.03305	0.00%	0.00%	0.00%	0.00%	0.00%	0.00%
	0.25	3	0.5	9	0.5	5	3762	0.0002915	0.03395	364.1	0.0001475	0.03305	0.00%	0.00%	0.00%	0.00%	0.00%	0.00%
Optical Size	0.25	3	1	3	0.5	5	3770	0.000292	0.03396	351.2	0.0001423	0.03299	0.21%	0.17%	0.03%	-3.54%	-3.53%	-0.18%
	0.25	3	0.75	3	0.5	5	3764	0.0002916	0.03395	360.5	0.0001462	0.03304	0.05%	0.03%	0.00%	-0.99%	-0.88%	-0.03%
	0.25	3	0.5	3	0.5	5	3762	0.0002915	0.03395	364.1	0.0001475	0.03305	0.00%	0.00%	0.00%	0.00%	0.00%	0.00%
Base Layers	0.25	3	1	3	0.5	3	3770	0.000292	0.03396	351.2	0.0001423	0.03299	0.00%	0.00%	0.00%	0.00%	0.00%	0.00%
	0.25	3	1	3	0.5	5	3770	0.000292	0.03396	351.2	0.0001423	0.03299	0.00%	0.00%	0.00%	0.00%	0.00%	0.00%
	0.25	3	1	3	0.5	7	3770	0.000292	0.03396	351.2	0.0001423	0.03299	0.00%	0.00%	0.00%	0.00%	0.00%	0.00%
	0.25	3	1	3	0.5	9	3770	0.000292	0.03396	351.2	0.0001423	0.03299	0.00%	0.00%	0.00%	0.00%	0.00%	0.00%
Base Size	0.25	3	1	3	1	3	3772	0.0002992	0.03397	332.8	0.0001372	0.0336	0.05%	2.47%	0.03%	-7.56%	-5.18%	1.91%
	0.25	3	1	3	0.75	3	3771	0.0002921	0.03396	342.2	0.0001415	0.03295	0.03%	0.03%	0.00%	-4.94%	-2.21%	-0.06%
	0.25	3	1	3	0.5	3	3770	0.000292	0.03396	351.2	0.0001423	0.03299	0.00%	0.00%	0.00%	-2.44%	-1.66%	0.06%
	0.25	3	1	3	0.25	3	3770	0.000292	0.03396	360	0.0001447	0.03297	0.00%	0.00%	0.00%	0.00%	0.00%	0.00%

Appendix F

Pavement Load Case Model Validation Results

PCC Model Validation

Group	Test	B Length (m)	B Width (m)	SG Depth (m)	PCC Mesh (m)	G-A Mesh (m)	SG Mesh(m)	Stress (Pa)	Strain	Deformation (m)	R Stress	R Strain	R Def
SG Depth	1	3	1.5	0.5	0.025	0.025	0.05	776000	0.00000961	0.0000369	-0.47%	-0.42%	-1.70%
	2	3	1.5	1	0.025	0.025	0.05	779000	0.000009643	0.00003742	-0.09%	-0.08%	-0.32%
	3	3	1.5	1.5	0.025	0.025	0.05	779500	0.000009649	0.00003751	-0.03%	-0.02%	-0.08%
	4	3	1.5	2	0.025	0.025	0.05	779600	0.000009651	0.00003753	-0.01%	0.00%	-0.03%
	5	3	1.5	2.5	0.025	0.025	0.05	779700	0.000009651	0.00003754	0.00%	0.00%	0.00%
B Width	1	3	1.5	0.5	0.025	0.025	0.05	776000	0.00000961	0.0000369	-7.96%	-5.78%	-58.74%
	2	3	2	0.5	0.025	0.025	0.05	819500	0.00001004	0.00005619	-2.80%	-1.57%	-37.18%
	3	3	3	0.5	0.025	0.025	0.05	845000	0.00001023	0.00008165	0.23%	0.29%	-8.71%
	4	3	4	0.5	0.025	0.025	0.05	844300	0.00001021	0.00008848	0.14%	0.10%	-1.07%
	5	3	5	0.5	0.025	0.025	0.05	843100	0.0000102	0.00008944	0.00%	0.00%	0.00%
B Length	1	1.5	4	0.5	0.025	0.025	0.05	768400	0.00000945	0.00003679	-8.94%	-7.53%	-63.79%
	2	2	4	0.5	0.025	0.025	0.05	813000	0.000009886	0.00005697	-3.65%	-3.27%	-43.93%
	3	3	4	0.5	0.025	0.025	0.05	844300	0.00001021	0.00008848	0.06%	-0.10%	-12.91%
	4	4	4	0.5	0.025	0.025	0.05	845900	0.00001024	0.00009957	0.25%	0.20%	-2.00%
	5	5	4	0.5	0.025	0.025	0.05	843800	0.00001022	0.0001016	0.00%	0.00%	0.00%
PCC Mesh	1	4	4	0.5	0.05	0.025	0.05	954800	0.00001148	0.0001133	14.76%	14.00%	15.46%
	2	4	4	0.5	0.025	0.025	0.05	845900	0.00001024	0.00009957	1.67%	1.69%	1.47%
	3	4	4	0.5	0.02	0.025	0.05	840900	0.00001017	0.00009892	1.07%	0.99%	0.81%
	4	4	4	0.5	0.015	0.025	0.05	836700	0.00001013	0.00009846	0.56%	0.60%	0.34%
	5	4	4	0.5	0.01	0.025	0.05	832000	0.00001007	0.00009813	0.00%	0.00%	0.00%
G-A Mesh	1	4	4	0.5	0.025	0.05	0.05	846300	0.00001024	0.00009975	0.06%	0.00%	0.22%
	2	4	4	0.5	0.025	0.025	0.05	845900	0.00001024	0.00009957	0.01%	0.00%	0.04%
	3	4	4	0.5	0.025	0.02	0.05	845800	0.00001024	0.00009953	0.00%	0.00%	0.00%
SG Mesh	1	4	4	0.5	0.025	0.05	0.1	846300	0.00001024	0.00009975	0.00%	0.00%	0.00%
	2	4	4	0.5	0.025	0.05	0.075	846300	0.00001024	0.00009976	0.00%	0.00%	0.01%
	3	4	4	0.5	0.025	0.05	0.05	846300	0.00001024	0.00009975	0.00%	0.00%	0.00%

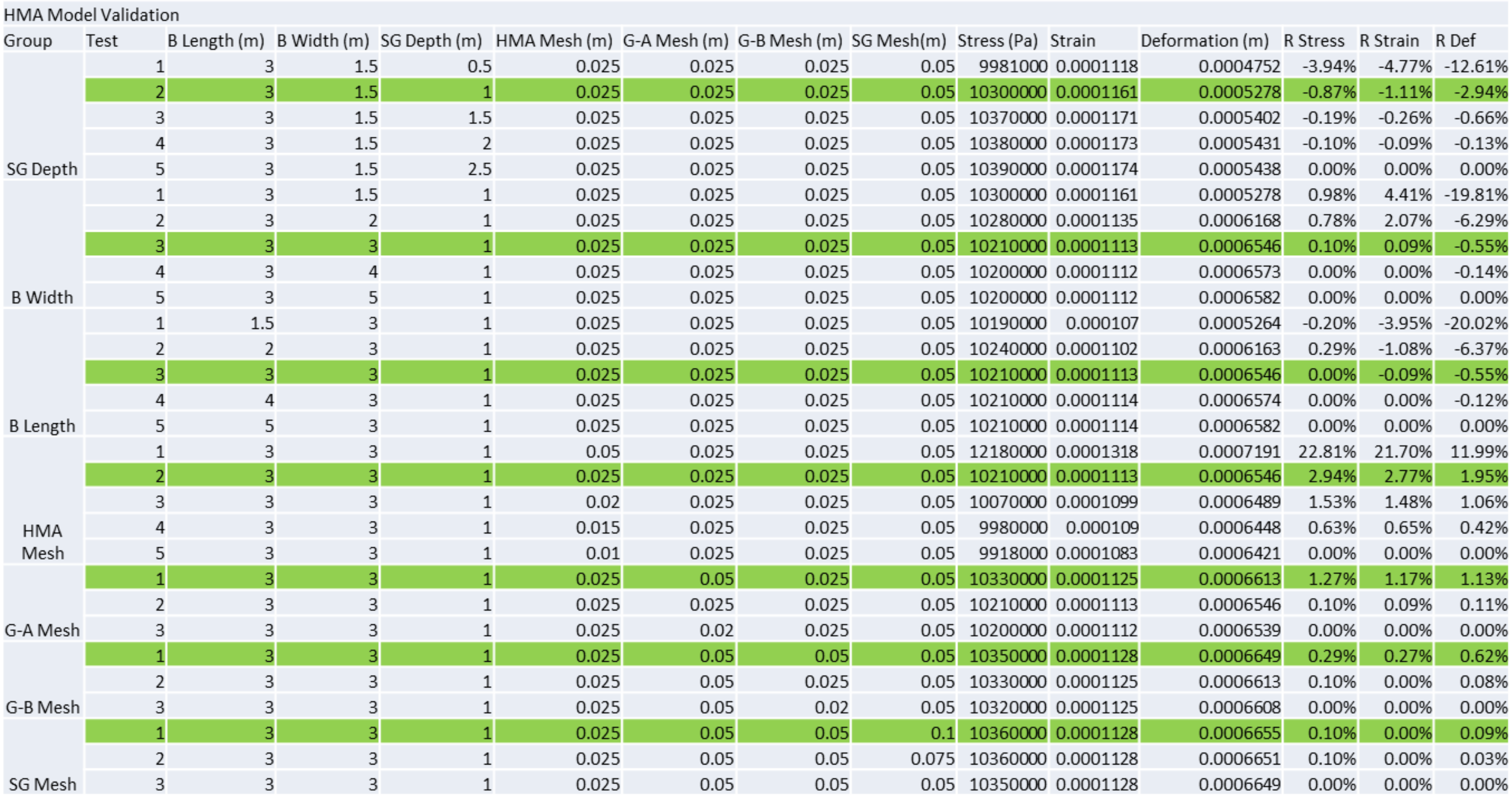

HMA Model Validation

Group	Test	B Length (m)	B Width (m)	SG Depth (m)	HMA Mesh (m)	G-A Mesh (m)	G-B Mesh (m)	SG Mesh(m)	Stress (Pa)	Strain	Deformation (m)	R Stress	R Strain	R Def
SG Depth	1	3	1.5	0.5	0.025	0.025	0.025	0.05	9981000	0.0001118	0.0004752	-3.94%	-4.77%	-12.61%
	2	3	1.5	1	0.025	0.025	0.025	0.05	10300000	0.0001161	0.0005278	-0.87%	-1.11%	-2.94%
	3	3	1.5	1.5	0.025	0.025	0.025	0.05	10370000	0.0001171	0.0005402	-0.19%	-0.26%	-0.66%
	4	3	1.5	2	0.025	0.025	0.025	0.05	10380000	0.0001173	0.0005431	-0.10%	-0.09%	-0.13%
	5	3	1.5	2.5	0.025	0.025	0.025	0.05	10390000	0.0001174	0.0005438	0.00%	0.00%	0.00%
B Width	1	3	1.5	1	0.025	0.025	0.025	0.05	10300000	0.0001161	0.0005278	0.98%	4.41%	-19.81%
	2	3	2	1	0.025	0.025	0.025	0.05	10280000	0.0001135	0.0006168	0.78%	2.07%	-6.29%
	3	3	3	1	0.025	0.025	0.025	0.05	10210000	0.0001113	0.0006546	0.10%	0.09%	-0.55%
	4	3	4	1	0.025	0.025	0.025	0.05	10200000	0.0001112	0.0006573	0.00%	0.00%	-0.14%
	5	3	5	1	0.025	0.025	0.025	0.05	10200000	0.0001112	0.0006582	0.00%	0.00%	0.00%
B Length	1	1.5	3	1	0.025	0.025	0.025	0.05	10190000	0.000107	0.0005264	-0.20%	-3.95%	-20.02%
	2	2	3	1	0.025	0.025	0.025	0.05	10240000	0.0001102	0.0006163	0.29%	-1.08%	-6.37%
	3	3	3	1	0.025	0.025	0.025	0.05	10210000	0.0001113	0.0006546	0.00%	-0.09%	-0.55%
	4	4	3	1	0.025	0.025	0.025	0.05	10210000	0.0001114	0.0006574	0.00%	0.00%	-0.12%
	5	5	3	1	0.025	0.025	0.025	0.05	10210000	0.0001114	0.0006582	0.00%	0.00%	0.00%
HMA Mesh	1	3	3	1	0.05	0.025	0.025	0.05	12180000	0.0001318	0.0007191	22.81%	21.70%	11.99%
	2	3	3	1	0.025	0.025	0.025	0.05	10210000	0.0001113	0.0006546	2.94%	2.77%	1.95%
	3	3	3	1	0.02	0.025	0.025	0.05	10070000	0.0001099	0.0006489	1.53%	1.48%	1.06%
	4	3	3	1	0.015	0.025	0.025	0.05	9980000	0.000109	0.0006448	0.63%	0.65%	0.42%
	5	3	3	1	0.01	0.025	0.025	0.05	9918000	0.0001083	0.0006421	0.00%	0.00%	0.00%
G-A Mesh	1	3	3	1	0.025	0.05	0.025	0.05	10330000	0.0001125	0.0006613	1.27%	1.17%	1.13%
	2	3	3	1	0.025	0.025	0.025	0.05	10210000	0.0001113	0.0006546	0.10%	0.09%	0.11%
	3	3	3	1	0.025	0.02	0.025	0.05	10200000	0.0001112	0.0006539	0.00%	0.00%	0.00%
G-B Mesh	1	3	3	1	0.025	0.05	0.05	0.05	10350000	0.0001128	0.0006649	0.29%	0.27%	0.62%
	2	3	3	1	0.025	0.05	0.025	0.05	10330000	0.0001125	0.0006613	0.10%	0.00%	0.08%
	3	3	3	1	0.025	0.05	0.02	0.05	10320000	0.0001125	0.0006608	0.00%	0.00%	0.00%
SG Mesh	1	3	3	1	0.025	0.05	0.05	0.1	10360000	0.0001128	0.0006655	0.10%	0.00%	0.09%
	2	3	3	1	0.025	0.05	0.05	0.075	10360000	0.0001128	0.0006651	0.10%	0.00%	0.03%
	3	3	3	1	0.025	0.05	0.05	0.05	10350000	0.0001128	0.0006649	0.00%	0.00%	0.00%

Granular Model Validation

Group	Test	B Length (m)	B Width (m)	SG Depth (m)	G-A Mesh (m)	G-B Mesh (m)	SG Mesh(m)	Stress (Pa)	Strain	Deformation (m)	R Stress	R Strain	R Def
SG Depth	1	3	1.5	0.5	0.025	0.025	0.05	20880000	0.0002308	0.0007503	-3.02%	-3.55%	-13.93%
	2	3	1.5	1	0.025	0.025	0.05	21390000	0.0002372	0.0008424	-0.65%	-0.88%	-3.36%
	3	3	1.5	1.5	0.025	0.025	0.05	21500000	0.0002388	0.0008649	-0.14%	-0.21%	-0.78%
	4	3	1.5	2	0.025	0.025	0.05	21520000	0.0002392	0.0008704	-0.05%	-0.04%	-0.15%
	5	3	1.5	2.5	0.025	0.025	0.05	21530000	0.0002393	0.0008717	0.00%	0.00%	0.00%
B Width	1	3	1.5	1	0.025	0.025	0.05	21390000	0.0002372	0.0008424	0.61%	1.98%	-9.95%
	2	3	2	1	0.025	0.025	0.05	21320000	0.0002343	0.0009091	0.28%	0.73%	-2.82%
	3	3	3	1	0.025	0.025	0.05	21260000	0.0002327	0.0009326	0.00%	0.04%	-0.31%
	4	3	4	1	0.025	0.025	0.05	21260000	0.0002326	0.0009347	0.00%	0.00%	-0.09%
	5	3	5	1	0.025	0.025	0.05	21260000	0.0002326	0.0009355	0.00%	0.00%	0.00%
B Length	1	1.5	2	1	0.025	0.025	0.05	21310000	0.0002304	0.0008313	-0.05%	-1.66%	-8.76%
	2	2	2	1	0.025	0.025	0.05	21340000	0.0002334	0.0008903	0.09%	-0.38%	-2.28%
	3	3	2	1	0.025	0.025	0.05	21320000	0.0002343	0.0009091	0.00%	0.00%	-0.22%
	4	4	2	1	0.025	0.025	0.05	21320000	0.0002343	0.0009107	0.00%	0.00%	-0.04%
	5	5	2	1	0.025	0.025	0.05	21320000	0.0002343	0.0009111	0.00%	0.00%	0.00%
G-A Mesh	1	2	2	1	0.05	0.025	0.05	22410000	0.0002446	0.0009238	5.56%	5.34%	4.24%
	2	2	2	1	0.025	0.025	0.05	21340000	0.0002334	0.0008903	0.52%	0.52%	0.46%
	3	2	2	1	0.02	0.025	0.05	21280000	0.0002328	0.0008882	0.24%	0.26%	0.23%
	4	2	2	1	0.015	0.025	0.05	21260000	0.0002325	0.0008872	0.14%	0.13%	0.11%
	5	2	2	1	0.01	0.025	0.05	21230000	0.0002322	0.0008862	0.00%	0.00%	0.00%
G-B Mesh	1	2	2	1	0.025	0.05	0.05	21390000	0.0002339	0.0008965	0.33%	0.30%	0.88%
	2	2	2	1	0.025	0.025	0.05	21340000	0.0002334	0.0008903	0.09%	0.09%	0.18%
	3	2	2	1	0.025	0.02	0.05	21330000	0.0002333	0.0008895	0.05%	0.04%	0.09%
	4	2	2	1	0.025	0.015	0.05	21320000	0.0002332	0.0008887	0.00%	0.00%	0.00%
SG Mesh	1	2	2	1	0.025	0.05	0.1	21400000	0.0002339	0.000898	0.05%	0.00%	0.17%
	2	2	2	1	0.025	0.05	0.075	21390000	0.0002339	0.0008971	0.00%	0.00%	0.07%
	5	2	2	1	0.025	0.05	0.05	21390000	0.0002339	0.0008965	0.00%	0.00%	0.00%

Subgrade Model Validation

Group	Test	B Length (m)	B Width (m)	SG Depth (m)	SG Mesh(m)	Stress (Pa)	Strain	Deformation (m)	R Stress	R Strain	R Def
SG Depth	1	3	1.5	0.5	0.05	30900000	0.000333	0.001064	-4.10%	-4.17%	-20.83%
	2	3	1.5	1	0.05	32000000	0.0003445	0.001275	-0.68%	-0.86%	-5.13%
	3	3	1.5	1.5	0.05	32170000	0.0003468	0.001328	-0.16%	-0.20%	-1.19%
	4	3	1.5	2	0.05	32210000	0.0003473	0.001341	-0.03%	-0.06%	-0.22%
	5	3	1.5	2.5	0.05	32220000	0.0003475	0.001344	0.00%	0.00%	0.00%
B Width	1	3	1.5	1.5	0.05	32170000	0.0003468	0.001328	0.22%	0.76%	-4.73%
	2	3	2	1.5	0.05	32120000	0.000345	0.001369	0.06%	0.23%	-1.79%
	3	3	3	1.5	0.05	32100000	0.0003443	0.00139	0.00%	0.03%	-0.29%
	4	3	4	1.5	0.05	32100000	0.0003442	0.001394	0.00%	0.00%	0.00%
	5	3	5	1.5	0.05	32100000	0.0003442	0.001394	0.00%	0.00%	0.00%
B Length	1	1.5	1.5	1.5	0.05	32170000	0.0003449	0.001291	0.00%	-0.55%	-2.86%
	2	2	1.5	1.5	0.05	32170000	0.0003463	0.001317	0.00%	-0.14%	-0.90%
	3	3	1.5	1.5	0.05	32170000	0.0003468	0.001328	0.00%	0.00%	-0.08%
	4	4	1.5	1.5	0.05	32170000	0.0003468	0.001329	0.00%	0.00%	0.00%
	5	5	1.5	1.5	0.05	32170000	0.0003468	0.001329	0.00%	0.00%	0.00%
SG Mesh	1	1.5	1.5	1.5	0.1	32310000	0.0003463	0.001298	0.72%	0.67%	0.93%
	2	1.5	1.5	1.5	0.075	32230000	0.0003454	0.001296	0.47%	0.41%	0.78%
	3	1.5	1.5	1.5	0.05	32170000	0.0003449	0.001291	0.28%	0.26%	0.39%
	4	1.5	1.5	1.5	0.025	32080000	0.000344	0.001286	0.00%	0.00%	0.00%